THEORETICAL MODELING OF ELECTROMECHANICAL COUPLING BEHAVIOR OF FERROELECTRICS AND THEIR COMPOSITES

by

Yang Cao

A dissertation submitted to the Graduate Faculty in Engineering in partial fulfillment of the requirements for the degree of Doctor of Philosophy, The City University of New York

2009

This manuscript has been read and accepted for the
Graduate Faculty in Engineering in satisfaction of the
dissertation requirement for the degree of Doctor of Philosophy.

Jackie Li

Date
Chair of Examining Committee

Mumtaz Kassir

Date
Executive Officer

Feridun Delale

Honghui Yu

Niell Elvin

Alberto Cuitino
Supervisory Committee

THE CITY UNIVERSITY OF NEW YORK

ABSTRACT

THEORETICAL MODELING OF ELECTROMECHANICAL COUPLING BEHAVIOR OF FERROELECTRICS AND THEIR COMPOSITES

by

Yang Cao

Advisor: Professor Jackie Li

The aim of this dissertation is to develop suitable theoretical models to study the physical properties of ferroelectrics in terms of temperature and size, and the nonlinear electromechanical coupling behavior of ferroelectrics and their composites under the different loading conditions. Three different models are introduced following applicable scale ranges. First, Texture and Anisotropy theory is used to model nonlinear behaviors of piezoelectric poly-crystals (Taylor-Bishop-Hill like model) without considering interaction between grains or domains. It is suitable in macro-scale range and can be used on both polycrystals and single crystals. Second, a micromechanics approach based on irreversible thermodynamic principle and morphology of spontaneous polarization and domain switch has been extended to study the temperature effects on $BaTiO_3$ single crystals and further for electromechanical coupling behavior of ferroelectric composites by considering the microstructure of the system. The micromechanics approach reaches its limitation when the material size reduces to nano-scale. Finally, Ginzburg–Landau theory has been chosen to determine $BaTiO_3$ nanowire behaviors under external loading. This powerful phenomenological method was originally developed for macro scale. Here we extend the model to be applicable at nano-scale range and study the polarization field and transition temperature in terms of the size of ferroelectric nanowires. The advantages and disadvantages of each model are discussed. All three models are also compared and verified by existing experiments.

ACKNOWLEDGEMENTS

My deepest gratitude is to my advisor, Professor Jackie Li, for giving me the freedom to explore on my own; for providing expert guidance and mentorship to help when my steps faltered; and for her patience, understanding, encouragement and support at all levels.

I also want to thank my research committee members, Professor Feridun Delale, Professor Honghui Yu, Professor Niell Elvin and Professor Alberto Cuitino for their time and support.

I am grateful to CUNY administration, the Graduate Center, the School of Engineering, and the Department of Mechanical Engineering for the financial support and the valuable academic and social help.

I thank my colleagues and friends, who helped me in different ways especially my officemates, Zhao Ping and Yves Ngabonziza.

Finally, I thank my wife and my family, for their unconditional and endless support.

TABLE OF CONTENTS

LIST OF TABLES

LIST OF FIGURES

1. Introduction

For decades researchers have been studying the nonlinear electrical-mechanical coupling behavior of ferroelectric ceramics both experimentally & theoretically due to their applications as smart materials in MEMS & other devices. The technology development on electron microscopy stimulates the growth of experimental study on ferroelectric nanowires and nanoparticles, which booms theoretical study on nanoscale ferroelectric phenomenon.

There are several theoretical models dealing with ferroelectrics at different length scales. At macro-scale level: mechanical approaches such as self-consistent crystal plasticity model and viscoplastic crystal model have been developed [1]; To take account of microstructures of the ferroelectrics such as spontaneous polarization and domain switch, micromechanics based approaches have been established [2-7]. At nano-scale level: ab initial method based on first principle and Landau theory approaches have been applied to study the size effects. Due to the complexity of ferroelectric structure and the nature of electromechanical coupling behavior, each model has its limitation and any of the single model alone cannot be utilized to study the electromechanical behavior throughout the different length scales from nano-, to micro- and up to macroscale. The size effect modeling which is always bonded with temperature effect has been overwhelming in ferroelectric field recently but it is just in the beginning stage and the connection between nano-scale and macro scale has not been found.

In this dissertation, three different approaches are proposed to study the piezoelectric and dielectric properties of ferroelectrics in terms of temperature and size, and electromechanical coupling behavior of ferroelectrics and their composites under the different loading conditions. The size range suitable for each approach is presented in Fig.1.1. At the macro-scale level, a simple mechanical approach based on the texture and anisotropy of the system is proposed without consideration of the interaction between the domains and/or grains. Then, a micromechanics approach based on irreversible thermodynamics principle and the morphology of domain switch and spontaneous polarization is developed to study the temperature effect on physical properties of ferroelectric crystals and electromechanical coupling behavior of ferroelectric composites by considering the microstructure of the system. Finally, at the nano-scale, a phenomenological approach named Landau theory is extended to study the polarization distribution and the Curie temperature of ferroelectric nanowires. Although Landau theory was originally developed for macro and micro scales, it can also be modified to study nano-scaled ferroelectrics [8]. Here the focus will be on ferroelectric nanowires. This dissertation is composed in the following orders: In Chapter 2 some basic concepts of ferroelectrics and the reason for this work are presented. In Chapter 3 a literature review for both theoretical and experimental research related to this study is briefly given. From Chapter 4 to Chapter 8, three theoretical models are presented, which includes: (i) Texture and Anisotropy approach in Chapter 4; (ii) Micromechanics approach in Chapter 5 & 6; and (iii) Ginzburg–Landau theory approach in Chapter 8. In Chapter 6, the micromechanics based model is extended to study the hysteresis electromechanical coupling behavior of ferroelectric composites. In Chapter 7, a combined model of Texture and Micromechanics approaches is presented. Finally, the conclusions, contribution from this work and future research are marked in Chapter 9.

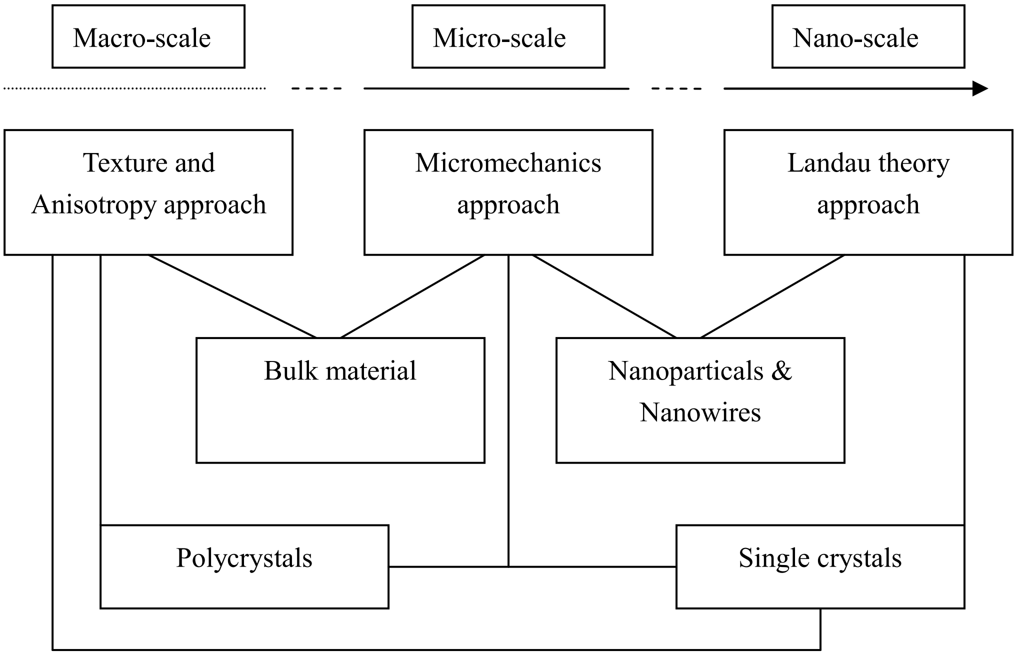

Fig. 1.1 Suitability of three approaches presented in this dissertation

2. Basic Concepts

In the next several chapters, many concepts related to ferroelectricity will come up and the meanings of some of them are sometimes confusing. In order to give readers a clearer view, these concepts including piezoelectricity, dielectricity, paraelectricity and ferroelectricity et al are introduced in this chapter. Then the reasons for choosing $BaTiO_3$ as one of our main studied materials are listed.

2.1 Piezoelectricity

Piezoelectricity is a fundamental process of electromechanical interaction and is a linear interaction between electrical and mechanical systems. In other words, when piezoelectric material is squeezed, an electric charge collects on its surface. Conversely, a piezoelectric material is subjected to an externally applied voltage, it deforms mechanically. The word is derived from the Greek *piezein* which means squeeze or press [9].

The piezoelectricity was discovered in 1880 by Pierre and Jacques Curie during the experiments on quartz. They combined their knowledge of pyroelectricity with their understanding of the underlying crystal structures that gave rise to pyroelectricity to predict crystal behavior, and demonstrated the effect using crystals of tourmaline, quartz, topaz, cane sugar, and Rochelle salt. Quartz and Rochelle salt exhibited the most piezoelectricity.

Piezoelectric crystals are now used in numerous ways because of their special electrical-mechanical coupling behavior. The effect finds useful applications such as the production and detection of sound (piezoelectric sensors), generation of high voltages (quartz), electronic frequency generation, microbalances, and ultra fine focusing of optical assemblies. It is also the basis of a number of scientific instrumental techniques with atomic resolution, the scanning probe microscopes such as STM, AFM, MTA, SNOM etc.

The best-known application is the electric cigarette lighter: pressing the button causes a spring-loaded hammer to hit a piezoelectric crystal, producing a sufficiently high voltage that electric current flows across a small spark gap, thus heating and igniting the gas.

Piezoelectric ceramic fiber technology is being used as an electronic dampening system on some Head tennis rackets. On some inkjet printers, particularly those made by Epson, piezoelectric crystals are used to control the flow of ink from the inkjet head to the paper.

Ferroelectric/piezoelectric materials have become increasingly important in the microelectronics industry and Micro-Electro-Mechanical Systems (MEMS) [10], such as actuators for active control of helicopter rotor blades and underwater vehicle control surfaces, ultrasonic rotary inchworm motor with high power and torque densities and rapid prototyping and stereo lithography techniques [11].

Many materials exhibit piezoelectricity, including both natural and man-made materials. The most common natural piezoelectric material is Quartz. The family of ceramics with perovskite or tungsten-bronze structures exhibits piezoelectricity: Barium Titanate ($BaTiO_3$) was the first piezoelectric ceramic discovered. This dissertation mostly focuses on $BaTiO_3$ crystals. Lead Zirconate Titanate ($Pb[ZrxTi1-x]O_3$ $0<x<1$), more commonly known as PZT, is the most common piezoelectric ceramic in use today.

2.2 Dielectricity, paraelectricity and Ferroelectricity

Most materials are polarized linearly with external electric field; nonlinearities are insignificant. This is called dielectric polarization.

Paraelectricity is the ability of many materials (especially ceramic crystals) to become polarized under an applied electric field. Unlike ferroelectricity, this can happen even if there is no permanent electric dipole tat exists in the material, and removal of the fields results in the polarization in the material returning to zero [10].

A ferroelectric can show a spontaneous polarization and it has the additional property that the polarization can be reversed by applying a sufficiently a large electric field. In a strong alternating field it therefore shows hysteresis [10].

The key physical phenomenon governing the nonlinear response of ferroelectrics happens below the Curie temperature. Typically, materials demonstrate ferroelectricity only below a certain phase transition temperature, called the Curie temperature, T_C, and are paraelectric above this temperature.

2.3 Spontaneous Polarization and Domain Switch

For ferroelectric materials with the perovskite crystal structure, spontaneous polarization changes the crystal system from cubic to tetragonal. Take $BaTiO_3$ as an example, above the Curie temperature the ferroelectrics has central symmetric structure which is paraelectric phase, and below the Curie temperature the structure has changed to asymmetric structure which is ferroelectric phase. When temperature is cooling down from above curie temperature to under it, the ferroelectric material will show this spontaneous polarization (Fig.2.1). More detail will be discussed in Chapter 5.

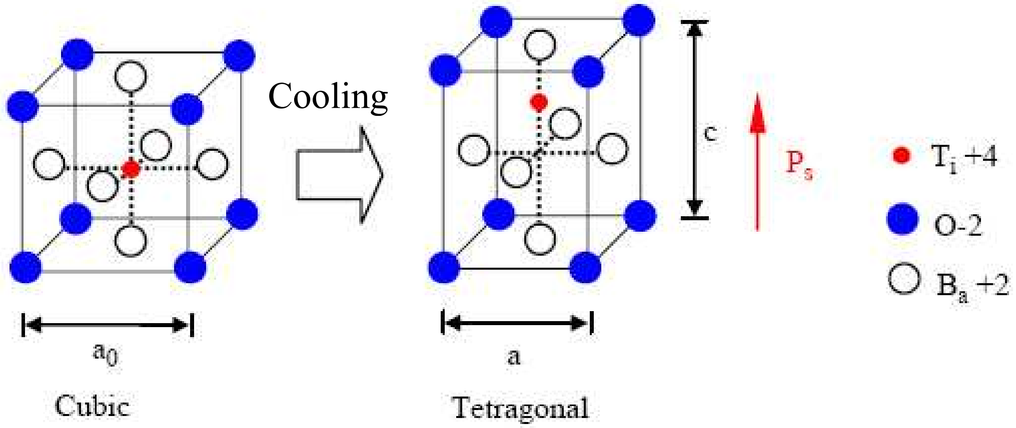

Fig. 2.1 A cubic-to-tetragonal phase transformation of $BaTiO_3$ due to spontaneous polarization upon cooling.

During the phase transition from paraelectric state to ferroelectric state, unit cells in a crystal arrange in such a way that many unit cells in the neighborhood will have the same orientation for the spontaneous polarization and form a domain. The orientation of the spontaneous polarization of a single unit cell in a crystal can be either parallel or perpendicular to the crystallographic axis of the crystal. Therefore there are six possible orientations for a domain in a unit cell though an infinite number of domains are possible in a single crystal material. A poly-crystal ferroelectric material consists of many crystals with random crystallographic orientations, and hence the domains can have numerous random orientations. However, since both the single crystal and poly-crystal piezoelectric materials have numerous domains with different orientations, the net polarization of an unpoled piezoelectric material is practically zero.

The domains in a ceramic crystal are aligned by exposing the crystal to a strong, direct current electric field, usually at a temperature slightly below the Curie point. The unit cells in the ceramic reorient themselves to give a net polarization along the poling direction during the poling process. The unit cell changes its direction of spontaneous polarization by switching 90° or 180° to a direction closer to the poling direction. In fact, domain switch is a gradual process and crystalline cells in a domain do not all switch simultaneously [12]. The process of domain switch starts with nucleation at different point on the existing domain, followed by switching of unit cells on the boundary of the nucleus, thus causing spreading of the newly formed domain. The movement of the newly formed domain boundary is called domain wall movement, and it sweeps fully through the existing domain to complete the domain switching process [13]. So through this poling process, domains most nearly aligned with the electric field expand at the expense of domains that are not aligned with the field, and the ceramic crystal lengthens in the direction of the field. After the electric field is removed, the crystal has a permanent polarization, the remanent polarization, and is permanently elongated.

2.4 Reasons for choosing $BaTiO_3$

We choose $BaTiO_3$ as our main focus in this dissertation. There are several reasons:

(1). Representable

Barium titanate is an oxide of barium and titanium with the chemical formula $BaTiO_3$. It is a typical perovskite ceramics (having ABO_3 compounds of perovskite structure), with a photorefractive effect and piezoelectric properties. It has five phases as a solid, listing from high temperature to low temperature: hexagonal, cubic, tetragonal, orthorhombic, and rhombohedral crystal structure. All of the structures exhibit the ferroelectric effect except cubic.

(2). Simple

Compare to the most common piezoelectric material PZT, $BaTiO_3$ has less elements so that a simpler structure.

(3). Experiments results available

Doing theoretical modeling, the theory has to be tested by comparing model results with experiments data. Available experiments data for $BaTiO_3$ single crystal, poly-crystals and nanowires give us the chance to test our models.

3. Literature Review

3.1 Theoretical Modeling

3.1.1 Mechanical Modeling

Huber and Fleck [1] introduced three constitutive models to capture the multi-axial response of the ferroelectric material: a rate-independent self-consistent plasticity model, a simplified viscoplastic crystal plasticity model with a reduced set of transformation systems, and a rate-independent phenomenological model. In each case the model was calibrated by using measurement of material response to fix the model parameters.

Hwang et al [14] developed Preisach hysteresis model to simulate electro-mechanical coupling behavior in each grain of the PLZT (Lead lanthanum zirconate titane). Then work energy criterion was applied to catch the critical loading at which the domain switching occurs in the grain. The electric displacement and strain were calculated by averaging over all grains during the mechanical modeling. Later, the same group (Hwang et al [15]) proposed a modified model of polarization switching to simulate the response of strain and electric displacement under electromechanical loading in polycrystalline tetragonal ferroelectric ceramics. A few additional parameters of the material were added to the energy equation to get a better agreement with the experimental results.

Our Texture and Anisotropy theory model (Chapter 4) has adopted Euler angle texture orientation system. Using the fast and recurrent increase of the computational power, we can calculate thousands of grains with different orientations. The model could be powerful but it requires a crucial input data which is the original texture orientation of the material.

3.1.2 Micromechanics Approach

Micromechanics approach has been widely applied to model the nonlinear electro-mechanical coupling behavior of ferroelectric materials, which is based on microstructure of domain switch. In general, commercial ferroelectric ceramics such as PZTs are poly-crystals. In order to use micromechanics approach, it is assumed that each grain processes its own effective polarization with its specific direction. Then the self-consistent model can be applied to study overall behavior of poly-crystals. The main calculation criterion is the domain switching under the applied electric field and mechanical stress. To get the macroscopic response of the bulk material subjected to the external loads, an energy equation is used for the threshold of domain switching in each grain and the averaging technique is implemented in the bulk material.

For ferroelectric single crystals, a microscopic constitutive model was presented by Chen et al [2]. They added an internal variable in the theoretical constitutive equations and domain volume fractions to simulate the nonlinear behavior of polycrystalline ferroelectrics.

Fan et al [3] also developed a micromechanics constitutive model to describe the nonlinear behavior of polarization switching. The irreversible strain was simulated by a mechanical model, consisting of several parallel-arranged Maxwell chains with each chain taking a main role in a different, successive stage of the switching process. This spreads the overall polarization switching over a range of stress and electric field levels.

Seemann [4] presented a micromechanical modeling of ferroelectric materials by using probability functions in the energy equations for domain switching.

As we mentioned above, those micromechanical approaches have used an energy criterion to simulate the domain switching of ferroelectric materials. In those models, the homogenization or averaging process is adopted to describe the overall response of a ferroelectric polycrystal. However, in the study of nonlinear behavior of a ferroelectric material, the irreversible thermodynamics and physics of domain switch are also important. Li and Weng [5, 6] developed a micromechanics model combined with the irreversible thermodynamics and physics involved in domain switch. This method is different from those mentioned above because the irreversible thermodynamics has been applied to develop the ferroelectric behavior instead of an energy criterion. Li [7] extended the micromechanics models [5, 6] to study the multi-axial response of ferroelectrics. An equivalent system was introduced to capture the key nonlinear response of ferroelectric poly-crystals subjected to the multi-axial loading. The overall effective polarization due to the multi-axial electric switch is identical to the one of the real polycrystal system.

3.1.3 Quantum mechanics approach

During the past two decades, the size effect of ferroelectric materials including ferroelectric thin films, nanoparticles and nanowires attracted considerable attention of physicists. From the experiment part, successful patterning of nanoscale ferroelectric structures using focused ion-beam sputtering or electron beam direct writing [16, 17] together with nanoscale measurements based on scanning force microscopy (SFM) [18] enabled experimental studies of finite size effects in single mesoscopic ferroelectric structures. From the theoretical modeling part, due to the modern computer power, there has been an evolution in atomistic modeling of materials. It is possible to describe material properties very accurately using methods directly based on the fundamental laws of quantum mechanics principles. “First principle” and “ab-initio” techniques are largely used. The class of ABO_3 compounds of perovskite structure especially $BaTiO_3$ has been studied using first principle method.

Until the advent of the recent atomistic simulations, the most popular approach to describe the temperature behavior of ferroelectrics at the macroscopic level was the phenomenological Devonshire-Ginzburg- Landau (DGL) theory [19, 20].

The Landau approach considers polarization and strains as independent degrees of freedom. The expression for the thermodynamic potential around the unpolarized cubic crystal, as reported by Devonshire in the pioneering works [19, 20] is given by poly-nominal functions.

3.2 Experimental Research

3.2.1 PZT Poly-crystals and Their Composites

Huber and Fleck [1] conducted a few experiments on multi-axial electric switching of a ferroelectric material. They have determined the relation of the change in electric displacement and applied electric field for a selection of specimens at θ=0, 45, 90, 135 and 180°. In the case of the 0° specimen, there is only slight non-linearity in the dielectric response because of no domain switching. By contrast, in the 180° specimen the change of remanent polarization occurs, of magnitude 0.48 Cm^{-2}. In the other cases, the curves show nonlinear responses under the electric field.

In Chapter 4, we will use Texture and Anisotropy approach to simulate these experimental results.

Zhao and Li [21, 22] have systematically studied the orientation effects on nonlinear electromechanical coupling behavior of PZT ceramics and PZT composites. They have carried out extensive experimental tests under compressive loading or electric field loading. In Chapter 7, a two-level micromechanics model will be developed to study the hysteresis behavior of ferroelectric composites and compared to Zhao and Li's [21, 22] experimental data. For more details about multi-axial loading on PZT materials and PZT composites, see Zhao's dissertation. [22]

3.2.2 $BaTiO_3$ single crystal and poly-crystals

Merz [23-27] has done a series of testes on $BaTiO_3$ type I and type II single crystals in 1950s. The results include relations between spontaneous polarization, dielectric constants and piezoelectric constants with external electric fields and external stress fields. Merz also did experiments on $BaTiO_3$ poly-crystals. These results are used widely for theoretical modeling on $BaTiO_3$ crystals. In Chapter 5, a micromechanics model will be presented and compared with these experimental results.

3.2.3 Ferroelectric Nanoparticles

Size effects on the ferroelectric phase transition in $PbTiO_3$ ultrafine particles (nearly free from the effect of the substrate) were initially reported by Ishikawa and coworkers [28, 29] and Zhong et al. [30]. Using high-resolution transmission electron microscopy (HRTEM) techniques, Jiang et al. [31] have found that the nanoparticles might be grown with extremely clean and sharp surfaces. Particles larger than 20 nm formed 90° domains, whose width decreased with decreasing the particle size. A phase transition to a monodomain state was observed for particle sizes smaller than 20 nm.

Fig.3.1 represents the thickness dependence of T_C. The results strongly suggested the presence of a critical size, estimated between 9.1 nm and 10.7 nm, below which the ferroelectric state becomes unstable. The same conclusion could be drawn by following the evolution of the specific heat [30] or the tetragonality [29, 30].

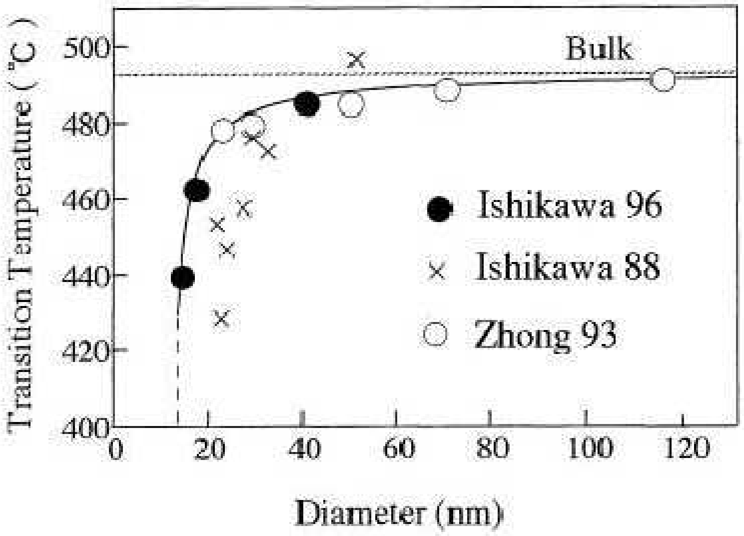

Fig. 3.1: Evolution of the paraelectric-to-ferroelectric transition temperature of $PbTiO_3$ ultrafine particles as a function of the particle size. Filled circles correspond to data reported in Ref. [29], crosses to Ref. [28] and open circles to Ref. [30]. The solid line is a fit to the empirical relation $Tc(d) = Tc(\infty) - \frac{C}{d - d_{crit}}$, where $Tc(\infty)$ is the critical temperature of the bulk crystal (dashed line), d_{crit} stands for the particle size, d_{crit} is the critical diameter below which ferroelectricity disappears, and C is a constant to fit the formula [29].

3.2.4 Ferroelectric Nanowires

The growth of ferroelectric nanowires has also been reported recently. $BaTiO_3$ ferroelectric nanowires of diameters ranging from 5 to 60 nm and lengths larger than 10 μm have been synthesized by Yun and coworkers [32]. A polarization perpendicular to the nanowire axis was induced and manipulated by an external electric field. Nonvolatile polarization domains, as small as 100 nm^2 in size (equivalent to a data storage density of about 1 $Tbit/cm^2$ in a real memory device) were written and reversed repeatedly and independently on these nanowires.

A DFT first-principles study of finite-size effects in $BaTiO_3$ nanowires has also been reported [33], looking explicitly at the dependence of the ferroelectric instability in the direction of the wire axis. Model systems of increasing size were built starting from $BaTiO_3$ clusters that are assemble together into infinite chains along z direction, themselves gathered together into nanowires of diameter n (n corresponds to the number of Ti-O chains combined within the wire). Each of these stechiometric wire has two BaO surfaces and two TiO_2 surfaces (Fig.3.2).

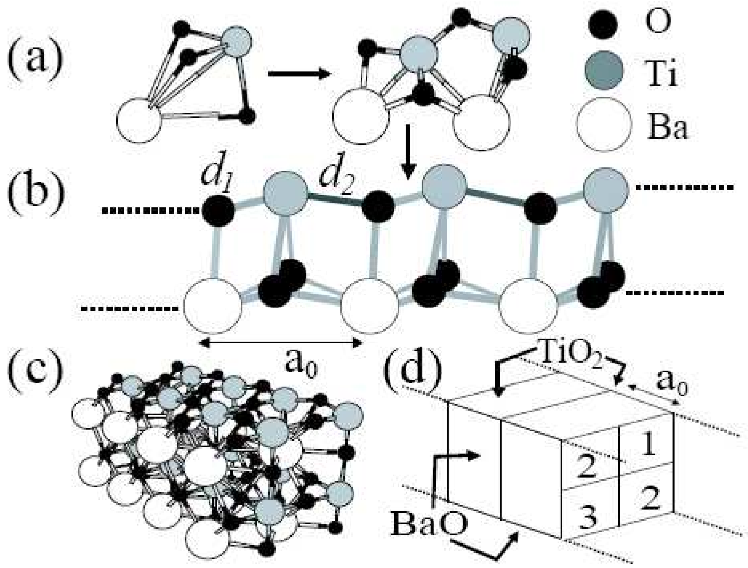

Fig. 3.2: $BaTiO_3$ stechiometric wires: $BaTiO_3$ clusters (a), assemble into infinite chains (b), themselves gathered together into nanowires (c) of diameter n. Panels (c) and (d) correspond to n = 4. [33].

Due to the low coordination of the atoms at the surface, the relaxed bond lengths for the thinnest wires are much shorter than in bulk. A critical diameter for ferroelectricity along the wire direction was predicted for $n_c \approx 9$. Below n_c, the polar distortion along the Ti-O chains is suppressed for the relaxed geometry but can be recovered by applying a tensile strain.

The transition from the paraelectric-to-ferroelectric nanowire is second order with the amplitude of the polar distortions increasing gradually as the equilibrium lattice constant tends to the bulk value (inset of Fig.3.7). The strong inhomogeneity of the distortions for the different Ti-O chains is in good agreement with the first-principles calculations of $BaTiO_3$ free surfaces, where an enhancement of the polarization for the in-plane polarization is observed for the TiO_2 terminated surface, while it is decreased in the BaO-terminated surface [34]. This fact points to a strong influence of the surface on the polarization of the different chains.

The ferroelectric behavior of the nanowires appears to be monitored by the strong sensitivity of ferroelectricity on the unit cell volume [35], itself determined by the low coordination effects at free surfaces.

Variable temperature electrostatic force microscopy is used by Andrew M. Rappe group [36] to manipulate, image, and evaluate the diameter-dependent stability of ferroelectric polarizations. These measurements show that the ferroelectric phase transition temperature (T_C) is depressed as the nanowire diameter (d_{nw}) decreases, following a 1/dnw scaling. The diameter at which T_C falls below room temperature is determined to be ~3 nm, and extrapolation of the data indicates that nanowires with dnw as small as 0.8 nm can support ferroelectricity at lower temperatures.

The $1/d_{nw}$ scaling relation shown in Fig.3.3 suggests that the observed suppression of ferroelectricity is caused by the depolarizing field. However, current views of ferroelectric destabilization with size suggest that the magnitude of this depolarizing field should become too large to support stable polarization at significantly greater values of

d_{nw} than those observed in Fig.3.3, particularly in a geometry lacking a top metallic electrode that screens the polarization charge. The data therefore suggest that a new screening mechanism is responsible for stabilizing nanoscale ferroelectricity in $BaTiO_3$ nanowires.

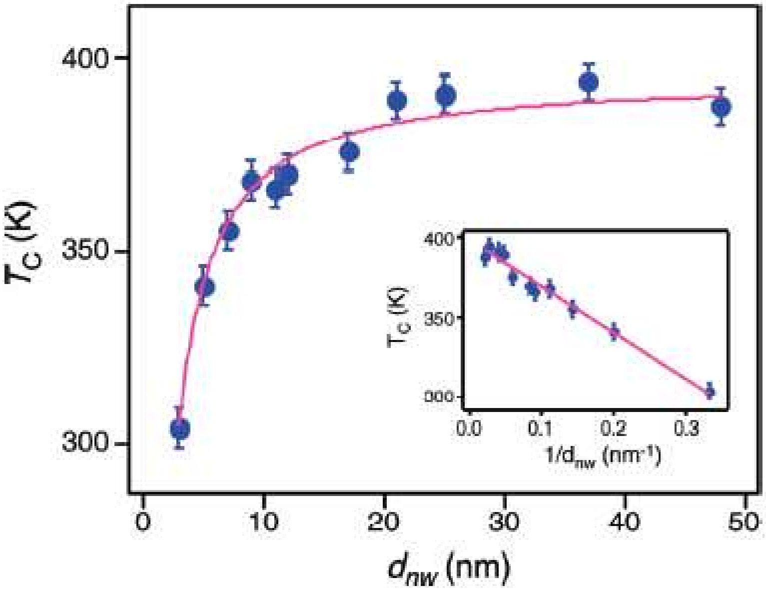

Fig. 3. 3 Ferroelectric phase transition temperature (T_C) as a function of d_{nw}. The solid circles are the experimentally determined T_C, and the error bars are uncertainties. The magenta solid line is the result of the fit to the data using the $1/d_{nw}$ scaling relation. The inset plots T_C as a function of $1/d_{nw}$ and illustrates the inverse diameter dependence [36].

In chapter 8, a modified Landau theory will be developed to study the polarization field of ferroelectric nanowires. The theory will be also applied to study the Curie temperature in terms of diameter of the wire and compared with the experimental data in Fig.3.3.

4. Texture and Anisotropy Approach

4.1 Introduction

Huber and Fleck [1] introduced three constitutive models to capture the multi-axial response of the ferroelectric material: a rate-independent self-consistent plasticity model, a simplified viscoplastic crystal plasticity model with a reduced set of transformation systems, and a rate-independent phenomenological model. In each case the model was calibrated by using measurement of material response to fix the model parameters.

Fig.4.1 shows the comparison of the three models with experiment results. As a conclusion, the self-consistent polycrystal model is computationally cumbersome for practical engineering modeling. The simplified viscoplastic crystal model neglects local interaction fields and then gives an improvement between speed and accuracy for practical engineering modeling. The phenomenological model is suitable for uniaxial loading and unable to reproduce the full range of multi-axial behavior in its present form.

From a totally different point of view, we have developed a simpler mechanical model to describe this phenomenon. The model presented below is adopted from a metal crystalline stress field model which was used to study fundamental slip and twinning system in metals. This approach fully relies on material's crystalline orientations and single grain behavior assumption. Although Huber and Fleck' work was nice enough, we believe this simpler model can better present the problem and is more applicable to realistic cases. With the help of advanced technique, the accuracy of this model can be fully tested.

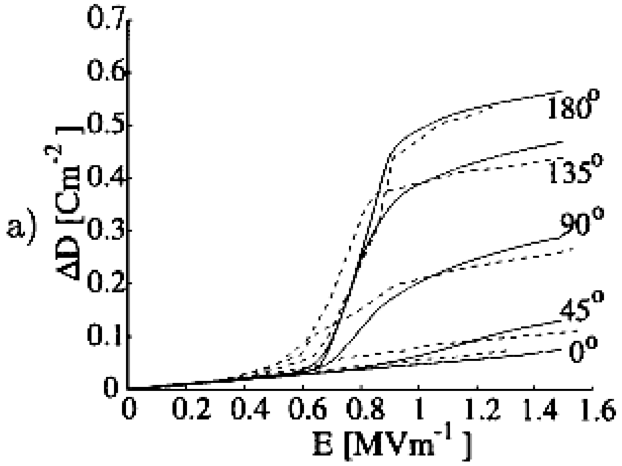

Fig. 4.1 (a) Comparison between calculated responses using three models and experimental results: self-consistent crystal plasticity model. [1]

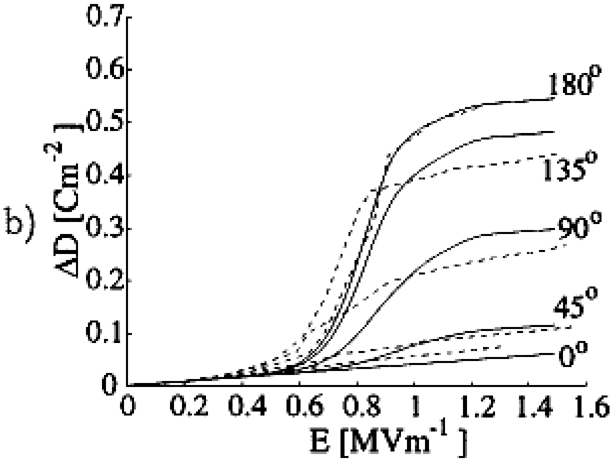

Fig. 4.1 (b) Comparison between calculated responses using three models and experimental results: simplified viscoplastic crystal model. [1]

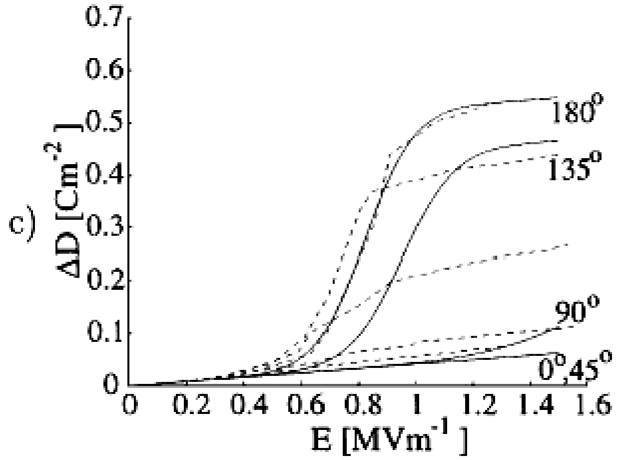

Fig. 4.1 (c) Comparison between calculated responses using three models and experimental results: phenomenological model. [1]

Modern views of crystals state that crystals have well defined directions with associated anisotropy. Preferred orientation (texture) strongly influences properties of all kinds. Anisotropy is referring to dependence of the crystal properties on the chosen direction.

The Taylor-Bishop-Hill (TBH) model of crystallographic lattice rotation is an important model for the development of lattice-preferred orientations in naturally and synthetically deformed rocks, metals and ceramics. The model describes intra crystalline deformation in terms of slip along discreet slip systems, which are different for different materials. As the crystal slips along a slip system, the crystallographic lattice reorients into alignment with respect to the bulk flow field in the rock. By this mechanism, a lattice preferred orientation microstructure develops [37].

In TBH model, they identified all of the 28 stress states, using principle of maximum virtual work to determine which stress state would be appropriate for a given shape change to activate the required slip systems. In our work, for each individual grain, instead of slip system, the domain switch (90° or 180°) will be activated by the external force. Once the relation between the external loading and domain switch is obtained in individual grain, the overall behavior of the system can be obtained by sum the effect of all the grains.

Before we apply this texture model to study the nonlinear behavior of ferroelectrics, a 2-D model is demonstrated here as an example. (This example can be presented using an interactive movie clip.) Suppose the material has initial random polarization as shown in Fig.4.2a. When an external electric field is applied, some polarizations will have 90° switch, some will have 180° switch and the rest won't have any kind of switch (Fig.4.2b, c). How each individual grain will behave depends on its orientation with respect to the applied electric field. The rules used in this model are as follows:

Let's call the angle between the grain's orientation and the applied electric field α

1. If $\alpha < 45°$, polarization won't change;
2. If $\alpha > 45°$ and $\alpha < 135°$, applied electric field exceeds a certain value, polarization will have 90° switch towards applied electric field direction;
3. If $\alpha > 135°$, applied electric field exceeds a certain value, polarization will have 180° switch towards applied electric field direction.

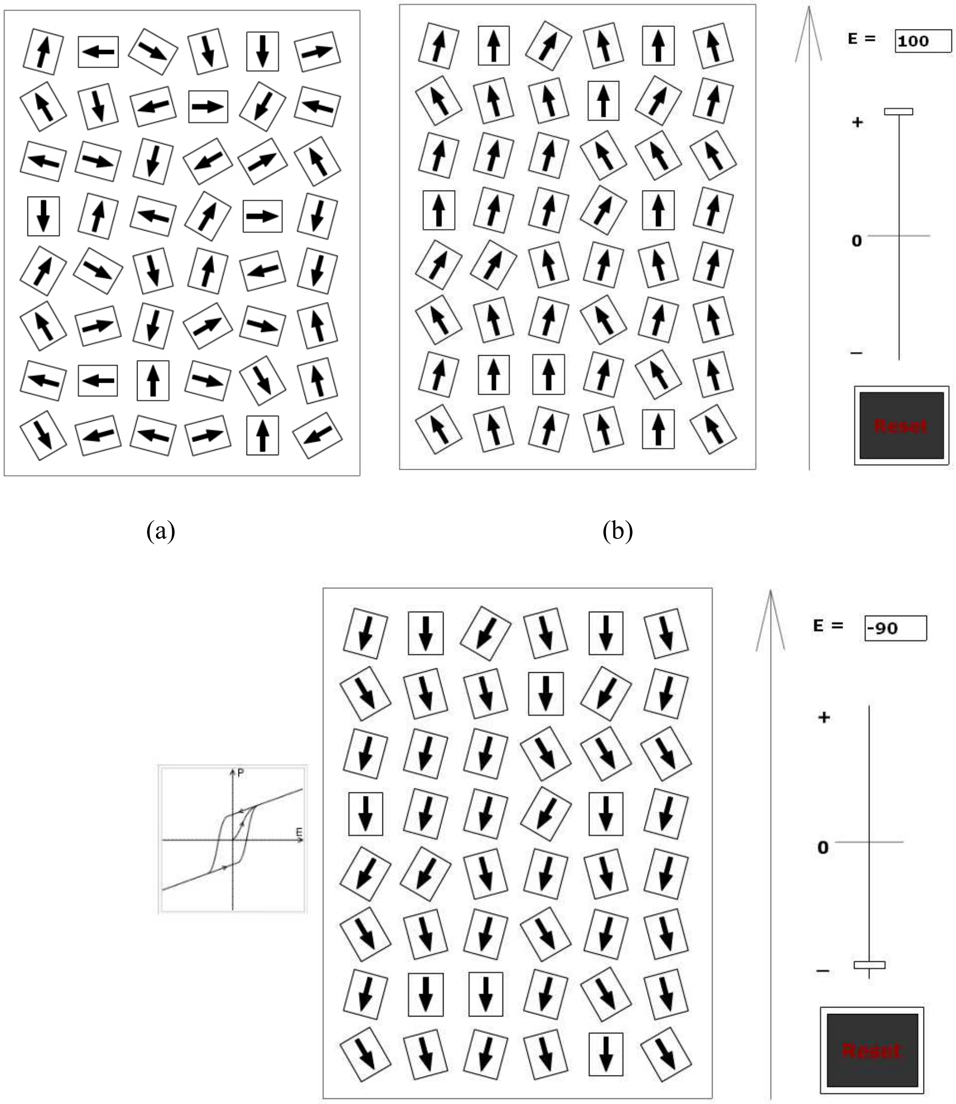

(a)

(b)

(c)

Fig. 4.2 (a) initial random polarization; (b) when positive applied electric field exceeds a certain value; (c) when negative applied electric field exceeds a certain value

4.2 Euler angles

The above example is a 2-D case. To illustrate the orientation of each grain in 3-dimentional space, we use Euler angles which is the most commonly used method in crystalline texture study. We are able to determine the effective force applying to each individual grain using transformation matrix derived from Euler angles. Then two questions will be answered for each single grain that are: (1) Will domain stay original orientation or switch to a new orientation? (2) Which angle will the domain switch to if it does switch to a new orientation?

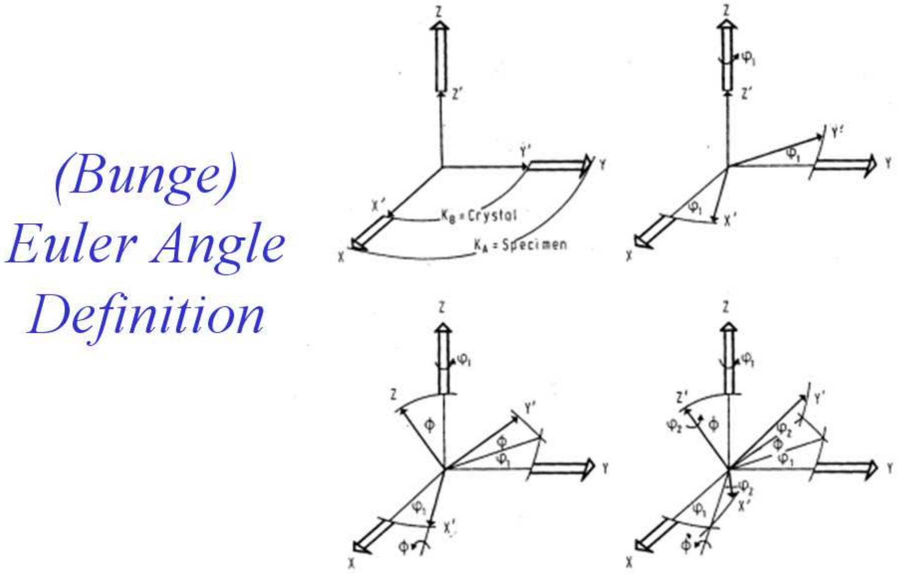

Fig.4.3 Illustration of Euler Angles [38]

Euler angles give us the 3-dimentional relation between the local orientation (grain) and the global orientation (sample). The three Euler angles can be described as follows: the 1st angle, φ_1, is the angle by rotating the crystal about the ND, then angle Φ is the out of plane rotational angle (about the [100] axis); finally, the 3rd angle (φ_2) is the angle by rotating the crystal about [001]. The illustration of Euler angles is shown in Fig.4.3.

The transformation matrix derived from Euler angles is given as follows

$$g = \begin{bmatrix} \cos\varphi_1 \cos\varphi_2 - \sin\varphi_1 \sin\varphi_2 \cos\Phi & \sin\varphi_1 \cos\varphi_2 + \cos\varphi_1 \sin\varphi_2 \cos\Phi & \sin\varphi_2 \sin\Phi \\ -\cos\varphi_1 \sin\varphi_2 - \sin\varphi_1 \cos\varphi_2 \cos\Phi & -\sin\varphi_1 \sin\varphi_2 + \cos\varphi_1 \cos\varphi_2 \cos\Phi & \cos\varphi_2 \sin\Phi \\ \sin\varphi_1 \sin\Phi & -\cos\varphi_1 \sin\Phi & \cos\Phi \end{bmatrix} \tag{4.1}$$

Inside the transformation matrix, the rows are the direction cosines for [100], [010], [001] in the sample coordinate system (global); the columns are the direction cosines for RD, TD and ND in the crystal system (local).

For given grain orientation, we can use transformation matrix to get the directions of grain in sample coordinate system; then, compare to external force direction and magnitude, we can get effective force; when effective force exceed a certain value along a different direction with respect to grain's original orientation, we will have domain switch. That answers our first question listed above. Then we shall test all the 6 directions in the grain coordinate system to determine which direction is desirable for domain switches. Both questions are answered now.

4.3 Pole figures

Pole figures are used to show the orientation of each single crystal or poly-crystals. A direct pole figure is a graphical representation of the angler distribution function of a chosen crystal direction with respect to the sample coordinate system. Here is an example showing a crystal oriented to put all 3 <100> directions approximately equally spaced from the ND. (See Fig.4.4)

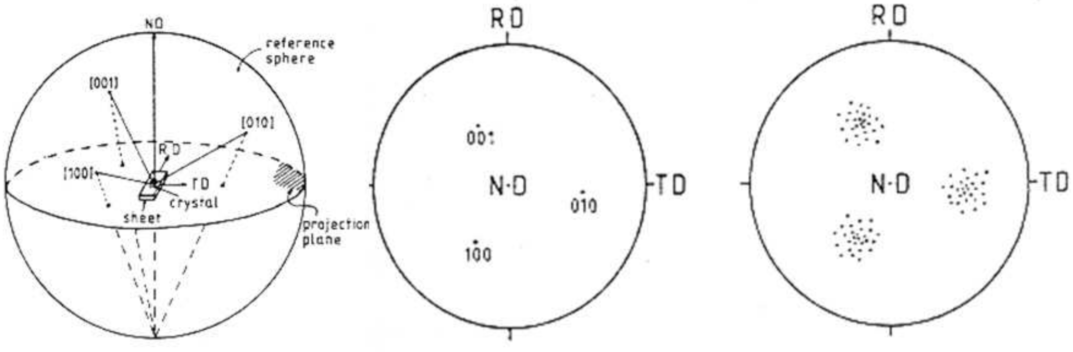

Fig.4.4 Illustration of Pole Figures [38]

In our piezoelectric poly-crystal study, we used two different sets of textures for the materials: random orientations (Fig.4.5a) and a strong texture (adopted from a rolled Al alloy texture) (Fig.4.5b). We also calculate a single crystal [001] using the same model.

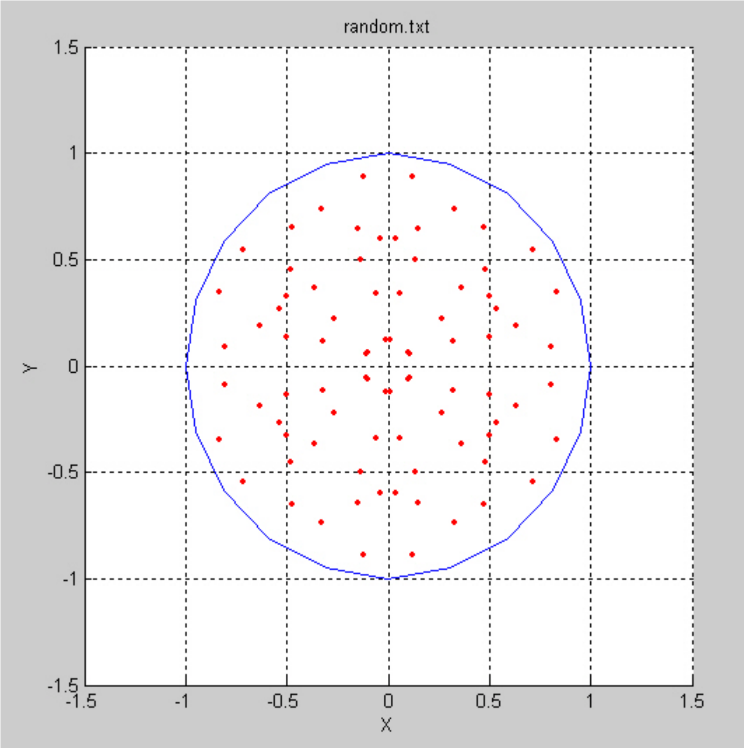

(a)

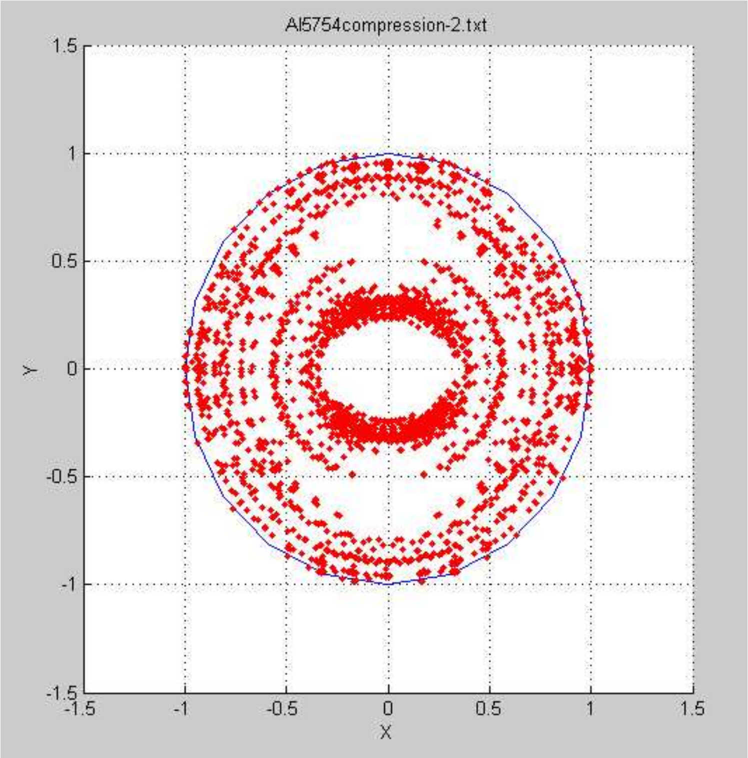

(b)

Fig. 4.5 Pole figures for (a) random orientation and (b) rolled Al alloy texture

4.4 Results and discussions

Fig.4.6 - Fig.4.8 show the results for random polarized sample, single crystal and highly polarized poly-crystal sample. For the random orientation sample (Fig.4.6), the overall polarization is zero. But for the highly polarized one (Fig.4.7), the overall polarization is [0.6, 0.6, 0.514] which is very close to [1, 1, 1]. If we treat all the polarization direction as [0, 0, 1] at local coordinates, then it means that the majority of grains' [0, 0, 1] axes (local coordinates) lie on [1, 1, 1] direction or very close to it at global coordinates.

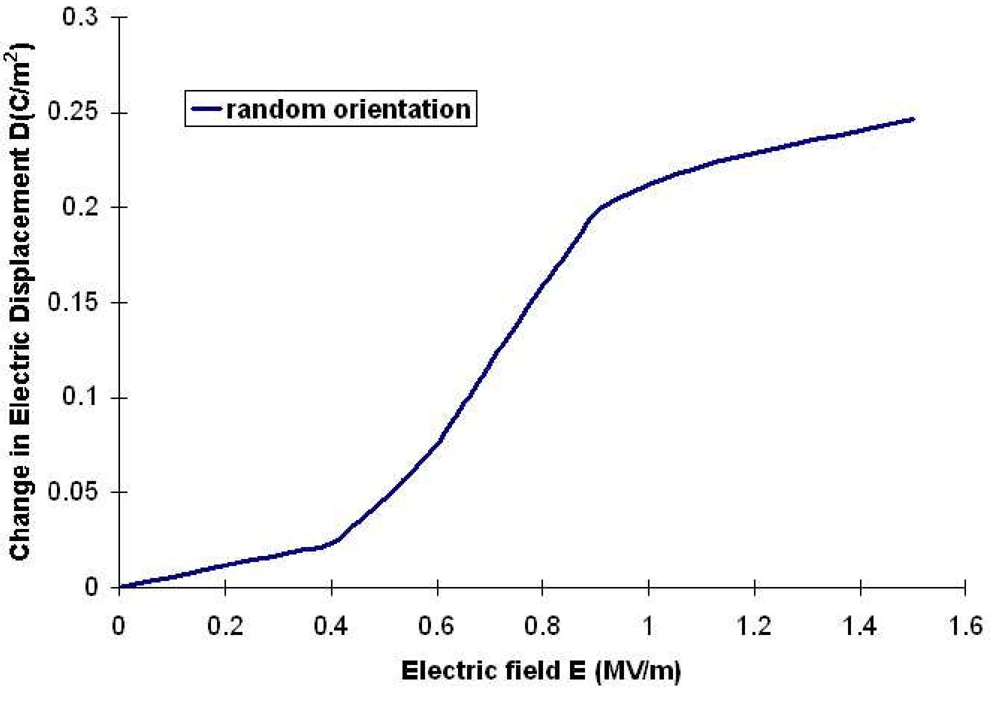

Fig. 4.6 Random orientation result

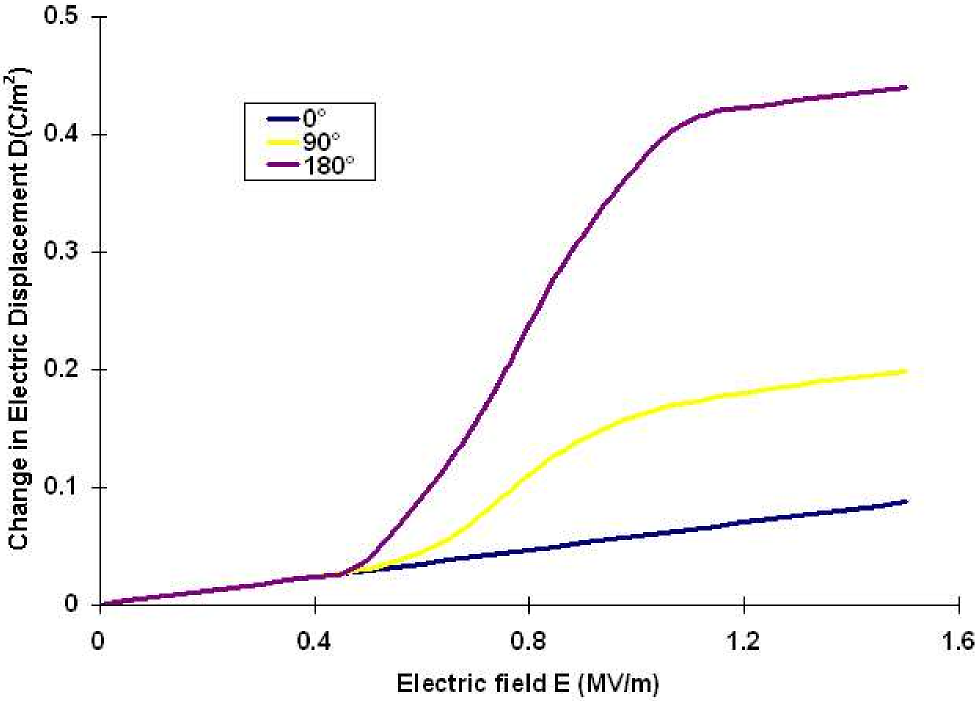

Fig. 4.7 Rolled Al alloy texture results under different loading angles

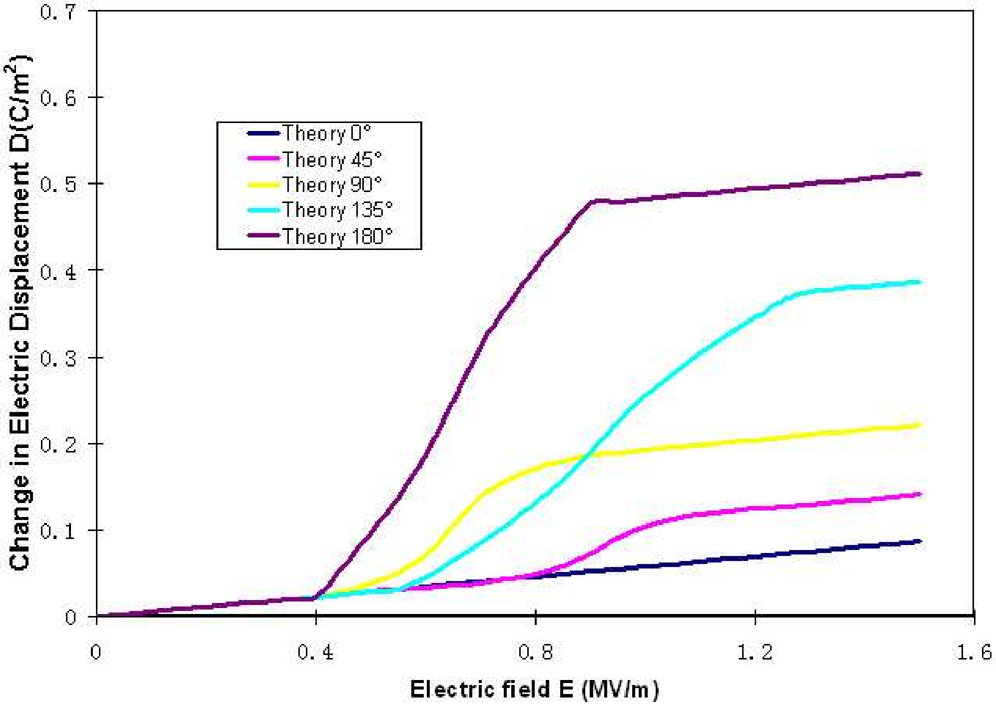

Fig. 4.8 Single crystal [001] results under different loading angles

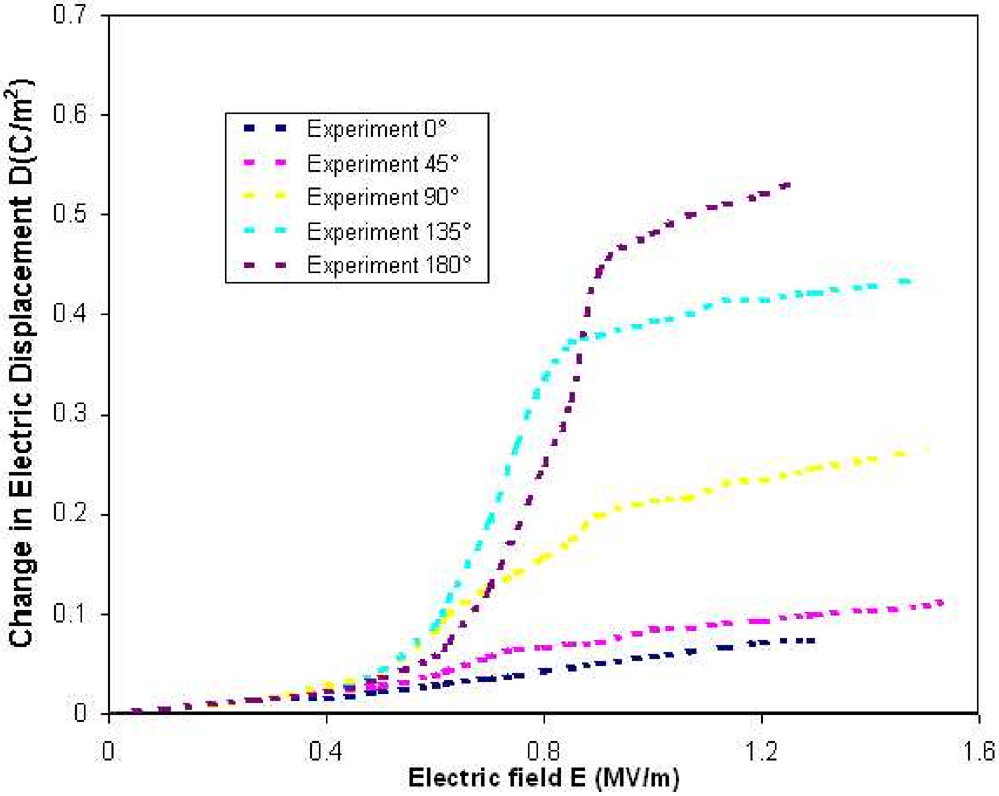

Fig. 4.9 Experimental data from Huber and Fleck [1].

We need an initial assumption of relationship between electric displacement and electric field for every single crystal. Here, we used a simple math model involves hyperbolic functions. Fig.4.10 is the electric displacement verses electric field curve of this assumption.

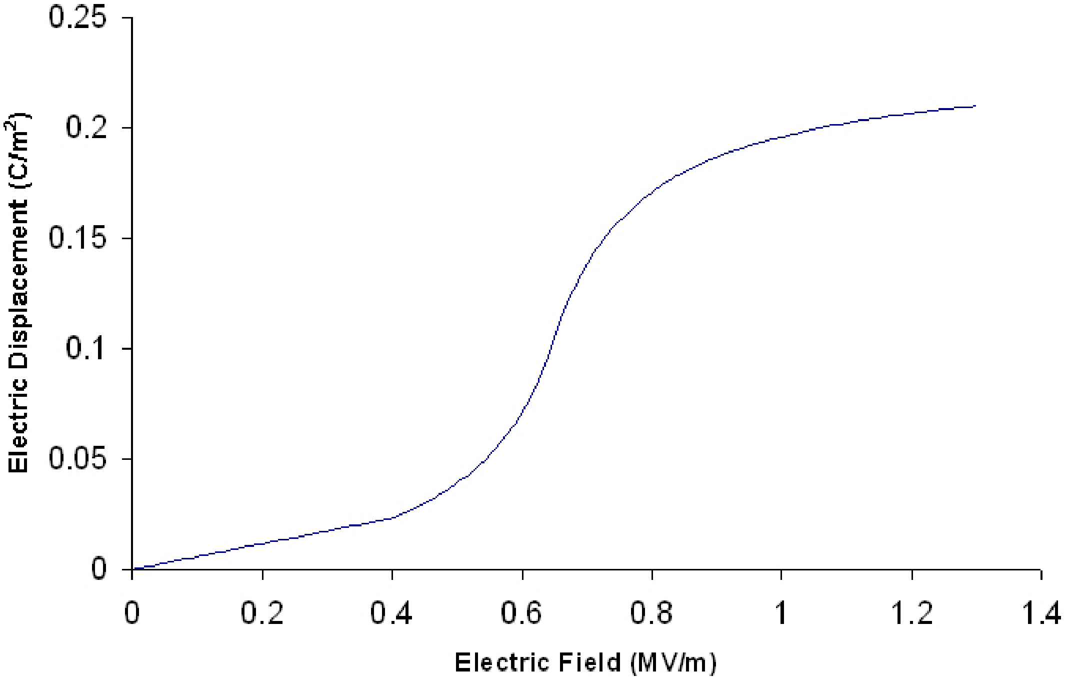

Fig. 4.10 Relationship of electric displacement and electric field assumption for single crystal

To be able to compare the texture model with experimental data, we reproduced Huber and Fleck's results in Fig. 4.9. From the comparison of the theoretical results and the experimental data, 0°, 90° and 180° curves fit well; 45° curve also fits reasonably. But 135° curve does not fit experimental data. It comes from initial assumptions. We assume it is a single crystal and all the grains can only have either 90° or 180° domain switch or does not switch at all. 45° and 135° forces have the least components on both 90° and 180° directions. The criterion for domains to switch is the component force on desirable direction reaches a certain level. So in 45° or 135° cases, in order to get domain switch, a greater external force is needed comparing to other cases.

4.5 Advantages and Drawbacks

The model requires a crucial input data which is the original texture orientation of the material. Using modern electron microscope, we can detect the orientation for each individual grain so that we can get the orientation map for the entire surface or even the 3-dimentional orientation density function (ODF) for the whole bulk material. The technique is called Electron Backscattered Diffraction (EBSD). The idea is to do a whole sample surface scan first using high magnification SEM; then use EBSD camera to get a Kikuchi Pattern for each grain; from each Kikuchi Pattern, the bands are identified and indexed; finally, the orientation matrix can be calculated and the Euler angles can be determined for each grain. After scanning the entire surface of the sample, the orientation map can be obtained; If enough samples for different layers of the material have been tested, the whole 3-dimentional ODF can be constructed.

An ideal experiment is to get the 3-D ODF of the ferroelectric material both before and after applying external forces including either mechanical forces or electric fields. Then exactly how the grains will response due to the external changes can be discovered and all the existing theoretical models can be tested.

For single crystals or for the highly polarized samples (strong texture), this model is very useful since the input orientation is much simpler compare to random polarized samples.

5. Micromechanics-Based Model for Temperature Effect on $BaTiO_3$

A micromechanics-based thermodynamic model is applied to study the piezoelectric and dielectric constants of $BaTiO_3$ crystals as a function of temperature upon the cooling from the Curie point. The formation of spontaneous polarization at the beginning of cooling provides dramatic change in the symmetry of the system. This plays an important role in the sudden change of piezoelectric constant d_{31} at the beginning of the cooling process. In this chapter, by considering the heterogeneous nature of the crystal at the beginning of the cooling due to spontaneous polarization, the micromechanics-based model is able to evaluate the piezoelectric coefficient d_{31}. To verify the new modified model, the dielectric constant k_{33} for a $BaTiO_3$ single crystal in terms of temperature is also calculated and compared with the existing micromechanics-based model in the literature [39]. It shows agreeable and improved result in dielectric constant k_{33} of $BaTiO_3$. Both dielectric and piezoelectric constants are also found to be consistent with the available experimental data.

5.1 Introduction

Above its Curie point, a ferroelectric single crystal is in its paraelectric phase. Upon the cooling from its Curie temperature, it experiences spontaneous polarization from a symmetric state to a less symmetric one. For instance, a pervoskite-type crystal such as

$BaTiO_3$ will have a cubic-to-tetragonal phase transition upon the cooling from its Curie temperature. Such a phase transition is also the source of piezoelectric effect of the crystal. Unlike other dielectric and piezoelectric properties, the piezoelectric coefficient d_{31} of $BaTiO_3$ crystal experiences a sudden change from zero (paraelectric stage) at the Curie point to a much higher absolute value just below the Curie point, and then reduces to a saturated value at the room temperature upon further cooling [27]. Even though the phenomenon has been observed a half century ago, proper modeling and explanations are falling short besides the rapid development of studying electro-mechanical coupling behavior of ferroelectric crystals using various approaches such as phenomenological methods [1, 19, 20, 40-42], energy approaches [43-45], and micromechanics approaches [2, 5-7, 14, 15, 21, 39, 46-53], among the others. Here we reexamine the problem by using the most recently developed micromechanics-based thermodynamic model [5-7, 21, 39, 47-53]. We noticed that without considering the effect of heterogeneous nature at the beginning of cooling from the Curie temperature, the piezoelectric constant d_{31} could not be simulated in such a way to be agreed with the experimental data. This is also the reason that no piezoelectric coefficient d_{31} has been properly addressed in terms of temperature [39] by using micromechanics-based models. In order to be able to solve the problem, we modified the existing micromechanics-based thermodynamic model by considering the effect of heterogeneous nature at the beginning of the cooling. With the new modified model, the piezoelectric coefficient d_{31} of a $BaTiO_3$ crystal in terms of temperature is obtained and compared with the available experimental data1. To validate the modified model, the dielectric constant k_{33} of $BaTiO_3$ crystal is also calculated and compared with the existing method [39]. The comparison agrees well with each other. The results for both dielectric and piezoelectric constants are also consistent with the experimental data [27].

In the past half century, micromechanics theory was mainly applied to study the mechanical behaviors of heterogeneous materials. Only in recent years, it has been brought into a broader aspect to study the coupling behaviors of materials such as Thermo-mechanical couplings of shape memory alloys [54, 55] and electro-mechanical coupling behavior of piezoelectrics/ferroelectrics [2, 5-7, 14, 15, 21, 39, 46-53]. The key issue in micromechanics theory is to identify the eigen field of the system, then various approaches such as Mori-Tanaka [56], differential scheme [57], or self-consistent [58-60] methods can be used. Regardless of differences among all approaches, Eshelby's [61] S-tensor is ready to be used in the sense of mechanical behavior of the system. For ferroelectrics, the electromechanical couplings need to be incorporated into the constitutive relations of the system. As a result, the Eshelby's S-tensor needs to be determined according to the coupled constitutive relations. Unfortunately most piezoelectric Eshelby's S-tensors [62-64] with ellipsoidal shapes of inclusions are implicit with integrals, which is not the case for the original S-tensors. One of the exceptions is the lamellar structure, in which the piezoelectric S-tensor can be obtained explicitly [5, 39, 49]. By observing the microstructure of $BaTiO_3$ single crystal, it has been found that the domain morphology also follows the lamellar structure [25, 26, 65].

This is a consequence of energy minimization, as it can be concluded from compatibility consideration, or from micromechanics as indicated in Liu, et al [66]. Such domain morphology makes the modeling easier and analytical solution possible.

To study the piezoelectric properties of ferroelectric crystals as a function of the temperature, the phase transition due to spontaneous polarization plays a key role in micromechanics-based model. Here we consider $BaTiO_3$ single crystal which belongs to perovskite crystal structure family ABO_3. Above the Curie point, it has a cubic structure which gives a paraelectric (non-piezoelectric) state. Upon the cooling from the Curie point, the tetragonal phase with a spontaneous polarization will grow at the expense of the parent cubic phase. A schematic sketch of such a cubic-to-tetragonal transition of a $BaTiO_3$ unit cell is given in Fig.2.1. As a result, the system can be treated as a two-phase composite with the cubic phase as parent phase, and the tetragonal phase as the secondary phase. Then the micromechanics theory can be utilized to study the electromechanical coupling behavior of ferroelectric if the volume fraction of the new growing phase can be determined.

We seek to reformulate the problem of a ferroelectric spontaneous polarization, similar to Su and Weng's [39] previous work and lay out the basic procedure of micromechanics-based irreversible thermodynamic principle used in modeling electro-mechanical behavior of ferroelectrics. Then, by considering the evolution of microstructure due to cubic-to-tetragonal phase transition during the cooling, and the impact on symmetry of such an evolution, the piezoelectric constant of d_{31} can be obtained in terms of temperature. This completes the micromechanics modeling on d_{31} in the literature.

5.2 Constitutive equations

Following Ikeda [67] formula, the linear electromechanical constitutive equations of a piezoelectric crystal can be written in tensorial notation as

$$\varepsilon_{ij} = s_{ijkl}^{(E)}\sigma_{kl} + d_{nij}E_n \text{, or} \qquad \varepsilon = s^{(E)}\sigma + d^T\mathrm{E} \tag{5.1a}$$

$$D_m = d_{mkl}\sigma_{kl} + k_{mn}^{(\sigma)}E_n \text{, or} \quad \mathrm{D} = d\sigma + k^{(\sigma)}\mathrm{E} \tag{5.1b}$$

where σ and E are stress tensor and electric field, ε and D are the strain and the electric displacement, s(E) and k(σ) are the elastic compliance measured at constant electric field and dielectric permittivity tensors measured at constant stress, d is the piezoelectric compliance tensor, and the superscript T denotes as the transport.

For convenience, these equations can be rewritten in a matrix format as

$$\begin{bmatrix} \varepsilon \\ D \end{bmatrix} = \begin{bmatrix} s & d^T \\ d & k \end{bmatrix} \begin{bmatrix} \sigma \\ E \end{bmatrix} \qquad \text{or} \quad \mathrm{Y} = \mathrm{MX} \tag{5.2}$$

where in Nye's [68] contracted notation,

$$\begin{aligned} Y &= (\varepsilon_1, \varepsilon_2, \varepsilon_3, \varepsilon_4, \varepsilon_5, \varepsilon_6, D_1, D_2, D_3)^T \\ X &= (\sigma_1, \sigma_2, \sigma_3, \sigma_4, \sigma_5, \sigma_6, E_1, E_2, E_3)^T \end{aligned} \quad . \tag{5.3}$$

In this unified notation, X serves as the external load such as mechanical stress and/or electric field loads and Y as the response. The superscript T denotes the matrix transpose. And M is the electromechanical compliances matrix. When a $BaTiO_3$ crystal is in paraelectric phase above the Curie temperature, it possesses a cubic symmetric structure, and the components of M then can be specified as

$$M_0 = \begin{bmatrix} s_{11} & s_{12} & s_{12} & 0 & 0 & 0 & 0 & 0 & 0 \\ s_{12} & s_{11} & s_{12} & 0 & 0 & 0 & 0 & 0 & 0 \\ s_{12} & s_{12} & s_{11} & 0 & 0 & 0 & 0 & 0 & 0 \\ 0 & 0 & 0 & s_{44} & 0 & 0 & 0 & 0 & 0 \\ 0 & 0 & 0 & 0 & s_{44} & 0 & 0 & 0 & 0 \\ 0 & 0 & 0 & 0 & 0 & s_{44} & 0 & 0 & 0 \\ 0 & 0 & 0 & 0 & 0 & 0 & k_{11} & 0 & 0 \\ 0 & 0 & 0 & 0 & 0 & 0 & 0 & k_{11} & 0 \\ 0 & 0 & 0 & 0 & 0 & 0 & 0 & 0 & k_{11} \end{bmatrix} \tag{5.4}$$

where the subscript 0 of M denotes as the parent paraelectric phase, and there is no piezoelectric effect and d = 0. Upon cooling from the Curie point, the crystal experiences a cubic-to-tetragonal transition. For the tetragonal ferroelectric phase (denoted as phase 1 here and after), it has the 4mm symmetry and the electro-mechanical compliance matrix M1 is approximated in measurement as

$$M_1 = \begin{bmatrix} s_{11} & s_{12} & s_{13} & 0 & 0 & 0 & 0 & 0 & d_{31} \\ s_{12} & s_{11} & s_{13} & 0 & 0 & 0 & 0 & 0 & d_{31} \\ s_{13} & s_{13} & s_{33} & 0 & 0 & 0 & 0 & 0 & d_{33} \\ 0 & 0 & 0 & s_{44} & 0 & 0 & 0 & d_{15} & 0 \\ 0 & 0 & 0 & 0 & s_{44} & 0 & d_{15} & 0 & 0 \\ 0 & 0 & 0 & 0 & 0 & s_{66} & 0 & 0 & 0 \\ 0 & 0 & 0 & 0 & d_{15} & 0 & k_{11} & 0 & 0 \\ 0 & 0 & 0 & d_{15} & 0 & 0 & 0 & k_{11} & 0 \\ d_{31} & d_{31} & d_{33} & 0 & 0 & 0 & 0 & 0 & k_{33} \end{bmatrix}. \tag{5.5}$$

The inverse of the constitutive relation in Eq. (5.2) can be obtained as

$$X = LY \quad \text{or} \quad X_i = L_{ij}Y_j\text{, sum over } i, j = 1,2,...,9 \tag{5.6}$$

where $L = M^{-1}$.

5.3 Spontaneous polarization

The occurrence of electro-mechanical coupling behavior of a ferroelectric crystal is mainly due to the spontaneous polarization or cubic-to-tetragonal phase transformation (See Fig.5.1) upon cooling from the Curie temperature. Such a spontaneous polarization can be treated as the source of an eigen field in the micromechanics model. At the paraelectric stage, the system possesses cubic symmetry and no eigen field exists. Once the spontaneous polarization occurs upon the cooling, the new tetragonal phase evolves at the expense of the cubic phase. By taking the polarization direction as axis 3, the eigen field due to such a spontaneous polarization forms the polarization strain of

$$\varepsilon^{sp} = [(a-a_0)/a_0,(a-a_0)/a_0,(c-a_0)/a_0,0,0,0]^T \tag{5.7}$$

and the electric polarization of

$$P^{sp} = [0,0,P_s]^T \tag{5.8}$$

where the superscripts sp denote for spontaneous polarization, and a_0, a and c are the lattice constants of the cubic and tetragonal unit cells, respectively. In the unified matrix notation, it becomes

$$Y^{sp} = \begin{bmatrix} \varepsilon^{sp} \\ P^{sp} \end{bmatrix} = [(a-a_0)/a_0,(a-a_0)/a_0,(c-a_0)/a_0,0,0,0,0,0,P_s]^T \ . \tag{5.9}$$

5.4 Gibbs free energy

Spontaneous polarization is due to a thermodynamic driving force by reduction of the Gibbs free energy of the dual-phase system during cooling. The Gibbs free energy of the dual-phase system can be casted into two terms:

$$G(T,\bar{X},c_1) = G_{ch}(T,c_1) + G_p(\bar{X},c_1) \quad , \qquad (5.10)$$

where $G_{ch}(T,c_1)$ is a chemical free energy with a volume fraction of the tetragonal phase c_1 at temperature T , and $G_p(\bar{X},c_1)$ is the electro-mechanical potential energy under the external loading $\bar{X}$.

According to Su and Weng's previous work [39], the change of chemical free energy with respect to cubic-to-tetragonal transition upon cooling from Curie point is given as

$$\Delta G_{ch}(T,c_1) = -c_1\left\{\Delta s(T_c)\cdot(T-T_c) + \Delta c_p\left[T\ln\frac{T}{T_c} - (T-T_c)\right]\right\} \quad , \qquad (5.11)$$

where $\Delta s(T_c) = s^T(T_c) - s^C(T_c)$, representing the difference of entropy of the tetragonal and the cubic phase at the Curie temperature Tc, and Δc_p is the difference of their specific heat.

And the change of electromechanical potential energy of a ferroelectric crystal with polarization strain ε^{sp} and spontaneous polarization P^{sp} or Y^{sp} follows as

$$\Delta G_p(\bar{X},c_1) = -\frac{1}{2}c_1[\bar{X}_1^T Y^{sp} + \bar{X}^T(Y^{sp} + Y^*)] \qquad (5.12)$$

where $\bar{X}_1$ is the average stress and electric field of the tetragonal phase 1, and $\bar{Y}^* = \left(\varepsilon^*, P^*\right)^T$ is Eshelby's equivalent electromechanical eigen field introduced to replace M_1 by M_0 in Eshelby's equivalent transformation principle. The detailed derivation of equation (5.12) is quite lengthy and can be found in the Appendices in Li and Weng [6]. Their original derivation was developed based upon the domain switch which can be equally applied to spontaneous polarization here. Following the fundamental micromechanics approach, the average electromechanical field of the tetragonal phase 1 and the equivalent eigen field are dependent on the applied external field $\overline{X}$, the eigen field Ysp due to spontaneous polarization, and the electromechanical properties M_0 and M_1 of the cubic and the tetragonal phase, respectively.

$$\begin{aligned} \overline{X}_1 &= \overline{X} + \widetilde{X} + \overline{X}^{pt} = B_1 Q \overline{X} + (c_1 B_1 Q - I) B_1 L_0 (I - S) Y^{sp}, \\ Y^* &= -[\Delta L (c_1 I + c_0 S) + L_0]^{-1} \Delta L [L_0^{-1} \overline{X} - c_0 (I - S) Y^{sp}], \end{aligned} \qquad (5.13)$$

with

$$B_1 = [I + L_0 (I - S)(M_1 - M_0)]^{-1}, \quad \text{and} \quad Q = (c_1 B_1 + c_0 I)^{-1}, \qquad (5.14)$$

where B_1 is the electromechanical field concentration tensor for a single inclusion with the moduli L_1 embedded in an infinite medium with electromechanical moduli of L_0, S is the Eshelby-type piezoelectric S-Tensor (Appendix A.1), and I is the symmetric fourth-order identity tensor. For a lamellar structure, Li [49] has derived the explicit expression of the Eshelby-type piezoelectric S-tensor which will be used in this work. By substituting eq. (5.13) into eq. (5.12) and following lengthy algebra, the change of the potential energy can be simplified as

$$\Delta G_p(\overline{X}, c_1) = -\frac{1}{2} c_1 [\overline{X}^T H_1 \overline{X} + \overline{X}^T H_2 Y^{sp} + {Y^{sp}}^T H_3 Y^{sp}], \qquad (5.15)$$

where

$$\begin{aligned} &H_1 = -P \Delta L L_0^{-1} = -P \Delta L M_0, \quad \text{with} \quad P = [\Delta L (c_1 I + c_0 S) + L_0]^{-1}, \quad \Delta L = L_1 - L_0; \\ &H_2 = F^T + 2I + R, \quad \text{with} \quad F = c_0 L_0 (I - S) P \Delta L M_0, \quad \text{and} \quad R = c_0 P \Delta L (I - S); \\ &H_3 = c_0 \{L_0 (S - I)[I + c_0 P \Delta L (I - S)]\}^T. \end{aligned}$$

$$(5.16)$$

5.5 Kinetic equation due to spontaneous polarization

Once the spontaneous polarization occurs in a crystal upon cooling from Curie temperature, the system can be treated as a two-phase composite system. Upon the further cooling, more tetragonal phase will continue to evolve, and the volume concentration of newly evolved tetragonal phase c_1 will increase at the expense of the parent cubic phase c_0, until c_1 reaches 1 at the saturation stage ($c_0+c_1=1$). Such an evolution process follows an irreversible thermodynamics principle. According to the second law of the irreversible thermodynamics principle, the change of Gibbs free energy under the thermo-electro-mechanical loading must satisfy the following inequality (Rice [69])

$$\left.\frac{\partial \Delta G(T,\overline{X},c_1)}{\partial c_1}\right|_{(T,\overline{X})} dc_1 \leq 0 \quad . \tag{5.17}$$

The equality holds only for a reversible process ($dc_1 = 0$). The thermodynamic driving force for the cubic-to-tetragonal transition is given as [39]

$$f_{drv} = -\left.\frac{\partial \Delta G}{\partial c_1}\right|_{(T,\overline{X})} = -\frac{\partial}{\partial c_1}[\Delta G_{ch}(T,c_1)|_T + \Delta G_p(\overline{X},c_1)|_{\overline{X}}]. \tag{5.18}$$

From Eq. (5.11), the first term of Eq. (5.18) can be simply obtained as

$$-\frac{\partial}{\partial c_1}\Delta G_{ch}(T,c_1) = \Delta s(T_c)\cdot(T-T_c) + \Delta c_p\left[T\ln\frac{T}{T_c} - (T-T_c)\right]. \tag{5.19}$$

The second term of Eq. (5.18) also can be obtained after some lengthy algebra [39] in matrix form as

$$-\frac{\partial \Delta G_p(\overline{X}, c_1)}{\partial c_1}\Big|_{\overline{X}} = \frac{1}{2}(\overline{X}^T A \overline{X} + \overline{X}^T B Y^{sp} + Y^{sp^T} C Y^{sp}) \tag{5.20}$$

where

$$\begin{aligned}
A &= H_1 + c_1 \frac{\partial H_1}{\partial c_1} = H_1 - c_1 H_4 M_0 \\
&\quad \text{with} \quad H_4 = P\Delta L(I-S)P\Delta L, \\
B &= H_2 + c_1 \frac{\partial H_2}{\partial c_1} \\
&= H_2 - \frac{c_1}{c_0}(H_2 - 2I) - c_1 c_0 [M_0 H_4{}^T (I - S^T) L_0 + H_4 (I - S)], \\
C &= H_3 + c_1 \frac{\partial H_3}{\partial c_1} \\
&= H_3 - \frac{c_1}{c_0} H_3 + c_1 c_0 (P\Delta L + c_0 H_4)^T (I - S^T)^2 L_0.
\end{aligned} \tag{5.21}$$

In order to grow new tetragonal phase, the thermodynamic driving force needs to overcome the resistance force coming from the surface/interface energy and the energy dissipation associated with the phase growth. The interface energy is given as

$$\Delta G_s = \gamma_s A_1 / V = \gamma_s (A_1 / V_1)(V_1 / V) = c_1 \gamma_s (A_1 / V_1), \tag{5.22}$$

where γ_s stands for the interface energy density, A_1 stands for the interface area, and V_1 stands for the total volume of the new phase in the system.

As described in Su and Weng's work [39], various dissipation energies have been adopted in the literature. When the volume concentration of the new product phase is low, the dissipation energy can be assumed as a linear function which is the case in the modeling of shape memory alloys by Sun, et al [70-72]. But for the entire transformation process, the parent phase will eventually transform to the product phase completely, a nonlinear function is essential to model such an evolution process. In general, the dissipation energy has been assumed as an exponential function for nonlinear behavior of ferroelectrics [5-7, 39, 49-52]. In this work, we have found that a logarithm function is more suitable for the modeling of piezoelectric constant d_{31}, and it also agrees well with an exponential function assumption used by Su and Weng [39] to calculate dielectric constant k_{33}. Here the dissipation energy is assumed as

$$\Delta G_d = b\ln a - b\ln(a - c_1) \tag{5.23}$$

where b and a are constants. This energy term can be approximated as a linear function at low concentration of c_1. Then the thermodynamic resistance force can be obtained as

$$f_{res} = \frac{\partial(\Delta G_s + \Delta G_d)}{\partial c_1} = \gamma_s(A_1/V_1) + \frac{b}{a - c_1}. \tag{5.24}$$

Once the thermodynamic driving force overcomes the resistance force, the new tetragonal phase will grow, and the kinetic equation governing the evolution of such phase transformation can be casted as

$$f_{drv} = f_{res} \tag{5.25}$$

or

$$\begin{aligned}
&\frac{1}{2}[\overline{X}^T A\overline{X} + \overline{X}^T BY^{sp} + Y^{sp^T} CY^{sp}] \\
&\quad + \Delta s(T_C)(T - T_C) + \Delta c_p[T\ln\frac{T}{T_C} - (T - T_C)] \\
&\quad = \gamma_s(A_1/V_1) + \frac{b}{a - c_1}.
\end{aligned} \tag{5.26}$$

Under the pure cooling process ($\overline{X} = 0$), the temperature starts at the Curie point with T=T$_C$, and the volume fraction of tetragonal phase jumps from zero to some initial value c$_{1i}$, then the Eq. (5.26) at this initial condition can be reduced to

$$\frac{1}{2}Y^{sp^T}C_0Y^{sp}=\gamma_s(A_1/V_1)+\frac{b}{a-c_{1i}} \quad \text{or} \quad \gamma_s(A_1/V_1)=\frac{1}{2}Y^{sp^T}C_0Y^{sp}-\frac{b}{a-c_{1i}}, \tag{5.27}$$

where C$_0$ is the value of C at $c_1=c_{1_i}$. By substituting Eq. (5.27) back into Eq. (5.26), the kinetic equation of evolution under the pure cooling is obtained as

$$\frac{1}{2}Y^{sp^T}(C-C_0)Y^{sp}+\Delta s(T_C)(T-T_C)+\Delta c_p[T\ln\frac{T}{T_C}-(T-T_C)]=\frac{b}{a-c_1}-\frac{b}{a-c_{1_i}}. \tag{5.28}$$

From the kinetic equation (5.28), the evolution of volume concentration of tetragonal phase c$_1$ can be evaluated upon the cooling.

This evolution will also provide the change of effective electromechanical properties of the system in terms of temperature. Following the classical micromechanics used in elasticity [73], the overall effective electromechanical compliance is given as

$$M=(c_0M_0+c_1M_1B_1)(c_0I+c_1B_1)^{-1}, \tag{5.29}$$

where B$_1$ is given in Eq. (5.14).

5.6 Results and discussions

Before we apply the developed micromechanics theory to evaluate the piezoelectric constant d$_{31}$, we first need to validate our approach with the existing micromechanics method and the experimental data. So far, the most relevant study regarding to the temperature effects on certain electromechanical properties using micromechanics approach is by Su and Weng [39]. Here we recalculated the dielectric constant k$_{33}$ by using the modified approach. The material properties and constants are given in Table 5.1. All of the parameters are chosen to be the same as in Su and Weng's work [39] except the constants a and b associated with dissipation energy. The evolution of volume concentration of tetragonal phase is shown in Fig.5.1. The solid line indicates our calculation, and the solid-dots by Su and Weng [39]. Fig.5.2 shows the comparison of dielectric constant k_{33} of $BaTiO_3$ in terms of cooling temperature among the experimental data [23], Su and Weng's model [39] and our calculation. Both models agree well with the experimental measurement. The only difference between Su and Weng's [39] model and ours is the assumption of dissipation energy. In their model, an exponential function is adopted, while in this work, a logarithm function is assumed.

Table 5.1 Materials properties and constants

Properties	**Cubic phase**	**Tetragonal phase**
$s_{11}(10^{-12} m^2 / N)$	8.33	8.05
$s_{12}(10^{-12} m^2 / N)$	-2.68	-2.35
$s_{13}(10^{-12} m^2 / N)$		-5.24
$s_{33}(10^{-12} m^2 / N)$		15.7
$s_{44}(10^{-12} m^2 / N)$	9.24	18.4
$s_{66}(10^{-12} m^2 / N)$		8.84
k_{11} (k_0=8.85×10^{-12}F/m)	10,000×k_0	2920×k_0
k_{33}		168×k_0
$d_{31}(10^{-12} C / N)$		-34.5
$d_{33}(10^{-12} C / N)$		85.6
$d_{15}(10^{-12} C / N)$		392

$T_C = 120°C, P_S = 0.16 C / m^2$

$\Delta s(T_C) = -1.25 \times 10^4 J / m^3 / °C, \Delta c_p = 12.4 \times 10^4 J / m^3 / °C$

$[\varepsilon^{sp}] = [-6.54 \times 10^{-4}, -6.54 \times 10^{-4}, 1.00 \times 10^{-3}, 0, 0, 0]$

a=1.01, b=35986.57 J / m^3,

c_{1i} = 0.20, $|d_{31}|_{max}$=223×$10^{-12} C / N$

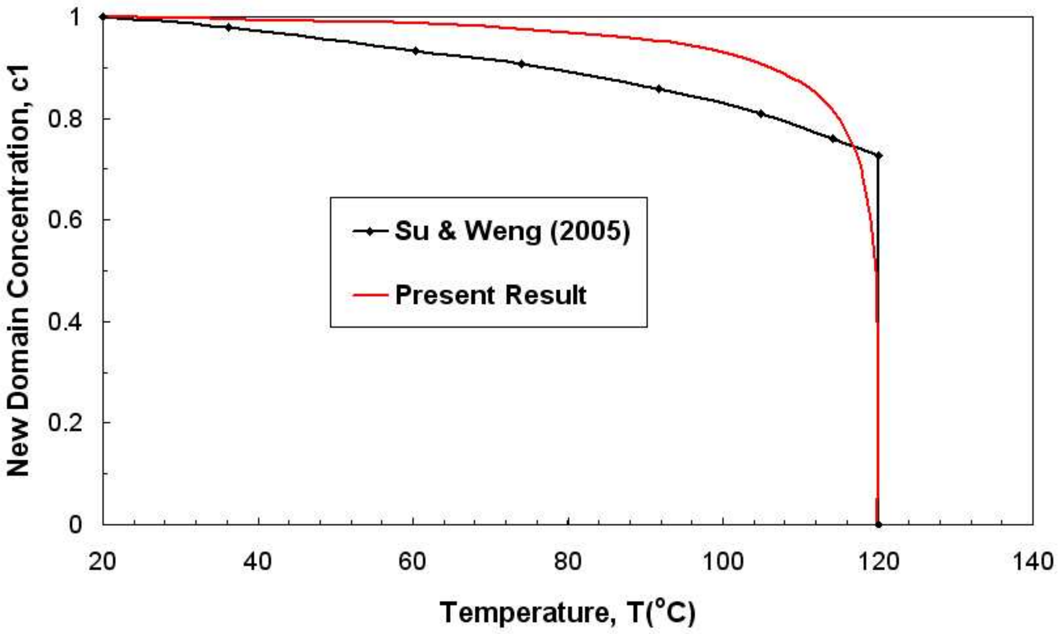

Fig. 5.1 Comparison of the evolution of the new tetragonal phase concentrations upon the cooling (solid line – present model; solid line with dot – Su and Weng [39])

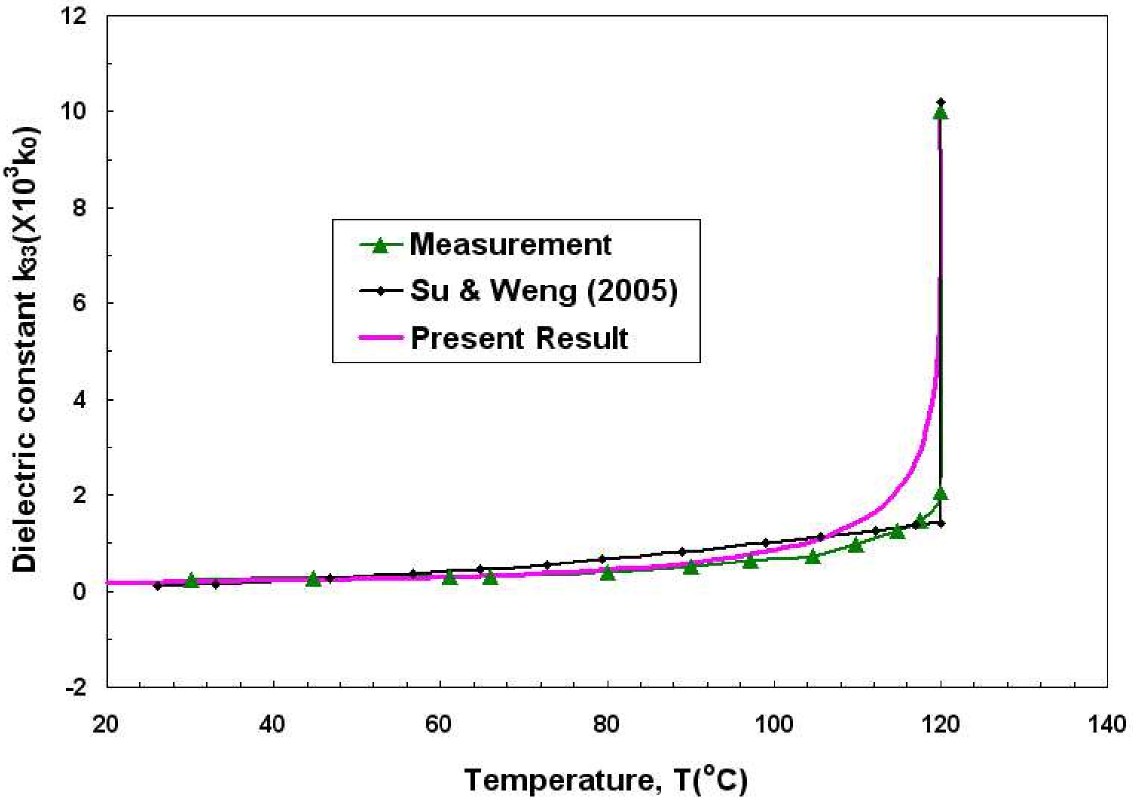

Fig. 5.2 Comparison of the dielectric constant k_{33} of a BaTiO3 crystal upon cooling: Merz's measurement [23], Su and Weng's model [39] and present model.

Then we apply our modified model to evaluate piezoelectric constant d_{31} which has not been studied using micromechanics approach due to the difficulty of its abrupt change right below the Curie point. Such a sudden change is mainly due to the heterogeneity and instability of the microstructure right after the initial spontaneous polarization. Both cubic and tetragonal phases coexist and the piezoelectric constant d_{31} of the system reaches the highest absolute value at that point. In general, such abrupt change of piezoelectric coefficient upon cooling cannot be modeled by using original piezoelectric constant $d_{31}=0$ of the paraelectric cubic phase above the Curie point as usual. By realizing such a physical meaning of its abrupt change, here we assume that the two-phase system consists of the new tetragonal ferroelectric phase 1 and the instable transition phase 0 with the maximum piezoelectric constant d_{31} right below the Curie point at $c_1 = c_{1_i}$. The determination of the maximum piezoelectric constant d_{31} for instable transition phase 0 is obtained based on the experimental data at the initial condition of $c_1 = c_{1_i}$. These values are given at the end of Table 5.1. The comparison on piezoelectric constant d_{31} of $BaTiO_3$ between experimental data [27] and our calculation is shown in Fig.5.3. Again both curves agree well with each other.

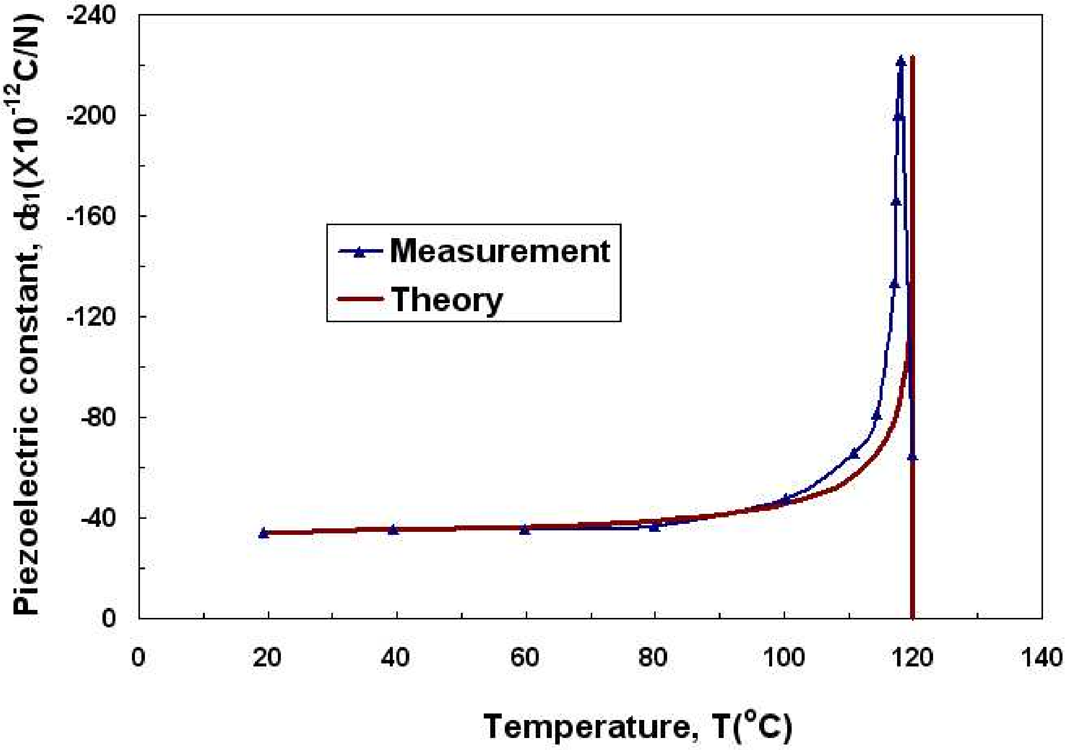

Fig. 5.3 Piezoelectric constant d_{31} of a $BaTiO_3$ upon cooling from Curie temperature: theory vs Caspari and Merz's measurement [27].

5.7 Conclusions

A modified micromechanics approach based on irreversible thermodynamics principle has been applied to study piezoelectric constant d_{31} upon cooling from Curie temperature. To validate the modified micromechanics model, the dielectric constant k_{33} was first calculated and compared to the existing micromechanics model [39] and the experimental data. The comparison shows promising agreement among the three. Then by considering the heterogeneous and instability nature at the beginning of the cooling, piezoelectric constant d_{31} was evaluated and compared with the experimental data which has been missing in Su and Weng's [39] work. The result agrees well with the measurement. Also the proposed model with other existing micromechanics models will provide the complete set of the piezoelectric, dielectric and elastic properties of ferroelectric crystals upon cooling.

5.8 Advantages and Drawbacks

When we try to use this model to deal with $BaTiO_3$ nanowires problems, the size limit for ferroelectricity we got is around 50nm which is way too high compare to current available experiment data. The size limitation of micromechanics model comes from several areas. One of them probably comes from the assumption of Eshelby's S tensor since typical S tensor is derived from semi-infinite bulk material which is either 2-dimentional or 3-dimentional. When dealing with 1-dimentional nanowires or nanoparticles, the foundation of micromechanics model probably won't work in such finite ranges although some researchers suggest some modifications could solve this problem [74].

6. 1-3 Piezoelectric Composites under Electric Loading

In this Chapter, a micromechanics approach based on Chapter 5 is extended to study PZT fiber composite material under external electric loading. To be able to study the hysteresis electric displacement vs electric field and the butterfly shaped strain and electric field relations of 1-3 ferroelectric composites, a two-level micromechanics approach is developed. The first level is at ferroelectric fiber inclusion level, in which, under external loading, domain switch may occur. The second level is on the larger scale consisting of both piezoelectric fibers and electric inactive polymer matrix. At the first level, the ferroelectric fibers alone can be treated as a two-phase composite consisting the parent phase and switched phase. Then a micromechanics based on irreversible thermodynamic principle developed in Chapter 5 can be applied to account for the nonlinear electro-mechanical coupling behavior of the fibers. At the second level, again the original micromechanics model for two-phase composites with piezoelectric fibers and inactive polymer can be adopted to study the overall behavior of the system. The results will be compared with Zhao's experimental data [22]. In Ping's thesis, the electro-mechanical response of 1-3 piezoelectric composites with PZT5A1 fibers embedded in epoxy matrix has been tested under compression and electric field loading, respectively. Since the micromechanical modeling has been carried out under compressive loading condition by Zhao and Li [21], here the focus will be on hysteresis behavior of ferroelectric composites under the electric field loading. When the electric field is applied to the composites at the angle θ to the polarization and fiber directions of PZT fibers, its nonlinear electro-mechanical response is dependent on such an angle. The experimental results indicate that as the loading direction changes from 0^o, to 30^o, 45^o, 60^o, and finally 90^o to the original poling direction (which is also the PZT fiber direction), the magnitude of the electric displacement and mechanical strain of the system all decease and the electrical response will diminish to zero at 90^o.

6.1 Micromechanics Modeling for Piezoelectric Fibers

A micromechanics based model for ferroelectric ceramics alone has been introduced in Chapter 5. We will use the same model to study the nonlinear behavior of ferroelectric fibers at the first level before we get into composite part. We will establish the non-linear coupling constitutive relations of PZT fibers under external electric loading. To be able to recapture some parts in Chapter 5 and have easy transition, equations (5.3), (5.13) and (5.14) are listed here again.

$$\begin{aligned} Y &= (\varepsilon_1, \varepsilon_2, \varepsilon_3, \varepsilon_4, \varepsilon_5, \varepsilon_6, D_1, D_2, D_3)^T \\ X &= (\sigma_1, \sigma_2, \sigma_3, \sigma_4, \sigma_5, \sigma_6, E_1, E_2, E_3)^T \quad . \end{aligned} \tag{5.3}$$

$$\begin{aligned} \overline{X}_1 &= \overline{X} + \widetilde{X} + \overline{X}^{pt} = B_1 Q \overline{X} + (c_1 B_1 Q - I) B_1 L_0 (I - S) Y^{ds}, \\ Y^* &= -[\Delta L (c_1 I + c_0 S) + L_0]^{-1} \Delta L [L_0^{-1} \overline{X} - c_0 (I - S) Y^{ds}], \end{aligned} \tag{5.13}$$

where

$$B_1 = [I + L_0 (I - S)(M_1 - M_0)]^{-1}, \quad \text{and} \quad Q = (c_1 B_1 + c_0 I)^{-1} , \tag{5.14}$$

Here S is Eshelby's tensor for domain switch that is different from the S tensor used in Chapter 5 which is for spontaneous polarization (Appendix A.2). When the electromechanical moduli of the parent and switched domains do not differ significantly in the global axes, one may take $L_1 = L_0$ in Equation (5.13). Then B1 = I and Y* = 0, and

$$\widetilde{X} + \overline{X}^{pt} = -(1-c_1)L_0(I-S)Y^{ds} \tag{6.1}$$

The constitutive equations we need here are also different from (5.1a) and (5.1b).

$$\sigma = c\varepsilon - h^T \mathrm{D} \tag{6.2a}$$

$$\mathrm{E} = -h\varepsilon + \beta \mathrm{D} \tag{6.2b}$$

The relationship between these coefficients is the following,

$$\begin{bmatrix} c_{6X6} & -h^T{}_{6X3} \\ -h_{3X6} & \beta_{3X3} \end{bmatrix} = \begin{bmatrix} s_{6X6} & d^T{}_{6X3} \\ d_{3X6} & k_{3X3} \end{bmatrix}^{-1} \tag{6.3}$$

Equation (6.1) is derived from Matrix notation so that we can multiply out L_0 and (I-S) in the following way,

$$\begin{bmatrix} (I-S)^1{}_{6X6} & (I-S)^2{}_{6X3} \\ (I-S)^3{}_{3X6} & (I-S)^4{}_{3X3} \end{bmatrix} \tag{6.4}$$

$$\widetilde{\sigma} + \overline{\sigma}^{pt} = -(1-c_1)\{[c(I-S)^1 - h^T(I-S)^3]\cdot\varepsilon^{ds} + [c(I-S)^2 - h^T(I-S)^4]\cdot D^{ds}\} \tag{6.5}$$

$$\widetilde{E} + \overline{E}^{pt} = -(1-c_1)\{[-h(I-S)^1 + \beta(I-S)^3]\cdot\varepsilon^{ds} + [-h(I-S)^2 + \beta(I-S)^4]\cdot D^{ds}\} \tag{6.6}$$

The change of Gibbs free energy is given as, [12]

$$\Delta G = -\frac{1}{2}c_1[(\widetilde{\sigma} + \overline{\sigma}^{pt})\varepsilon^{ds} + (\widetilde{E} + \overline{E}^{pt})D^{ds}] - \frac{1}{2}c_1[\overline{\sigma}(2\varepsilon^{ds} + \varepsilon^*) + \overline{E}(2D^{ds} + D^*)] \tag{6.7}$$

The conjugate thermodynamic driving force for the evolution of the new domain whose microstructure is represented by its volume concentration c_1 of the new switched domain is given by

$$\begin{aligned} f_{drv} &= -\frac{\partial \Delta G}{\partial c_1} \\ &= -\frac{1}{2}(1-2c_1)\Big[\{[c(I-S)^1 - h^T(I-S)^3]\cdot \varepsilon^{ds} + [c(I-S)^2 - h^T(I-S)^4]\cdot D^{ds}\}\cdot \varepsilon^{ds} \\ &\quad + \{[-h(I-S)^1 + \beta(I-S)^3]\cdot \varepsilon^{ds} + [-h(I-S)^2 + \beta(I-S)^4]\cdot D^{ds}\}\cdot D^{ds}\Big] + \overline{\sigma}\varepsilon^{ds} + \overline{E}D^{ds} \end{aligned} \tag{6.8}$$

During domain growth, the domain wall has to overcome the resistance due to pinning by defects or inclusions, and this results in the energy dissipation. Surface energy will also form at the interface of the parent and product domains. This energy, however, is reversible upon reversed switch and, as such, can also be treated as a free energy. The interface energy is given by

$$\Delta G_s = \gamma_s A_1 / V = \gamma_s (A_1 / V_1)(V_1 / V) = c_1 \gamma_s (A_1 / V_1) = 2c_1 \gamma_s / t \tag{5.22}$$

where γ_s is the interface energy density, A_1 the total interface area and V_1 the total volume of the new domain in a unit volume of the system. When the new domain takes the lamellar morphology, t represents its average thickness.

Energy dissipation is found to increase with increasing domain concentration due to an increased level of domain interactions. This function, as required, has to reduce to zero when new domain is absent ($c_1 = 0$). We used the following function as dissipation energy in Chapter 5, this energy function is proper for Spontaneous Polarization which is a phase transformation from Cubic to Tetragonal. The energy functions are re-listed here so that we can compare when we use a new energy function for domain switch.

$$\Delta G_d = b\ln a - b\ln(a - c_1) \tag{5.23}$$

The resistance force then follows as

$$f_{res} = \frac{\partial(\Delta G_s + \Delta G_d)}{\partial c_1} = \gamma_s (A_1 / V_1) + \frac{b}{a - c_1}. \tag{5.24}$$

For 90^o and 180^o domain switches, we need a new dissipation energy function. In the latter discussion, it will show that we need a two step 90^o switches to produce electric displacement and butterfly strain curves. To have consistency, we still follow hyperbolic function family. For the 1st 90^o switch, the following is used as dissipation energy function,

$$\Delta G_{d1} = -b_1 \ln a_1 + b_1 \ln(a_1 + c_1) \tag{6.9}$$

While for the 2nd 90^o switch, this function becomes,

$$\Delta G_{d2} = -b_2 \ln a_2 + b_2 \ln(a_2 - c_1) \tag{6.10}$$

Then the resistance force will become

$$f_{res} = \frac{\partial(\Delta G_s + \Delta G_d)}{\partial c_1} = \gamma_s (A_1 / V_1) + \frac{b_1}{a_1 + c_1}, \left(or, \gamma_s (A_1 / V_1) - \frac{b_2}{a_2 - c_1} \right). \tag{6.11}$$

For the domain to grow, the resistance force must be overcome by the driving force, namely (5.25), this equation can be made more transparent under the approximation of $L_1 = L_0$, reducing to

$$
\begin{aligned}
&-\frac{1}{2}(1-2c_1)\Big[\{[c(I-S)^1-h^T(I-S)^3]\cdot\varepsilon^{ds}+[c(I-S)^2-h^T(I-S)^4]\cdot D^{ds}\}\cdot\varepsilon^{ds}\\
&+\{[-h(I-S)^1+\beta(I-S)^3]\cdot\varepsilon^{ds}+[-h(I-S)^2+\beta(I-S)^4]\cdot D^{ds}\}\cdot D^{ds}\Big]+\bar{\sigma}\varepsilon^{ds}+\bar{E}D^{ds}\\
&=\gamma_s(A_1/V_1)+\frac{b_1}{a_1+c_1},\left(or,\gamma_s(A_1/V_1)-\frac{b_2}{a_2-c_1}\right)
\end{aligned}
\tag{6.12}
$$

This equation provides the new domain concentration c_1 at a given level of applied $(\bar{\sigma},\bar{E})$. It is the general kinetic equation of domain switch.

At this level of c_1, the overall strain $\bar{\varepsilon}$ and overall electric displacement $\bar{D}$ of the ferroelectric ceramic follow as

$$\bar{\varepsilon}=s\sigma+d^T\mathrm{E}+\mathrm{c}_1(\varepsilon^{\mathrm{ds}}+\varepsilon^*)\tag{6.13}$$

$$\bar{D}=d\sigma+k\mathrm{E}+\mathrm{c}_1(\mathrm{D}^{\mathrm{ds}}+D^*)\tag{6.14}$$

where the elastic, piezoelectric and dielectric compliances are those of the parent domain. This pair of overall relations are not limited to the condition that $L_1 = L_0$, but when such an assumption is made both equivalent eigen fields ε^* and D^* vanish.

Under a cyclic electrical loading a readily measurable quantity is the level of applied electric field at which nonlinearity starts ($c_1 = 0$). In the absence of an external stress the surface energy term $\gamma_s A_1/V_1$ can be related to as

$$
\begin{aligned}
&-\frac{1}{2}\Big[\{[c(I-S)^1-h^T(I-S)^3]\cdot\varepsilon^{ds}+[c(I-S)^2-h^T(I-S)^4]\cdot D^{ds}\}\cdot\varepsilon^{ds}\\
&+\{[-h(I-S)^1+\beta(I-S)^3]\cdot\varepsilon^{ds}+[-h(I-S)^2+\beta(I-S)^4]\cdot D^{ds}\}\cdot D^{ds}\Big]+\bar{E}_sD^{ds}\\
&=\gamma_s(A_1/V_1)+\frac{b_1}{a_1},\left(or,\gamma_s(A_1/V_1)-\frac{b_2}{a_2}\right)
\end{aligned}
\tag{6.15}
$$

Subtraction of Equation (6.15) from Equation (6.12) leads to the new form of kinetic equation

$$(\overline{E}-\overline{E}_s)D^{ds} = -c_1\Big[\{[c(I-S)^1 - h^T(I-S)^3]\cdot\varepsilon^{ds} + [c(I-S)^2 - h^T(I-S)^4]\cdot D^{ds}\}\cdot\varepsilon^{ds}$$

$$+\{[-h(I-S)^1+\beta(I-S)^3]\cdot\varepsilon^{ds} + [-h(I-S)^2+\beta(I-S)^4]\cdot D^{ds}\}\cdot D^{ds}\Big] + \frac{b_1}{a_1+c_1} - \frac{b_1}{a_1},$$

$$\left(or, -\frac{b_2}{a_2-c_1}+\frac{b_2}{a_2}\right)$$

(6.16)

This gives the specific value of new domain concentration c_1 at the level of electric field. We have to be careful about using (6.16) because there are two sets of D^{ds} and ε^{ds} for the 1st and 2nd 90° domain switches. Take $BaTiO_3$ as an example (Fig. 6.1), under electric field with downward direction, for the 1st 90° switch,

$$D_1^{ds} = (P_s, 0, -P_s),\ \ \varepsilon_1^{ds} = [(c-a)/a, 0, -(c-a)/c, 0, 0, 0] \qquad (6.17)$$

For the 2nd 90° switch, these values become,

$$D_2^{ds} = (-P_s, 0, -P_s),\ \ \varepsilon_2^{ds} = [-(c-a)/c, 0, (c-a)/a, 0, 0, 0] \qquad (6.18)$$

So, we have to use (6.16) twice to calculate c_1 separately for the 1st and 2nd 90° domain switches.

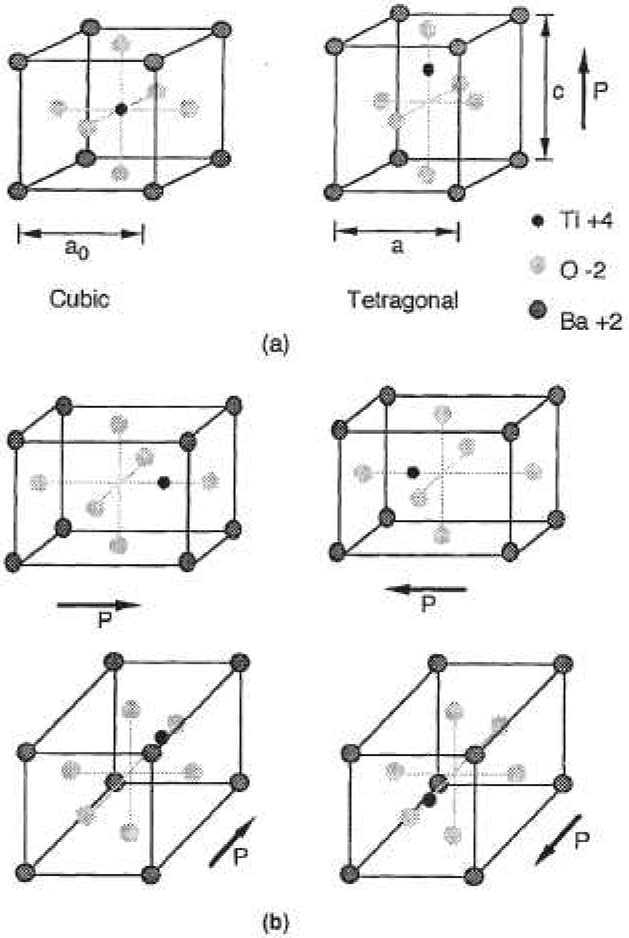

Fig. 6.1 (a) Spontaneous polarization of $BaTiO_3$, (b) Reorientation of the domain under compressive stress or perpendicular electric field.

Now let the applied electric field be opposite to the poled direction. With the calculated c_1 the electric displacement follows as

$$\overline{D}_3 = k_{33}\overline{E}_3 + c_1(D_3^{ds} + D_3^{*}) \tag{6.19}$$

The result is shown in Figure 6.2. The theory as a whole is found to be able to capture the essential features of the hysteresis behavior.

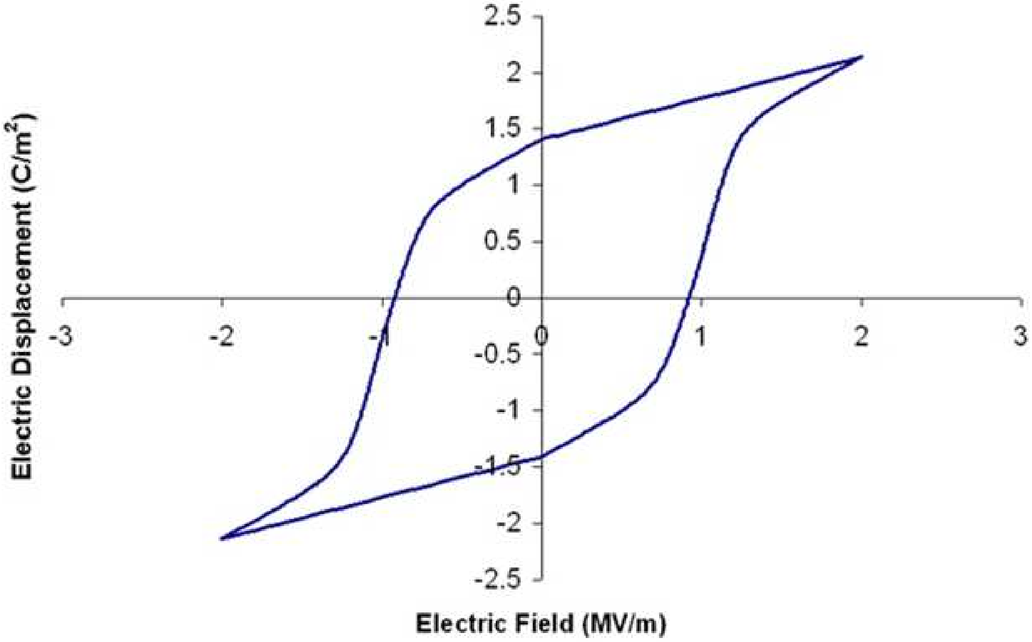

Fig. 6.2 Electric displacement versus electric field hysteresis loop for PZT fibers

It is interesting to see how the new domain evolves during this cyclic electrical loading. This is plotted in Fig. 6.3. Starting from positive electric field of about 2 MV/m, the initial unloading is strictly linear without generation of any new domain. As it reduced to zero, new domains began to evolve. The evolution was initially slow, and became very fast as it reduced to the coercive field of about –1 MV/m, and then became slow again as it approached completion of switch due to an increased level of domain interactions. Reversed switch from negative electric field did not commence until the electric field increased to zero. Then following the same pattern the right branch of the loop was completed.

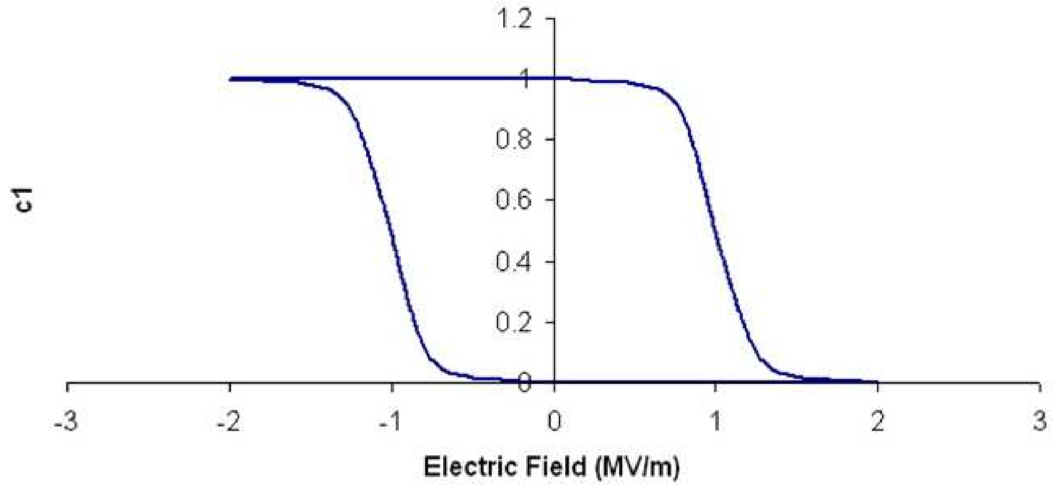

Fig. 6.3 Evolution of the new switched domain concentration c_1 under electric loading

The hysteresis D versus E relation discussed above is accompanied by an evolution of axial strain. At a given c_1 the axial strain component of the heterogeneous material is given by

$$\bar{\varepsilon}_{33} = d_{333}\bar{E}_3 + c_1(\varepsilon_{33}^{ds} + \varepsilon_{33}^{*}) \qquad (6.20)$$

so that, in addition to the linear portion due to the converse effect, there is an additional one due to the continuous evolution of new domain.

The narrow tails of the butterfly shaped loop is a reflection that the 180° domain switch is not accomplished instantly; as such a switch does not produce any eigen strain. Rather, it is a reflection that the 180°-switch is accomplished first by a 90°-switch and then followed by another consecutive 90°-switch.

This is tantamount to saying that the positively charged Ti ion (say in the $BaTiO_3$ unit cell) moves to the side first (to produce a 90° switch) before it reaches its final destination to complete the 180° switch. The first part results in a reduction of the strain and the subsequent one leads to an increase. The two consecutive motions take place as the applied electric field reaches the neighborhood of the coercive field where the curve is very steep and the switch process is believed to be non-stopping but the strain reduction and increase are nonetheless detectable. Accounting for the existence of such an intermediate state is an essential step to a successful modeling of the sharp tails, and it is also consistent with the notion that a 90°-switch is much easier to accomplish than a direct 180°-switch. The developed model is applied in this two-step fashion to calculate the evolution of the axial strain. As the 90°-switch is only half way to a full 180°-switch, a given value of c_1 in Fig. 6.3 is taken to generate two c_1 for the volume concentration of the 90° domain in the calculation of axial strain in Equation (6.17). This is done for each of the two steps, noting that for the second step the recount starts from $c_1 = 0.5$. The calculated results for the PZT are shown in Fig. 6.4, along with the experimental data from Zhao's Dissertation [22] (Table 6.1). The full range of the strain versus electric field relation—including the sharp tails of the butterfly and the remanent strain—is seen to be well simulated.

Table 6.1. Materials properties and constants

Properties	**Matrix**	**PZT Fiber**
$s_{11}(10^{-11} m^2/N)$	19.7	2.07
$s_{12}(10^{-11} m^2/N)$	-5.91	-0.621
$s_{13}(10^{-11} m^2/N)$	-5.91	-0.621
$s_{33}(10^{-11} m^2/N)$	19.7	2.07
$s_{44}(10^{-11} m^2/N)$	51.2	5.38
$s_{66}(10^{-11} m^2/N)$	51.2	5.38
k_{11} (k_0=8.85×$10^{-12}$$C^2/Nm^2$)		1850×k_0
k_{33}		1850×k_0
$d_{31}(10^{-10} C/N)$		-1.85
$d_{33}(10^{-10} C/N)$		4.40
$d_{15}(10^{-10} C/N)$		4.55

PZT fiber percentage c_f=65%.

$[\varepsilon^{ds}]_1 = [0.001665, 0, -0.001665, 0, 0, 0]$, $[D^{ds}]_1 = [0.16, 0, -0.16]$

$[\varepsilon^{ds}]_2 = [-0.001665, 0, 0.001665, 0, 0, 0]$, $[D^{ds}]_2 = [-0.16, 0, -0.16]$

a_1=0.01, b_1=8114.5258 J/m^3,

a_2=0.51, b_2=7654.4726 J/m^3.

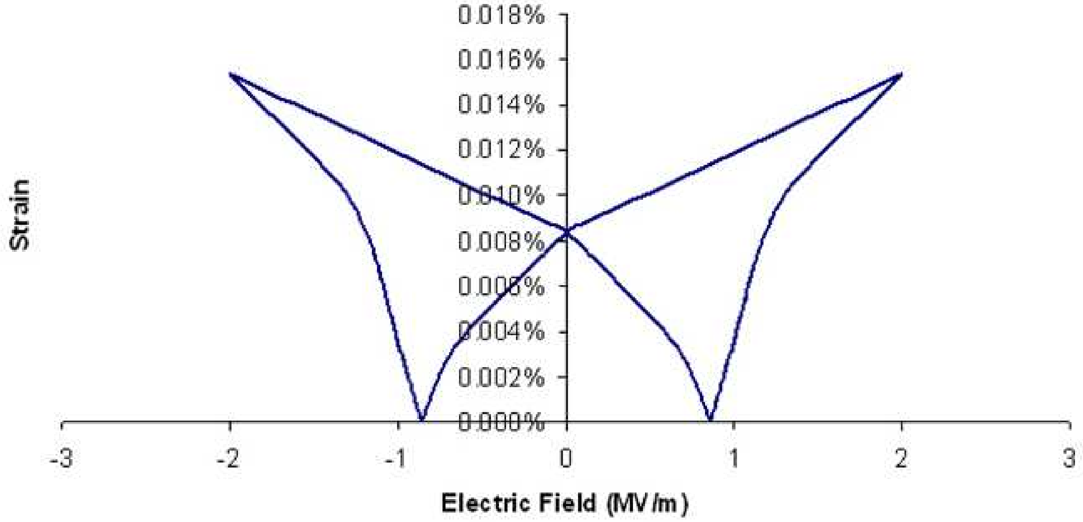

Fig. 6.4 Evolution of PZT fibers strain under electric loading

6.2 1-3 Piezoelectric Fiber Composites

Now we have the strain and electric displacement results for PZT fibers inside the composites regarding to the applied external electric field. Then how can we use these results to get the overall strain and electric displacement reaction for the composite material due to the presence of external electric field? At this second level, again a micromechanics approach for two-phase composite with the piezoelectric inclusions is adopted here. For piezoelectric composites, due to electromechanical coupling, the piezoelectric S-tensor, in general, cannot be obtained explicitly. Only for some special cases such as lamellar [49] and fiber [75], the explicit solution exists. Here we adopt the results from [75]. The direct results they derived are for coefficients (c, e, k). To use their results, we have to do coefficients conversion between (c, e, k) and (s, d, k). The complete conversion formulas are listed in Appendix B. Once coefficients (c, e, k) for both PZT fiber and matrix are calculated, the formulas from [75] then can be used to calculate overall coefficients (c, e, k) for the composites where superscript f represents fiber and superscript m represents matrix. c_f is effective PZT fiber percentage. Then the conversion formulas can be used one more time to transform coefficients (c, e, k) back to (s, d, k).

There is one more issue we have to resolve before using the composite coefficients formulas directly. One of the assumptions they used when they derived the formulas is that all the coefficients for both the fibers and matrix are constants. That means the relationship between loading and response is linear. This is true for composites under small loading conditions, but not for piezoelectric composites under large loading conditions. Under higher loading such as high electric field loading, the piezoelectric fiber alone responds non-linearly, like the hysteresis loop for electric displacement and the butterfly curve for strain derived above using micromechanics. To be able to study the nonlinear behavior of the system, a secant modulus approach associated with the micromechanics theory is adopted here. The concept of secant modulus is that we break the whole non-linear curve down into many tiny little segments, the coefficients at each segment can be treated as constants as long as the segment is small enough. Also, there are only two coefficients that play major roles in the whole calculation which are d_{33} and k_{33}. So we only need to get $d_{33}^{(s)}$ and $k_{33}^{(s)}$ for each small segment and keep other coefficients unchanged. Here (s) stands for secant. These two secant coefficients are calculated from (6.16) and (6.17) as following,

$$\overline{D}_3 = k_{33}\overline{E}_3 + c_1(D_3^{ds} + D_3^*) = k_{33}^{(s)}\overline{E}_3 \tag{6.21}$$

$$\overline{\varepsilon}_{33} = d_{333}\overline{E}_3 + c_1(\varepsilon_{33}^{ds} + \varepsilon_{33}^*) = d_{333}^{(s)}\overline{E}_3 \tag{6.22}$$

Since our goal is to produce relationships of electric displacement and strain versus electric loading for the composites, the over all composite coefficients d_{33} and k_{33} are the only two coefficients we need. Therefore, we only need formulas for some coefficients from [75], the following is the list of these formulas.

$$C_{11} = \frac{C_{11}^f C_{11}^m}{c_f C_{11}^m + (1-c_f)C_{11}^f} \tag{6.23}$$

$$C_{12} = C_{11}\left[\frac{c_f C_{12}^f}{C_{11}^f} + \frac{(1-c_f)C_{12}^m}{C_{11}^m}\right] \tag{6.24}$$

$$C_{13} = C_{11}\left[\frac{c_f C_{13}^f}{C_{11}^f} + \frac{(1-c_f)C_{13}^m}{C_{11}^m}\right] \tag{6.25}$$

$$e_{31} = C_{11}\left[\frac{c_f e_{31}^f}{C_{11}^f} + \frac{(1-c_f)e_{31}^m}{C_{11}^m}\right] \tag{6.26}$$

$$e_{33} = c_f e_{33}^f + (1-c_f)e_{33}^m + \frac{C_{13}e_{31}}{C_{11}} - \frac{c_f C_{13}^f e_{31}^f}{C_{11}^f} - \frac{(1-c_f)C_{13}^m e_{31}^m}{C_{11}^m} \tag{6.27}$$

$$k_{33} = c_f k_{33}^f + (1-c_f)k_{33}^m + \frac{e_{31}^2}{C_{11}} - \frac{c_f (e_{31}^f)^2}{C_{11}^f} - \frac{(1-c_f)(e_{31}^m)^2}{C_{11}^m} \tag{6.28}$$

The practical procedure has four steps:

(1) Get $d_{33}^{(s)}$ and $k_{33}^{(s)}$ for each segment (small increment in E) along with S_{11}, S_{12}, S_{13}, S_{33} and d_{31} as initial input for piezoelectric fiber and get the corresponding coefficients for matrix too;

(2) Get C_{11}, C_{12}, C_{13}, e_{31}, e_{33} and k_{33} for both piezoelectric fiber and matrix using conversion method in Appendix B;

(3) Calculate composite coefficients C_{11}, C_{12}, C_{13}, e_{31}, e_{33} and k_{33} using above (6.23-6.28);

(4) Convert these coefficients to (s, d, k) to get d_{33} and k_{33} for composites.

Up to now, we haven't considered angle effect yet. The results we get from above procedure are for $\theta = 0^o$ only. Fig. 6.5 is the comparison between the developed model and the experimental data for the relationship between strain and electric field for zero degree PZT fiber composite; Fig. 6.6 is the comparison between the model and experimental data for electric displacement and electric field of PZT fiber composite with zero degree orientation. The solid lines are from theoretical modeling and the red dashed lines are from the experiments [22].

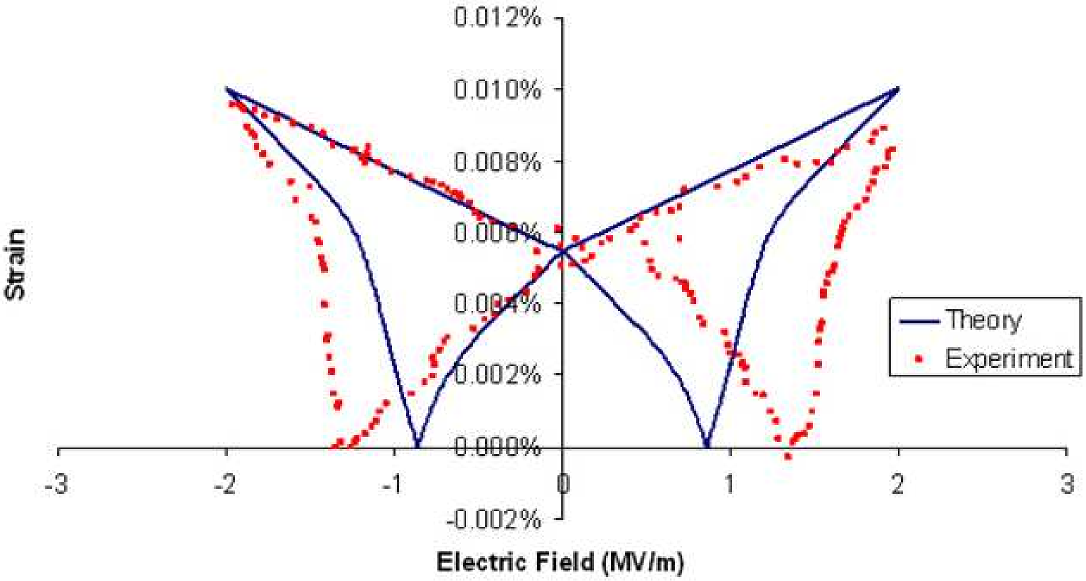

Fig. 6.5 Overall strain and electric field relation for zero degree PZT composite under electric loading

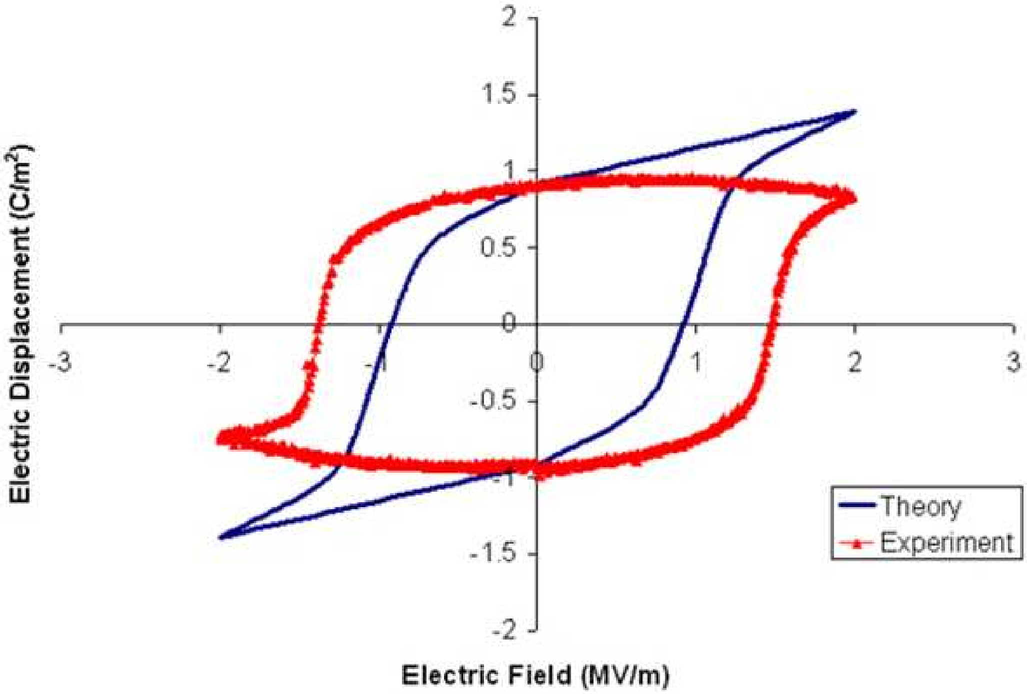

Fig. 6.6 Overall electric displacement for zero degree PZT composite under electric loading

6.3 Orientation Effects on 1-3 Piezoelectric Fiber composites

Orientation effects on PZT fiber composites have two parts. One is due to orientation change which can be derived from the transformation of coordinates; the other is the change of effective PZT fiber percentage due to the sample size limit. We will discuss them one by one in the following.

For the orientation effect, both ε^{ds} and D^{ds} are changing in terms of angles. In order to simplify the orientation problem and still capture the key factor of the electromechanical coupling behavior of a ferroelectric polycrystal, an equivalent two-phase system has been introduced by Li [49]. In this equivalent system, the overall effective polarization of the parent phase is treated as an original phase 0, and the new switched domain as phase 1. Then the two-phase composite micromechanics model can be readily applied. In such a system, the effective electric polarization due to the domain switch in the global coordinates can be written as

$$D_{ds} = \begin{bmatrix} (1-\sin\theta) \\ 0 \\ \cos\theta \end{bmatrix} P_s \tag{6.29}$$

where P_s is the spontaneous polarization. The corresponding polarization strain (or eigenstrain) is

$$\varepsilon_{ds} = \begin{bmatrix} (1+\upsilon_t)\varepsilon_{33}^s \cos^2\theta & 0 & (1+\upsilon_t)\varepsilon_{33}^s \cos\theta\sin\theta \\ 0 & 0 & 0 \\ (1+\upsilon_t)\varepsilon_{33}^s \cos\theta\sin\theta & 0 & -(1+\upsilon_t)\varepsilon_{33}^s \cos^2\theta \end{bmatrix} \tag{6.30}$$

where ε_{33}^s is the polarization strain due to the spontaneous polarization in the local coordinates.

ν_t is the "transformation" Poisson's ratio during the poling process.

When a fully poled specimen is subjected to compressive loading with an angle of θ to the poling direction, the change of remanent polarization or the maximum depolarization ΔP in loading direction (axis 3) can be directly obtained as

$$\Delta P = P_s \cos\theta \tag{6.31}$$

where the spontaneous polarization P_s is set to be the same as the saturation polarization P_{sat}.

For the second issue which is effective PZT fiber percentage change due to change of angles, we use Fig. 6.7 to illustrate the sample size limit and calculate the corresponding effective PZT density.

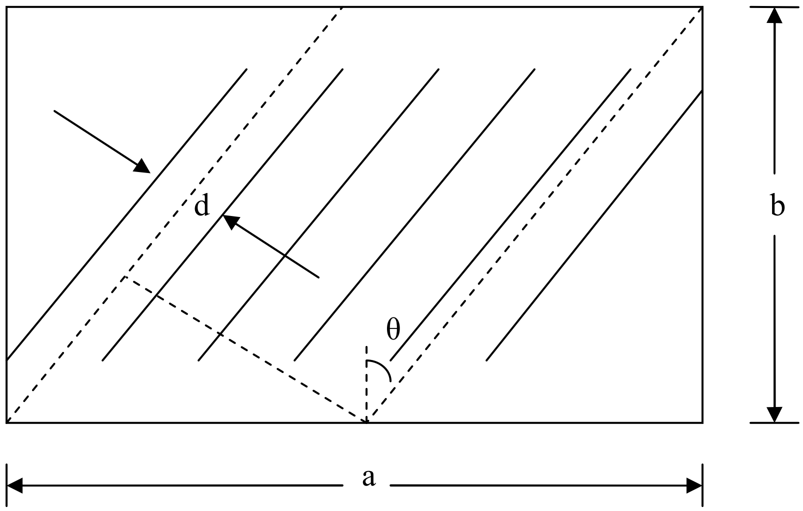

Fig. 6.7 Illustration of angle effects on effective PZT percentage c_f

As showed in Fig. 6.7, only those PZT fibers which are within the region in the middle can contribute to the overall electric displacement response due to the external electric field; other PZT fibers cannot contribute at all because there is no circuit constructed along the fibers. The effective PZT Fiber Density c_f can be calculated as,

$$\frac{(a-b\cdot\tan\theta)\cdot\cos\theta}{d}=\frac{(a\cdot\cos\theta-b\cdot\sin\theta)}{d}=\frac{R}{d}\cdot\sin(\alpha-\theta) \tag{6.32}$$

$$R=\sqrt{a^2+b^2},\quad \alpha=\arctan(a/b),\quad \theta\le\alpha \tag{6.33}$$

For 0 degree case, the effective PZT density c_f is just the fiber percentage within the composite which is 65%; for other angles, the effective PZT density c_f is following sin function in terms of angles. (See Fig. 6.8)

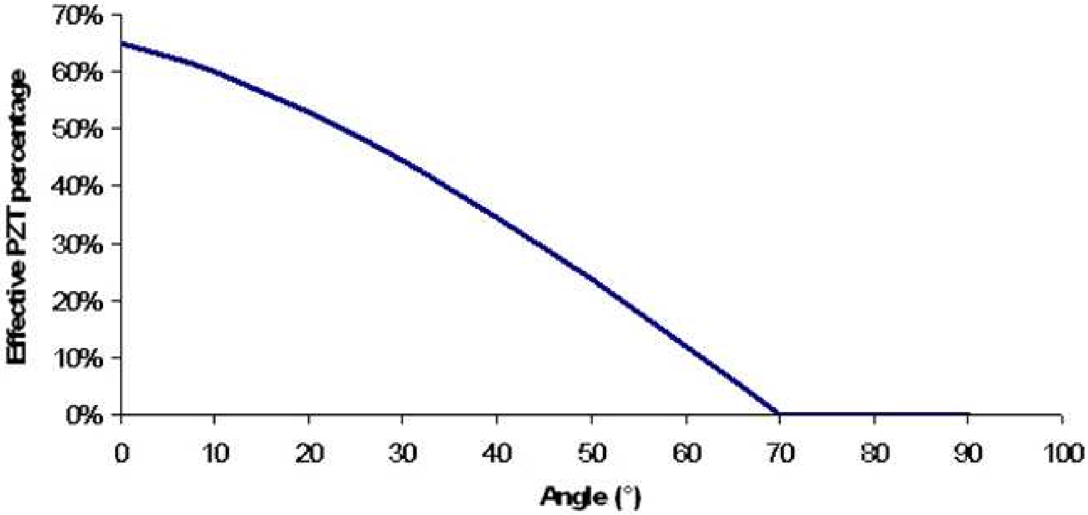

Fig. 6.8 Change of the effective PZT percentage c_f in term of angle θ

Now we combine the angle effects on both orientation and effective PZT percentage to calculate the evolution of hysteresis loop and butterfly curve due to angle changes. After put the new ε^{ds}, D^{ds} and c_f into the calculation above for the zero degree angle, we are able to produce relationships of electric displacement and strain versus electric loading for all the angles other than zero. Fig. 6.9 shows the theoretical calculation results for evolution of hysteresis loops with different angles. It is then compared with Fig. 6.10 which is from the experimental data; Fig. 6.11 shows the theoretical calculation results for evolution of butterfly strain curves with different angles and then it is compared with the experimental data (Fig. 6.12). Meanwhile, the remanent polarization and remanent strain have also been calculated and compared with the experimental results. These are showed as Fig. 6.13 and Fig. 6.14.

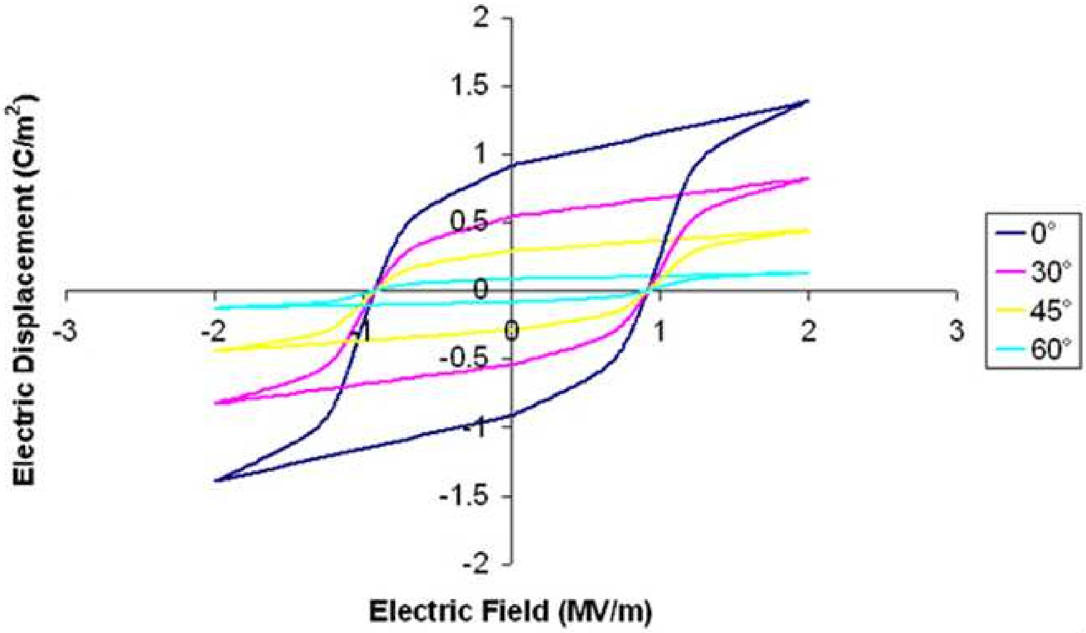

Fig 6.9 Theoretical results for the hysteresis loops of electric displacement and electric field at θ=0°, 30°, 45°, 60°

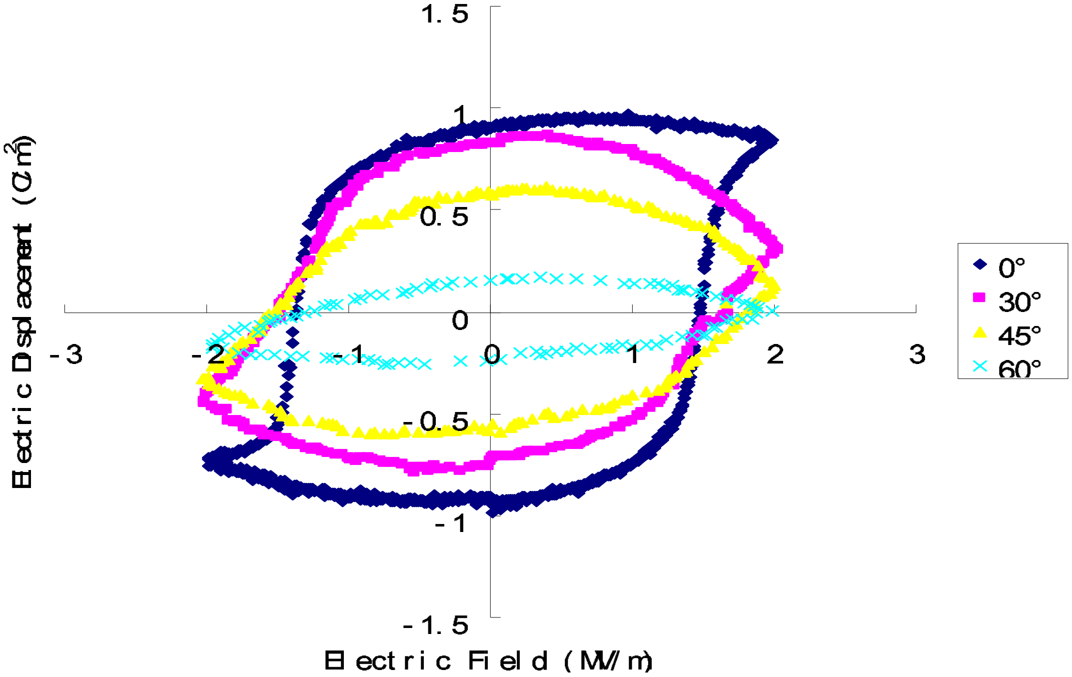

Fig 6.10 Experimental results for the hysteresis loops of electric displacement and electric field at θ=0°, 30°, 45°, 60° [22]

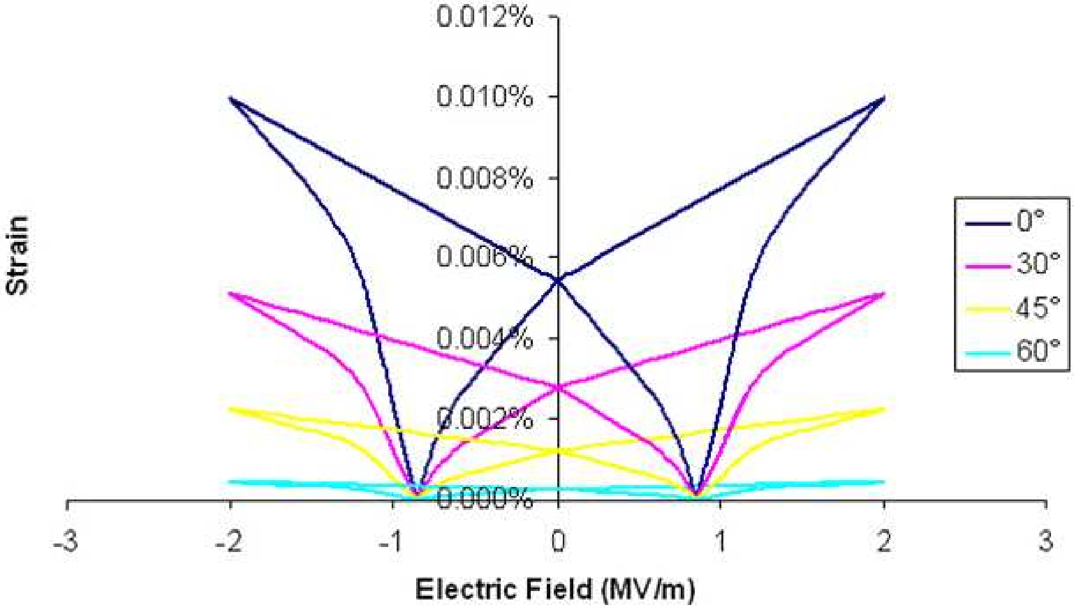

Fig 6.11 Theoretical results for the relation of electric field and strain at $\theta = 0°, 30°, 45°, 60°$

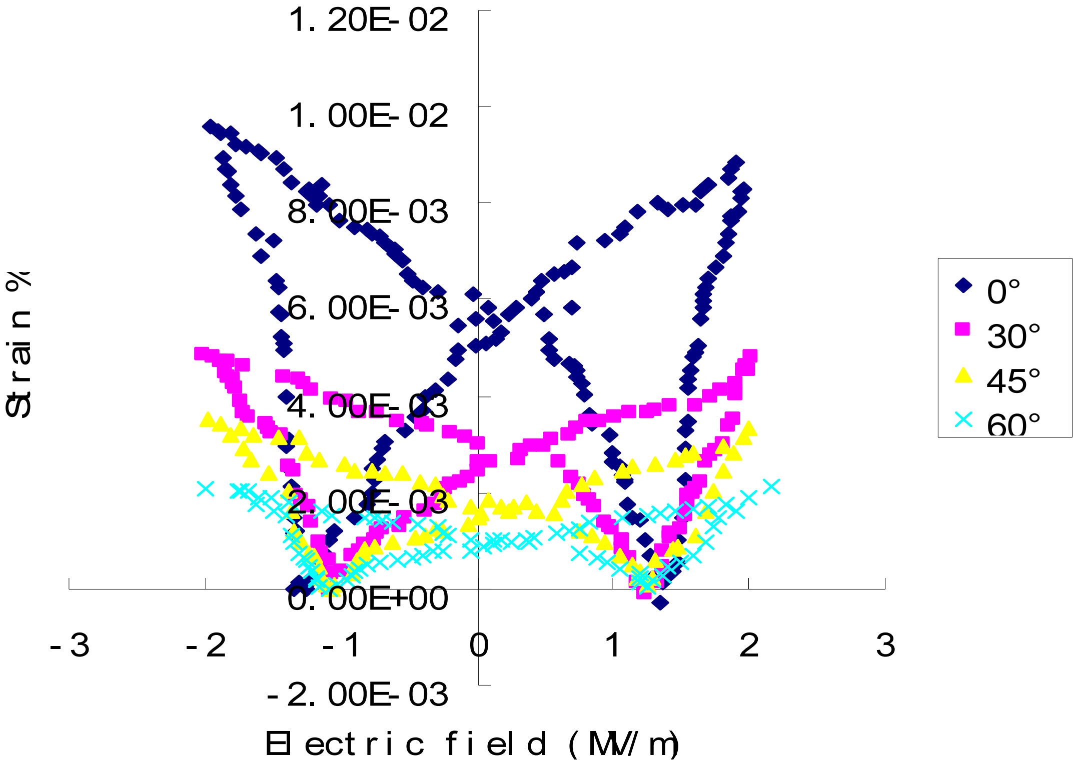

Fig 6.12 Experimental results for the relation of electric field and strain at $\theta = 0°, 30°, 45°, 60°$ [22]

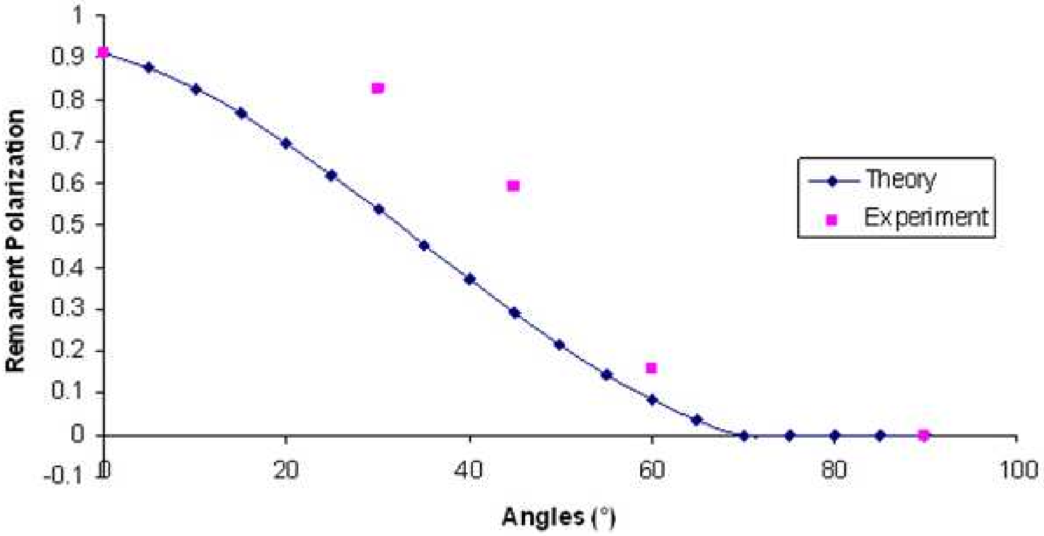

Fig. 6.13 Comparison of the remanent polarization in term of angle θ

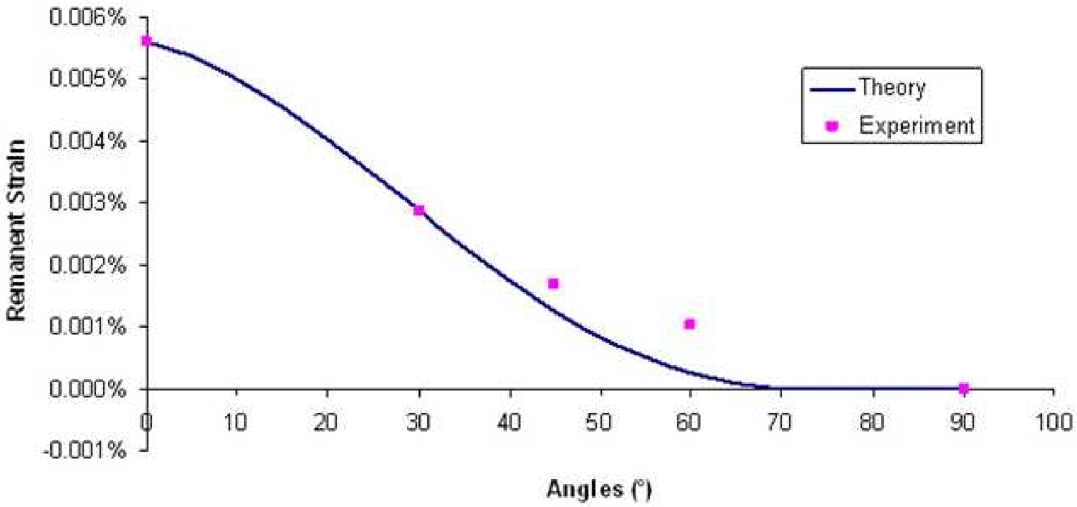

Fig. 6.14 Comparison of the remanent strain in term of angle θ

6.4 Conclusions

A two-level micromechanics based model is established to study the hysteresis loop and butterfly strain curve of piezoelectric composites. At the first level (the piezoelectric fibers), a micromechanics based on an irreversible thermodynamic principle developed in

Chapter 5 has been extended to study the hysteresis behavior of piezoelectric fibers. Then, at the second composite level, a secant modulus approach with traditional micromechanics model of piezoelectric composite has been developed. Finally the angle effects of applied electric field have been modeled. All the theoretical results have been compared with experimental data.

7. Combination of Micromechanics Model and Texture Model

In Chapter 4, we presented a texture model to study ferroelectrics in different orientations. The model needs two critical inputs. One is the orientation distribution of the material and the other is the single grain behavior under external forces. For the second assumption, we used a simple math function in our previous work. In Chapter 5 and Chapter 6, we presented a theoretical approach on $BaTiO_3$ single crystal and PZT composite studies. This micromechanics-based model could be the second assumption for our first model. In this chapter, a universal model is constructed by combining Texture and Anisotropy approach and the Micromechanics approach.

Using the same method in Chapter 6, we can get relationship of electric displacement and external electric field for a single crystal. This relationship can be used as one of the initial assumptions for Texture and Anisotropy model. Fig. 7.1 shows this relationship calculated from micromechanics model. Fig. 7.2 is the result for piezoelectric single crystal with orientation [0 0 1] under electric loading with different angles.

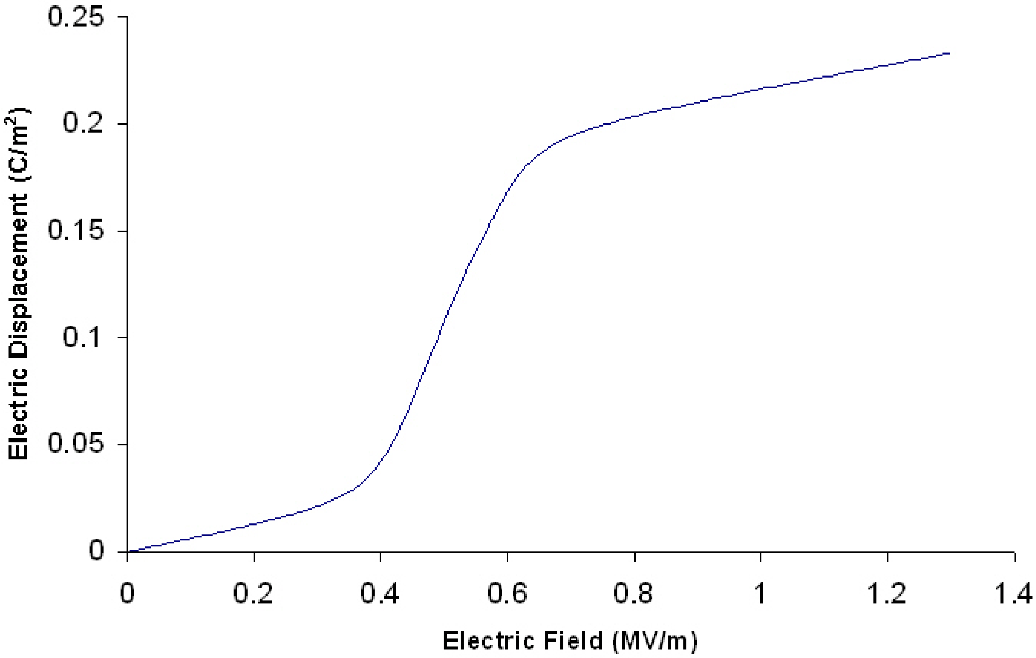

Fig. 7.1 Relationship of electric displacement and electric field got from micromechanics model

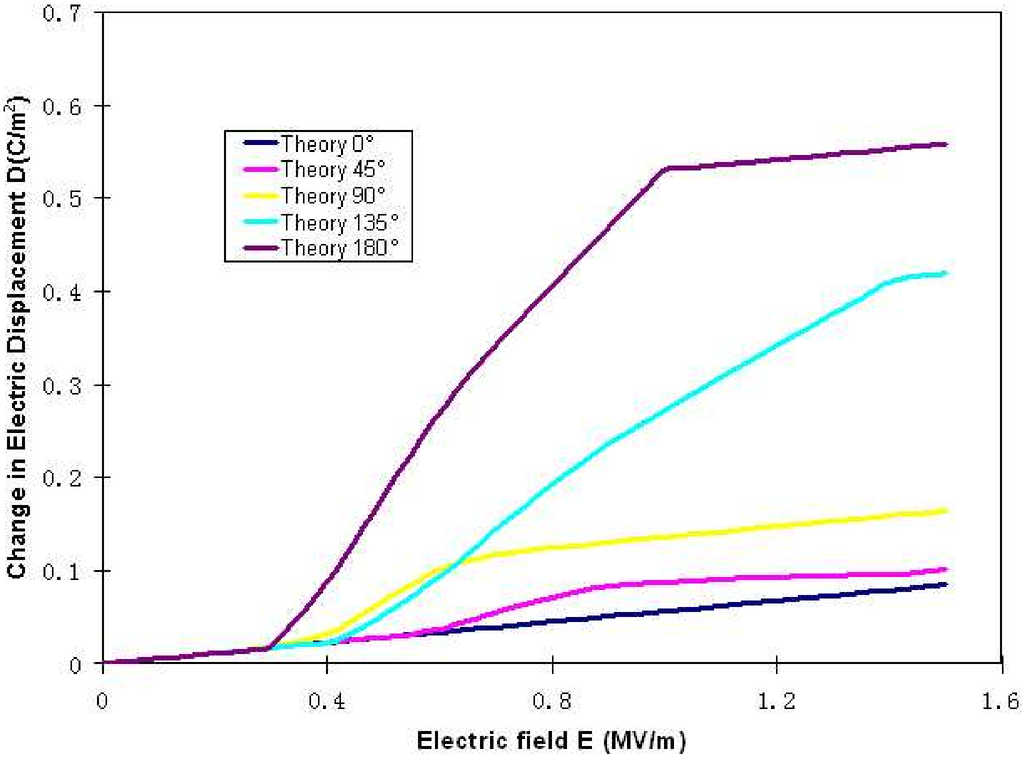

Fig. 7.2 Single crystal [001] results under different loading angles

From the comparison of the theoretical results (Fig. 7.2) and the experimental data (Fig. 4.9), again like results in Chapter 4, 0°, 90° and 180° curves fit well; 45° curve also fits. However, 135° curve does not fit experimental data. The reasons are the same as listed in Chapter 4. It comes from initial assumptions. We assume it is single crystal and all the grains can only have either 90° or 180° domain switch or does not switch at all. 45° and 135° forces have the least components on both 90° and 180° directions. The criterion for domains to switch is the component force on desirable direction reaches a certain level. So in 45° or 135° cases, in order to get domain switch, a greater external force is needed comparing to other cases. The discrepancy may also come from the limitation of the texture model which did not take into account of interaction between each domain.

8. Ginzburg–Landau Theory Approach

When we use micromechanics model to study $BaTiO_3$ nanowires problem, we reached size limit of this model. From our model, the smallest diameter for $BaTiO_3$ nanowire to have ferroelectric behavior is around 50nm. Comparing to available experimental data, it is way too high. This is due to general assumption for S tensor which is derived from bulk material or 2-dimentional semi infinite plane. It is not suitable for nanowire since the diameter is within nano range and the material structure becomes one-dimensional.

8.1 Landau governing equation

Usually at this range, quantum mechanics has to be used to give material appropriate model such as first principle and ab-initio methods. However, these methods are limited in very small range of size up to hundreds atoms. Here we choose Landau theory to study the electro-mechanical coupling behavior of ferroelectric nanowires.

Let us consider ferroelectric cylindrical nanowire with radius R, length h and polarization $P_Z(\rho, z)$ oriented along z-axis (Fig.8.1). The external electric field is E(0, 0, E_0).

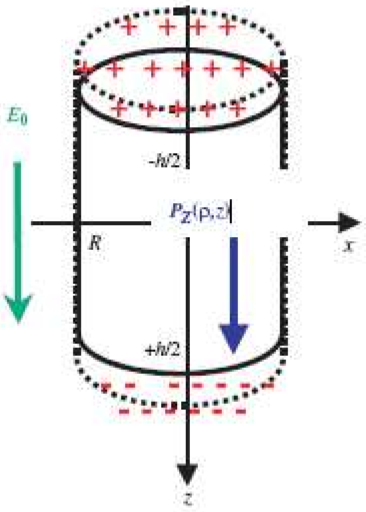

Fig. 8.1 The geometry of cylindrical particle.[8]

The bulk part ΔGv acquires the form:

$$\Delta Gv = 2\pi\int_{-h/2}^{h/2} dz\int_0^R \rho d\rho \times \left(\frac{\alpha_R(T)}{2}P_Z^2(\rho,z)+\frac{\beta_Z}{4}P_Z^4(\rho,z)+\frac{\gamma_Z}{6}P_Z^6(\rho,z)+\frac{\delta}{2}(\nabla P_Z(\rho,z))^2-P_Z(\rho,z)\left(E_0+\frac{E_Z^d(\rho,z)}{2}\right)\right)$$

(8.1)

Following Euler-Lagrange equations, we have:

$$\alpha_R P_Z(\rho,z)+\beta P_Z^3(\rho,z)+\gamma P_Z^5(\rho,z)-\delta\nabla^2 P = E_0 + E_Z^d(\rho,z) \qquad (8.2)$$

Where,

$$\nabla^2 P = \frac{\partial^2 P_Z(\rho,z)}{\partial z^2}+\frac{1}{\rho}\frac{\partial}{\partial\rho}\rho\frac{\partial}{\partial\rho}P_Z(\rho,z) = \frac{\partial^2 P_Z(\rho,z)}{\partial z^2}+\frac{1}{\rho}\frac{\partial}{\partial\rho}P_Z(\rho,z)+\frac{\partial^2 P_Z(\rho,z)}{\partial\rho^2}$$

(8.3)

Material coefficients $\delta > 0$, $\gamma_Z > 0$, while $\beta_Z < 0$ for the first order phase transitions or $\beta_Z > 0$ for the second order ones. The coefficient $\alpha_R(T)$ in Eq. (8.1) & (8.2) should be renormalized by the external stress [76, 77].

$$\alpha_R(T,R) = \alpha_T(T-T_C)+2Q_{12}\frac{\mu}{R} \qquad (8.4)$$

The expression for depolarization field E_Z^d(r, z) inside the cylindrical nanowire covered with screening charges is derived elsewhere [77].

$$E_Z^d(\rho,z) =< P_Z > \eta(R,h) - \eta(R,h)P_Z(\rho,z)\text{, where } \eta(R,h) = \frac{4\pi}{1+(h/2R)^2} \qquad (8.5)$$

Ignore non-linear terms, move the P_z term inside the E_z^d to the left, Eq. (8.2) becomes:

$$(\alpha_R + \eta(R,h))P_Z(\rho,z) - \delta\nabla^2 P = E_0 + < P_Z > \eta(R,h) \qquad (8.6)$$

Here we got Landau governing equation for $BaTiO_3$ nanowires.

8.2 Homogeneous solutions

To solve Eq. (8.6), we need to find both homogeneous and particular solutions. Let's get homogeneous solution first, which is to solve:

$$(\alpha_R + \eta)P_Z(\rho,z) - \delta\left(\frac{\partial^2 P_Z(\rho,z)}{\partial z^2} + \frac{1}{\rho}\frac{\partial}{\partial\rho}P_Z(\rho,z) + \frac{\partial^2 P_Z(\rho,z)}{\partial\rho^2}\right) = 0 \qquad (8.7)$$

Using separate variables,

Let $P_Z(\rho,z) = T(\rho)\times Q(z)$, Eq. (8.7) becomes:

$$(\alpha_R + \eta)TQ - \delta\left(TQ'' + \frac{1}{\rho}T'Q + T''Q\right) = 0 \qquad (8.8)$$

Divided by TQ, we have:

$$(\alpha_R + \eta) - \delta\left(\frac{Q''}{Q} + \frac{1}{\rho}\frac{T'}{T} + \frac{T''}{T}\right) = 0 \qquad (8.9)$$

Let $$\alpha_R + \eta - \delta\frac{Q''}{Q} = \delta\left(\frac{1}{\rho}\frac{T'}{T} + \frac{T''}{T}\right) = m \qquad (8.10)$$

We get two separate equations.

$\frac{T''}{T}+\frac{1}{\rho}\frac{T'}{T}=\frac{m}{\delta}$ (8.11) for variable T, and $Q''-\frac{\alpha+\eta-m}{\delta}Q=0$ (8.12) for variable Q.

Eq. (8.11) has following solutions:

(i) if m=0, $\frac{d}{d\rho}\left(\rho\frac{dT}{d\rho}\right)=0$, then $T=c_1\ln\rho+c_2$ (8.13)

(ii) if $\frac{m}{\delta}<0$, let $\frac{m}{\delta}=-\frac{n^2}{R^2}$, then $T''+\frac{1}{\rho}T'+\frac{n^2}{R^2}T=0$, solution for T is:

$$T=A_1J_0(\frac{n\rho}{R})+A_2Y_0(\frac{n\rho}{R}), \tag{8.14}$$

where J_0 and Y_0 are related to Bessel functions

(iii) if $\frac{m}{\delta}>0$, let $\frac{m}{\delta}=\frac{n^2}{R^2}$, then $T''+\frac{1}{\rho}T'-\frac{n^2}{R^2}T=0$, solution for T will be

$$T=A_3I_0(\frac{n\rho}{R})+A_4K_0(\frac{n\rho}{R}), \tag{8.15}$$

where I_0 and K_0 are related to Complex Bessel functions.

For our calculation, we use even simpler solution $T=A_1J_0(\frac{n\rho}{R})$ as the homogeneous solution for T. (8.16)

For Eq. (8.12), let $Q=e^{\frac{k}{h}Z}$ (8.17)

Then it becomes:

$$\delta\frac{k^2}{h^2}e^{kZ/h}-(\alpha+\eta-m)e^{kZ/h}=0,\ \frac{k^2}{h^2}=\frac{\alpha+\eta-m}{\delta},\ k=h\sqrt{\frac{\alpha+\eta-m}{\delta}} \tag{8.18}$$

The solution for Q is:

$$Q=B_1\exp(kZ/h)+B_2\exp(-kZ/h) \tag{8.19}$$

Together, the homogeneous solution for Pz will be $P_Z=T\times Q$. (8.20)

8.3 Particular solutions

To get particular solutions for Eq. (8.6), which is the same as:

$$(\alpha_R+\eta)P_Z(\rho,z)-\delta\left(\frac{\partial^2 P_Z(\rho,z)}{\partial z^2}+\frac{1}{\rho}\frac{\partial}{\partial\rho}P_Z(\rho,z)+\frac{\partial^2 P_Z(\rho,z)}{\partial\rho^2}\right)$$
$$=E_0+<P_Z>\eta \tag{8.21}$$

We assume the particular solution $P_Z = T\times W$ satisfies Eq. (8.21), where W is a constant, then we have the following,

$$(\alpha_R+\eta)TW-\delta\left(\frac{1}{\rho}T'+T''\right)W=E_0+<P_Z>\eta \tag{8.22}$$

8.4 Solving Landau equation with boundary conditions

Given the homogeneous and assumed particular solutions, the constructed final solution form of P$_Z$ is:

$$P_Z=T\times(Q+W) \tag{8.23}$$

To get the exact solution P$_Z$, the boundary conditions on the cylinder faces z =±h/2, and the sidewall surface $\rho=R$ and second mode interface $\rho=r$ have been used as,

$$\left.\left(P_Z+\lambda_b\frac{dP_Z}{dz}\right)\right|_{Z=h/2}=0,\quad \left.\left(P_Z-\lambda_b\frac{dP_Z}{dz}\right)\right|_{Z=-h/2}=0, \tag{8.24}$$

$$\left.\left(P_Z+\lambda_S\frac{dP_Z}{d\rho}\right)\right|_{\rho=R}=0,\quad \left.\left(P_Z+\lambda_S\frac{dP_Z}{d\rho}\right)\right|_{\rho=r}=0 \tag{8.25}$$

Here, λ_b and λ_S are longitudinal and lateral extrapolation lengths. $\lambda_S << 1$, and the value of λ_b used in calculation is listed in table 8.1.

From (8.19), (8.20) and (8.23), we get

$$P_Z = T[(B_1 \exp(kZ/h) + B_2 \exp(-kZ/h)) + W], \qquad \text{so that,}$$

$$\frac{dP_Z}{dz} = T\frac{dQ}{dz} = T\left(B_1 \frac{k}{h} e^{kZ/h} - B_2 \frac{k}{h} e^{-kZ/h} \right) \tag{8.26}$$

Then boundary conditions (8.24) becomes

$$\left. \left(T\left((B_1 e^{kZ/h} + B_2 e^{-kZ/h}) + W \right) + \lambda_b T (B_1 \frac{k}{h} e^{kZ/h} - B_2 \frac{k}{h} e^{-kZ/h}) \right) \right|_{Z=h/2} = 0$$

$$\left. \left(T\left((B_1 e^{kZ/h} + B_2 e^{-kZ/h}) + W \right) - \lambda_b T (B_1 \frac{k}{h} e^{kZ/h} - B_2 \frac{k}{h} e^{-kZ/h}) \right) \right|_{Z=-h/2} = 0 \tag{8.27}$$

We get the solution for coefficient B_1 and B_2.

$$\begin{aligned} B_1 = B_2 &= \frac{-W}{(e^{k/2} + e^{-k/2}) + (e^{k/2} - e^{-k/2})\lambda_b k/h} \\ &= \frac{-W}{2(\cosh(k/2) + \sinh(k/2)\lambda_b k/h)} \end{aligned} \tag{8.28}$$

Solution Q becomes

$$\begin{aligned} Q &= B_1(\exp(kZ/h) + \exp(-kZ/h)) \\ &= 2B_1 \cosh(kZ/h) = \frac{-\cosh(kZ/h)\cdot W}{\cosh(k/2) + \sinh(k/2)\lambda_b k/h} \end{aligned} \tag{8.29}$$

Now we see, assumed particular solution term W is inside solution Q, then from summation of similar terms, solution Pz can be constructed as:

$$P_Z = T \times W \times (1 - \psi(z)), \quad \text{where} \quad \psi(z) = \frac{\cosh(kZ/h)}{\cosh(k/2) + \sinh(k/2)\lambda_b k/h} \tag{8.30}$$

Then we apply Pz to the other two boundary conditions (8.25), we have,

$$\left(T \times W \times (1-\psi) + \lambda_S T' \times W \times (1-\psi)\right)\Big|_{\rho=R} = 0$$

$$\left(T + \lambda_S T'\right)\Big|_{\rho=R} = \left(AJ_0(\frac{n\rho}{R}) - \lambda_S \frac{An}{R} J_1(\frac{n\rho}{R}) \right)\Bigg|_{\rho=R} = 0 \tag{8.31}$$

Which results in $J_0(n) = \frac{\lambda_S n}{R} J_1(n)$. (8.32)

Let's go back to homogeneous solution (8.16) for T.

$$T = AJ_0(\frac{n\rho}{R}) \tag{8.16}$$

Then from derivatives, we have

$$T' = -\frac{An}{R} J_1(\frac{n\rho}{R})$$

$$T'' = \frac{An}{\rho R} J_1(\frac{n\rho}{R}) - \frac{An^2}{R^2} J_0(\frac{n\rho}{R}) \tag{8.33}$$

Now Eq. (8.22) becomes

$$\left((\alpha_R + \eta) J_0(\frac{n\rho}{R}) - \delta\left(-\frac{n}{\rho R} J_1(\frac{n\rho}{R}) + \frac{n}{\rho R} J_1(\frac{n\rho}{R}) - \frac{n^2}{R^2} J_0(\frac{n\rho}{R}) \right) \right) AW = E_0 + < P_Z > \eta$$

which is

$$\left((\alpha_R + \eta + \frac{\delta n^2}{R^2}) J_0(\frac{n\rho}{R}) \right) AW = E_0 + < P_Z > \eta \ . \tag{8.34}$$

If we take average, then

$$\left((\alpha_R + \eta + \frac{\delta n^2}{R^2}) \left\langle J_0(\frac{n\rho}{R}) \right\rangle \right) AW = E_0 + < P_Z > \eta \tag{8.35}$$

To get $\left\langle J_0(\frac{n\rho}{R}) \right\rangle$, we use area weighted average as shown in Fig.8.2.

let, $r = \frac{\rho}{R}$,

$$\left\langle J_0(\frac{n\rho}{R})\right\rangle = \frac{\int_0^1 J_0(nr)\cdot(2\pi r)dr}{\pi\cdot 1^2} = 2\int_0^1 rJ_0(nr)dr = \frac{2}{n}J_1(n) \tag{8.36}$$

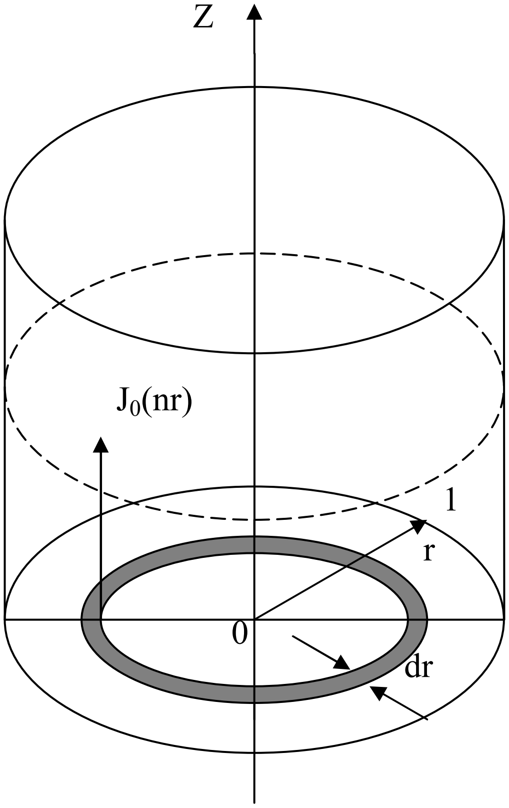

Fig. 8.2 Area-weighted average J_0

Compare (8.35) and (8.36), we get the expression for AW.

$$AW = \frac{E_0 + <P_Z>\eta}{(\alpha_R + \eta + \frac{\delta n^2}{R^2})\left(\frac{2}{n}J_1(n)\right)} \tag{8.37}$$

Finally, $P_Z = T\times W\times(1-\psi(z)) = J_0(\frac{n\rho}{R})\times AW\times(1-\psi(z))$. (8.38)

The final solution for Pz is:

$$P_Z = \frac{nJ_0(n\rho/R)}{2J_1(n)}\times\frac{E_0 + <P_Z>\eta}{\alpha_R + \eta + \delta n^2/R^2}\times(1-\psi),$$

$$\psi(z) = \frac{\cosh(kZ/h)}{\cosh(k/2) + \sinh(k/2)\lambda_b k/h} \tag{8.39}$$

Since Bessel function $J_0(x)$ has infinite series of roots (Fig.8.3), our Pz also has infinite series of modes:

$$P_Z\big|_{\rho=R} = 0, \quad \frac{nJ_0(n)}{2J_1(n)} \times AW \times (1-\psi) = 0, \quad J_0(n) = 0 \tag{8.40}$$

$$n = a_1, a_2, a_3 ....$$

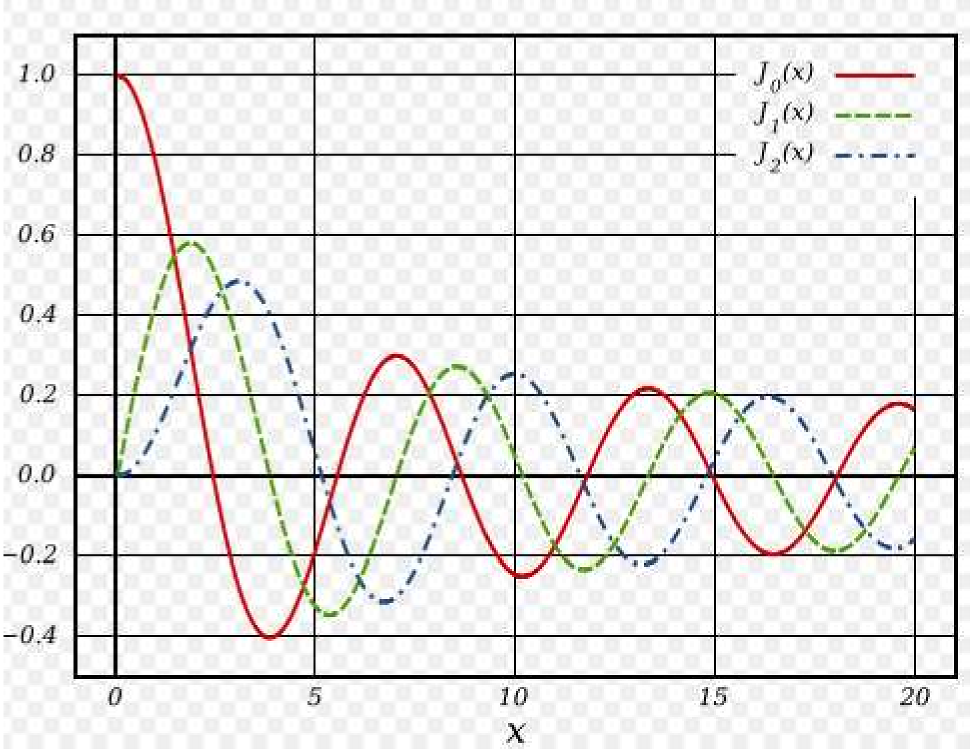

Fig. 8.3 Plot of Bessel function $J_0(x)$, $J_1(x)$ and $J_2(x)$

Let's break down first 3 modes of $J_0(x)$.

1st mode, $n = a_1$,

$$P_Z = \frac{a_1 J_0(a_1\rho/R)}{2J_1(a_1)} \times \frac{E_0 + <P_Z>\eta}{\alpha_R + \eta + \delta a_1^2/R^2} \times (1-\psi),$$

$P_Z = 0$ only when $\rho = R$. (8.41)

2nd mode, $n = a_2$,

$$P_Z = \frac{a_2 J_0(a_2\rho / R)}{2J_1(a_2)} \times \frac{E_0 + < P_Z > \eta}{\alpha_R + \eta + \delta a_2^2 / R^2} \times (1-\psi),$$

$$P_Z = 0 \text{ when } \rho = R \text{ or } \rho = \frac{a_1}{a_2} R. \tag{8.42}$$

3rd mode, $n = a_3$,

$$P_Z = \frac{a_3 J_0(a_3\rho / R)}{2J_1(a_3)} \times \frac{E_0 + < P_Z > \eta}{\alpha_R + \eta + \delta a_3^2 / R^2} \times (1-\psi),$$

$$\text{when } \rho = R \text{ or } \rho = \frac{a_1}{a_3} R \text{ or } \rho = \frac{a_2}{a_3} R, \ P_Z = 0 \tag{8.43}$$

…..

We can solve <P$_Z$> explicitly at every mode from (8.39).

$$< P_Z >= \frac{\dfrac{E_0(1-\psi)}{\alpha_R + \eta + \delta n^2 / R^2}}{1 - \dfrac{\eta(1-\psi)}{\alpha_R + \eta + \delta n^2 / R^2}} = \frac{E_0(1-\psi)}{\alpha_R + \eta\psi + \delta n^2 / R^2} \tag{8.44}$$

From <Pz>, we get $< \varepsilon_{ZZ} >$.

$$< \varepsilon_{ZZ} >= \frac{d < P_Z >}{dE_0} = \frac{\dfrac{(1-\psi)}{\alpha_R + \eta + \delta n^2 / R^2}}{1 - \dfrac{\eta(1-\psi)}{\alpha_R + \eta + \delta n^2 / R^2}} = \frac{(1-\psi)}{\alpha_R + \eta\psi + \delta n^2 / R^2} \tag{8.45}$$

After getting <Pz>, the solution for Pz is simplified to:

$$P_Z = \frac{nJ_0(n\rho / R)}{2J_1(n)} \times \frac{E_0(1-\psi)}{\alpha_R + \eta\psi + \delta n^2 / R^2}, \quad \psi(z) = \frac{\cosh(kZ / h)}{\cosh(k/2) + \sinh(k/2)\lambda_b k / h}$$

(8.46)

$$E_Z^d(\rho,z)=\eta(<P_Z>-P_Z(\rho,z))=\eta\times\left(1-\frac{nJ_0(n\rho/R)}{2J_1(n)}\right)\times\frac{E_0(1-\psi)}{\alpha_R+\eta\psi+\delta n^2/R^2} \tag{8.47}$$

8.5 Results and discussions

Fig.8.4 and Fig.8.5 are the comparison of our calculated Pz for the 1st mode and the results from [8]. Fig.8.4 is the plot of Pz VS. ρ at z=0, Fig.8.5 is the plot of Pz VS. z at ρ=0. The constants used are listed in table 8.1.

Table 8.1 Constants used in solving Landau equation and calculating transition temperature T_N for $BaTiO_3$ nanowire

Constants	**Value used in calculation**
h/R	100
α_T (1/K)	0.0005375
Q_{12}	-0.043
μ (nm)	0.224
η	0.005
n(a_1)	2.405
T_C(K)	400
δ (nm^2)	0.0396
λ_b	0.159

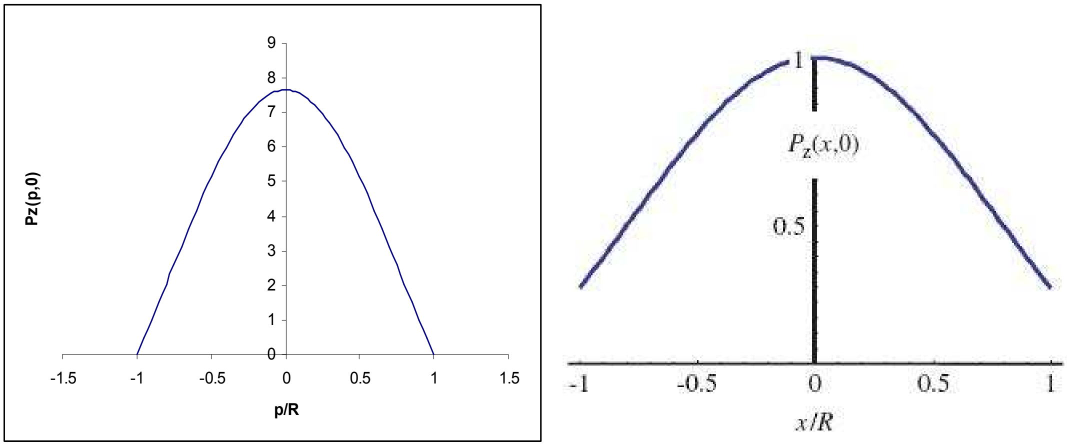

(a) (b)

Fig. 8.4 Pz VS. ρ: (a) calculated Pz for 1st mode; (b) results from [8].

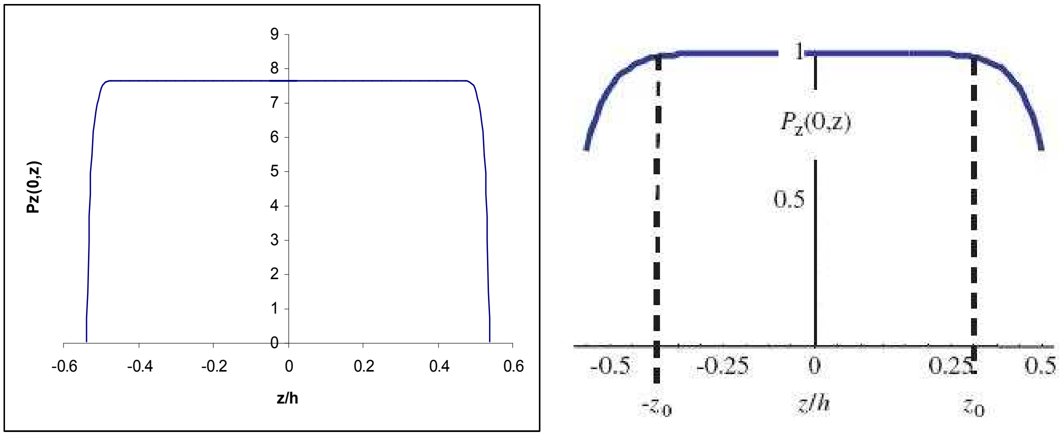

(a) (b)

Fig. 8.5 Pz VS. z: (a) calculated Pz for 1st mode; (b) results from [8].

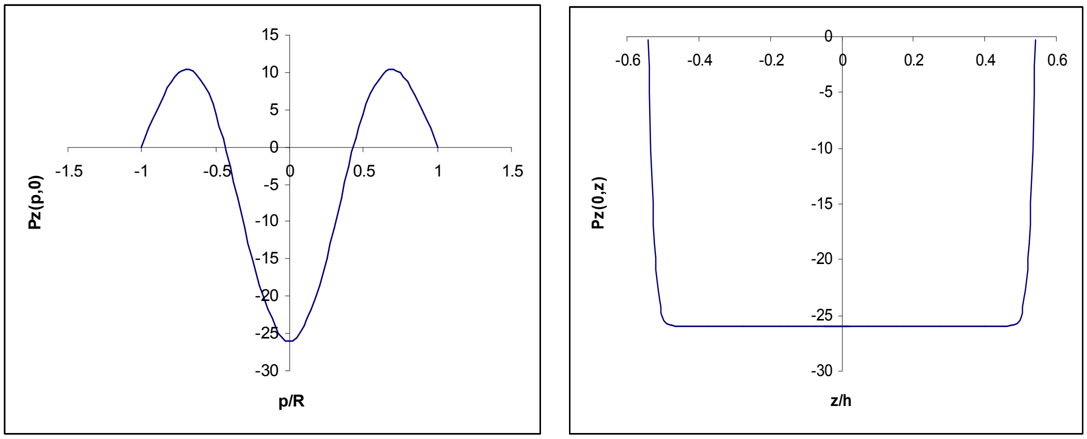

(a) (b)

Fig. 8.6 2nd mode: (a) Pz VS ρ, (b) Pz VS. z

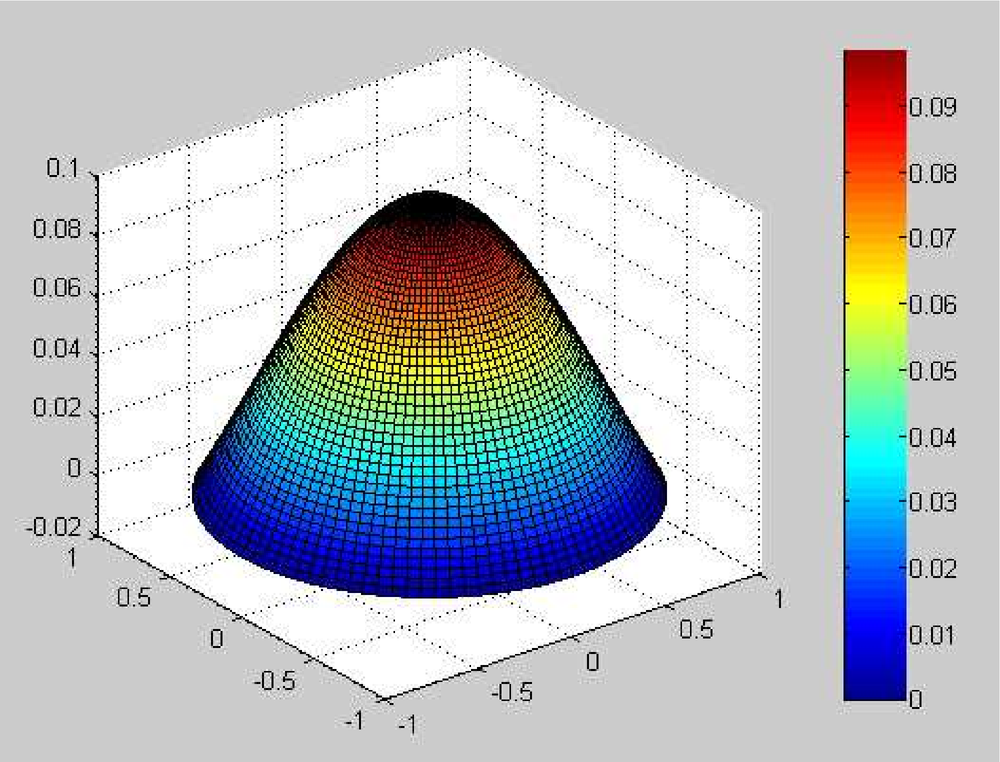

Fig. 8.7 3-D presentation for Pz 1st mode

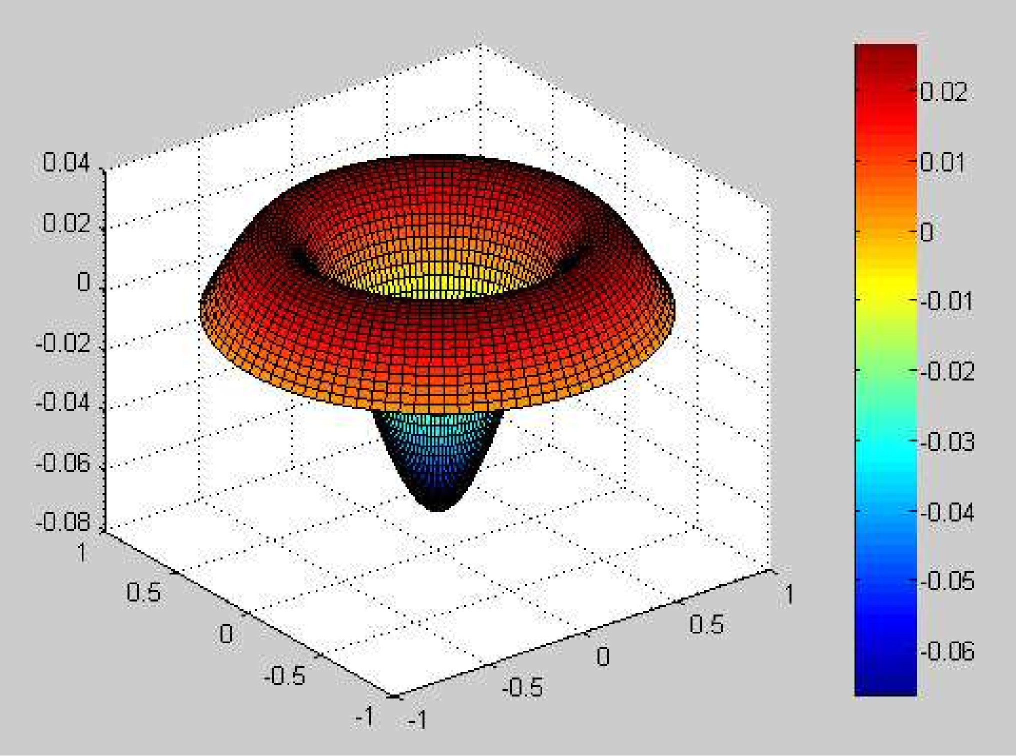

Fig. 8.8 3-D presentation for Pz 2nd mode

Fig.8.6 shows our 2nd mode calculated results for Pz VS. ρ and Pz VS. z. Fig.8.7 and Fig.8.8 are the 3-dimentional plots of Pz for the 1st mode and 2nd mode. Interestingly, our 2nd mode results have matched Min-Feng Yu [78] group's recent experimental discover (Fig.8.11).

Yu's [78] group has done a series of experiments on $BaTiO_3$ nanowires using Piezo-response force microscopy (PFM) and Scanning Electron Microscopy (SEM). One of the tests was to operate PFM in both vertical and lateral modes using atomic force microscope (AFM) cantilever. Results showed ferroelectric polarization switching along the axial (lateral) direction of nanowire, while the polarization along the transversal (vertical) direction was strongly suppressed. Such a one-dimensional polarization formation was also found to be highly stable and nonretentive in that switched polarization spontaneously returned to its original orientation at the instant of removing the applied poling voltage.

Fig.8.9 is a lattice resolved high-resolution transmission electron microscopy (TEM) image, which shows that $BaTiO_3$ nanowire is single crystalline with a lattice constant of 4.02 Å and free of almost any internal defects. Selected area electron diffraction from a single nanowire, shown in the inset of Fig.8.9b, reveals that the pseudo cubic $BaTiO_3$ structure has one of the three principle <100> lattice axes aligned along the wire length direction.

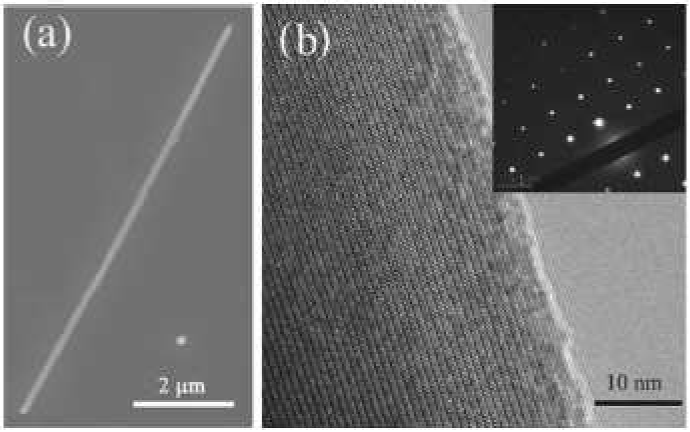

Fig. 8.9 (a) SEM image of a typical $BaTiO_3$ nanowire. (b) High-resolution TEM image of a $BaTiO_3$ nanowire. Inset: the selected area electron diffraction pattern from nanowire. [78]

Fig.8.10 shows both ends of the nanowires were fixed onto the electrodes with platinum contacts made by localized gas assisted e-beam deposition inside a scanning electron microscope. The testing device was then transferred into our PFM system and positioned so that the nanowire direction was aligned perpendicular to the AFM cantilever, a necessary step for the study of axial (in-plane) polarization in nanowire with lateral mode PFM. For lateral mode PFM, if the local in-plane polarization is aligned along the (+x) length direction of the nanowire, the induced shear deformation (piezo-response) would be in sync with the ac signal applied on the AFM tip, and the measured phase difference between the piezo-response and the ac signal is zero. Otherwise, if the local polarization is along the (−x) length direction, the measured phase difference is 180◦. Thus, the phase signal detected in lateral mode PFM can be used to characterize the polarization orientation for a given domain in ferroelectric structure. For the nanowire shown in Fig.6.11, a phase change from 0◦ to 180◦ or vice versa will occur if the polarization is switched by the applied axial dc bias. [79]

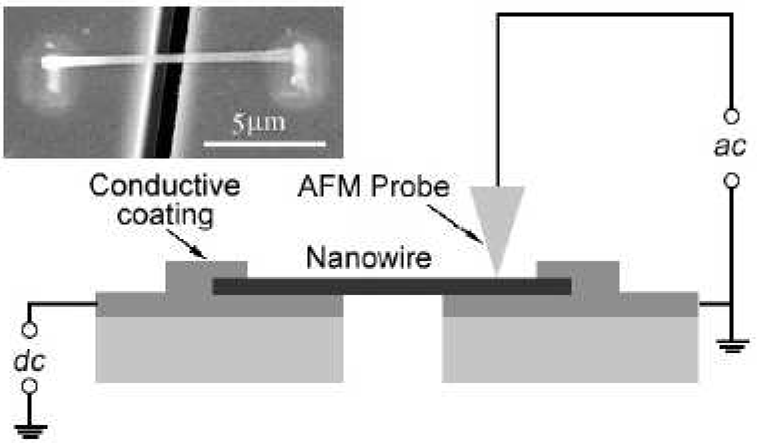

Fig. 8.10 Schematic diagram showing the axial dc biasing PFM for ferroelectric switching study of nanowire. The inset shows the SEM image of the studied $BaTiO_3$ nanowire in the testing device.[79]

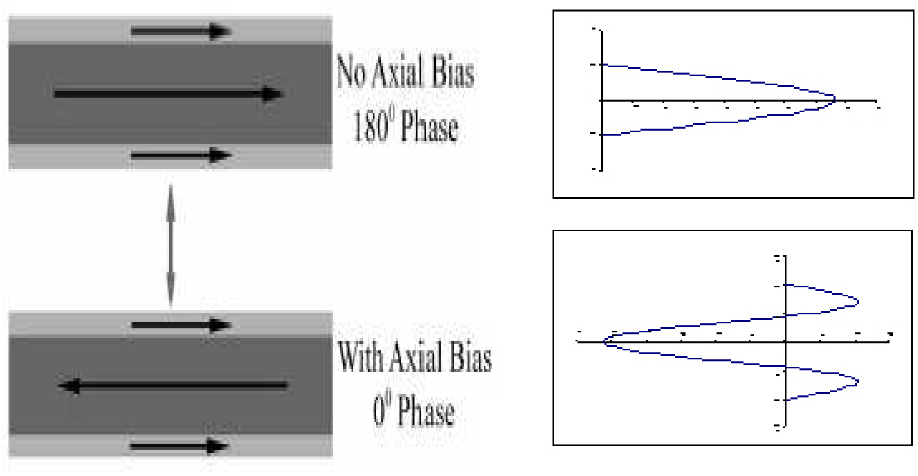

(a) (b)

Fig. 8.11 Comparison: (a) [79]schematic diagram showing the axial polarization switching behavior of a $BaTiO_3$ nanowire according to the core–shell model [80]; (b) calculated 1st and 2nd modes.

8.6 Nanowire size effect on its transition temperature

In Morozovska's work [8], the temperature effect is also studied as well as size effect for $BaTiO_3$ nanowires. They found the transition temperature is the highest when the nanowire is at its critical size, below which the nanowire won't show ferroelectricity.

The equation for paraelectric (Cubic) to ferroelectric (Tetragonal) phase transition temperature T_N can be obtained from Eq. (6.46) in the following form which is setting denominator equal to zero:

$$\alpha_R + \eta\psi + \delta n^2/R^2 = 0 \tag{8.48}$$

From $k = h\sqrt{\dfrac{\alpha+\eta-m}{\delta}}$ in equation (6.18) and $\dfrac{m}{\delta} = -\dfrac{n^2}{R^2}$, it is not hard to get,

$$\alpha_R = \delta k^2/h^2 - \eta - \delta n^2/R^2 \tag{8.49}$$

By combining (8.48) and (8.49), the condition for $BaTiO_3$ phase transformation from paraelectric to ferroelectric has a new expression which is identical to (8.48) mathematically.

$$\delta k^2/h^2 - \eta(1-\psi) = 0 \tag{8.50}$$

Since ψ is changing along Z direction, an average over entire nanowire needs to be calculated and it is given as follows,

$$\begin{aligned}\langle\psi(z)\rangle &= \frac{1}{h}\int_{-h/2}^{h/2}\frac{\cosh(kZ/h)}{\cosh(k/2)+\sinh(k/2)\lambda_b k/h}dZ = \frac{\sinh(kZ/h)}{k[\cosh(k/2)+\sinh(k/2)\lambda_b k/h]}\Bigg|_{-h/2}^{h/2}\\ &= \frac{2\sinh(k/2)}{k[\cosh(k/2)+\sinh(k/2)\lambda_b k/h]} = \frac{2}{k[\coth(k/2)+\lambda_b k/h]}\end{aligned} \tag{8.51}$$

Now the condition (8.48) and (8.50) become,

$$\alpha_R + \eta\langle\psi\rangle + \delta n^2/R^2 = 0,\ \delta k^2/h^2 - \eta(1-\langle\psi\rangle) = 0 \tag{8.52}$$

For α_R, we follow (8.4) for special case when $T=T_N$.

$$\alpha_R(T_N, R) = \alpha_T(T_N - T_C) + 2Q_{12}\frac{\mu}{R} \tag{8.53}$$

Substitute (8.53) into (8.52), we get the following equation in which transition temperature T_N is involved.

$$\alpha_T(T_N - T_C) + 2Q_{12}\frac{\mu}{R} + \eta\langle\psi\rangle + \delta n^2 / R^2 = 0 \tag{8.54}$$

Now the transition temperature T_N for $BaTiO_3$ nanowire can be expressed explicitly in terms of nanowire radius R.

$$\begin{aligned} T_N &= T_C - \frac{1}{\alpha_T}[2Q_{12}\frac{\mu}{R} + \eta\langle\psi\rangle + \delta n^2 / R^2] \\ &= T_C - \frac{2\mu Q_{12}}{\alpha_T R} - \frac{\delta n^2}{\alpha_T R^2} - \frac{2\eta \sinh(k/2)}{k\alpha_T[\cosh(k/2) + \sinh(k/2)\lambda_b k / h]} \end{aligned} \tag{8.55}$$

The first term T_C in Eq. (8.55) is Curie temperature for $BaTiO_3$ bulk material, the second term is related to the coupling of surface tension with polarization via electrostriction effect, the third one corresponds to the correlation effects, and the fourth represents the depolarization field contribution.

Now, from the Landau's theory, the transition temperature T_N in terms of diameter of the wire has been be obtained from equation (8.55) and the comparison with experimental data given in Fig. 3.3 is shown in Fig. 8.12. All of the constants used in the calculation are listed in table 8.1.

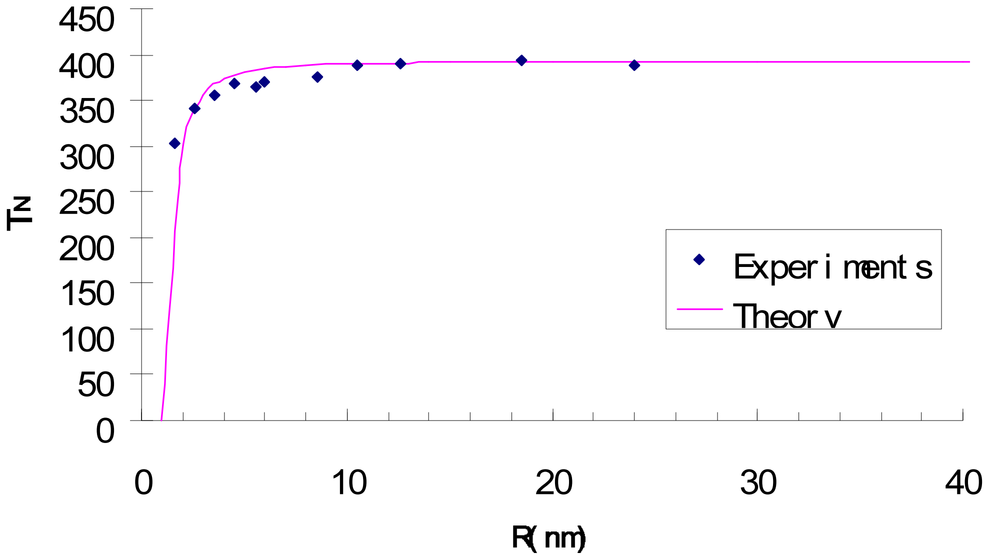

Fig. 8.12 Transition temperature T_N versus $BaTiO_3$ nanowire radius R

An simpler case for Nanowires with infinite length is listed as the following. When $h \to \infty$, $\eta \to 0$ (from Eq. 8.5), then

$$\alpha_T(T_N - T_C) + 2Q_{12}\frac{\mu}{R} + \delta n^2 / R^2 = 0 \qquad (8.56)$$

(6.55) is then simplified as,

$$T_N = T_C - \frac{2\mu Q_{12}}{\alpha_T R} - \frac{\delta n^2}{\alpha_T R^2} \qquad (8.57)$$

8.7 Conclusions

Landau theory which is a phenomenological approach is introduced and extended to study the polarization distribution and the Curie temperature of ferroelectric nanowires. The theoretical results have been compared with experimental data and they are found to fit well. During the derivation, a second mode of general solution has been found to be consistent with the existing core-shell theory.

9. Conclusions and Future Work

9.1 Importance of theoretical work

One may argue that doing experiments is the only way to understand physical principles that then can be used in practice by others; theoretical work can play a big role in it, too. Because doing experiments may need long time to accomplish and can be very costly, theoretical modeling is more efficient then. Of course theoretical modeling still needs the support from experiments most of the time.

Over the years, there have been quite a lot of theories trying to unfold the physical principle behind the electromechanical behavior of piezoelectric crystals. It is still lack of a universal model that can be applied broadly from calculating properties coefficients to producing hysteresis loop and butterfly curves; Ferroelectric Nanowires have been a hot topic in recent years, however, the current theoretical models are either having difficulty to reflect the ferroelectric phenomenon or being too complicated that are hard to use practically; Composite materials draw more and more attention due to its overall better properties than the component materials within while theoretical models are still in need.

Because of above, we put efforts on all of these areas trying to establish a practical model that can be used on these issues.

9.2 Theoretical Models Developed

Three approaches and one combined approach have been introduced in this dissertation to study the electromechanical behavior of ferroelectric crystals and their composites.

First, in Chapter 4, a simple mechanical approach based on the texture and anisotropy of the system is proposed without consideration of the interaction between the domains and/or grains to mimic the piezoelectric single crystal response under external electric loadings with different angles.

Second, a micromechanics approach based on irreversible thermodynamics principle and the morphology of domain switch and spontaneous polarization is developed to study the temperature effect on physical properties of ferroelectric crystals in Chapter 5; then it has been extended to study electromechanical coupling behavior of ferroelectric composites by considering the microstructure of the system in Chapter 6.

Third, Landau theory which is a phenomenological approach is extended to study the polarization distribution and the Curie temperature of ferroelectric nanowires in Chapter 8.

All of above theoretical modeling results have been compared with experimental data.

9.3 Future Work

In Chapter 8, we adopted a phenomenological approach called Landau theory from physics field to study the size effects on $BaTiO_3$ nanowires transition temperatures. We also listed this approach in Chapter 1 as applicable in the nano-scale range. However, this approach actually can be applied to all the ranges. To be able to apply this approach to micro or macro scale ranges, the original Landau equation has to be used which is a function of energy in terms of variable P. This P can be assigned as any physical properties. The Landau equation used in Chapter 8 was simplified and the variable P was assigned as the polarization along Z direction inside each single cell within the $BaTiO_3$ nanowire. In the future, one can continue this work to utilize Landau theory to other scale ranges so that it can become a universal approach to study electromechanical coupling behavior of ferroelectric materials.

Appendix A Eshelby's S tensor

A.1 Spontaneous Polarization (from Cubic to Tetragonal)

Non-vanishing components of the S tensor are:

$$S_{1111} = 1$$

$$S_{1122} = \frac{C_{12}}{C_{11}}$$

$$S_{1212} = S_{1313} = \frac{1}{2}$$

$$S_{4242} = S_{4343} = 1$$

A.2 90° Domain Switch

Non-vanishing components of the S tensor are:

$$S_{3333} = 1$$

$$S_{3311} = S_{3322} = -\frac{C_{13}k_{33} + e_{33}e_{31}}{C_{33}k_{33} + e_{33}^2}$$

$$S_{3343} = \frac{e_{33}}{C_{33}k_{33} + e_{33}^2}$$

$$S_{1331} = S_{1313} = S_{3232} = \frac{1}{2}$$

$$S_{4141} = S_{4242} = 1$$

Appendix B Coefficients Conversions

Constitutive Equations:

$$\varepsilon = s\sigma + d^T \mathrm{E}$$

$$\mathrm{D} = d\sigma + k^{\sigma} \mathrm{E}$$

$$\sigma = c\varepsilon - e^T \mathrm{E}$$

$$\mathrm{D} = e\varepsilon + k^{\varepsilon} \mathrm{E}$$

Conversion from (c, e, k) to (s, d, k):

$$S_{11} = \frac{C_{11}C_{33} - C_{13}^2}{(C_{11} - C_{12})[(C_{11} + C_{12})C_{33} - 2C_{13}^2]}$$

$$S_{12} = \frac{-C_{12}C_{33} + C_{13}^2}{(C_{11} - C_{12})[(C_{11} + C_{12})C_{33} - 2C_{13}^2]}$$

$$S_{13} = \frac{-C_{13}}{(C_{11} + C_{12})C_{33} - 2C_{13}^2}$$

$$S_{33} = \frac{C_{11} + C_{12}}{(C_{11} + C_{12})C_{33} - 2C_{13}^2}$$

$$S_{44} = \frac{1}{C_{44}}$$

$$S_{66} = \frac{1}{C_{66}}$$

$$d_{31} = \frac{C_{33}e_{31} - C_{13}e_{33}}{(C_{11} + C_{12})C_{33} - 2C_{13}^2}$$

$$d_{33} = \frac{(C_{11} + C_{12})e_{33} - 2C_{13}e_{31}}{(C_{11} + C_{12})C_{33} - 2C_{13}^2}$$

$$d_{15} = \frac{e_{15}}{C_{44}}$$

$$k_{11}^{\sigma} = k_{11}^{\varepsilon} + \frac{e_{15}^2}{C_{44}}$$

$$k_{33}^{\sigma} = k_{33}^{\varepsilon} + \frac{[(C_{11} + C_{12})e_{33} - 2C_{13}e_{31}]e_{33} + 2(C_{33}e_{31} - C_{13}e_{33})e_{31}}{(C_{11} + C_{12})C_{33} - 2C_{13}^2}$$

Conversion from (s, d, k) to (c, e, k):

$$C_{11} = \frac{S_{11}S_{33} - S_{13}^2}{(S_{11} - S_{12})[(S_{11} + S_{12})S_{33} - 2S_{13}^2]}$$

$$C_{12} = \frac{-S_{12}S_{33} + S_{13}^2}{(S_{11} - S_{12})[(S_{11} + S_{12})S_{33} - 2S_{13}^2]}$$

$$C_{13} = \frac{-S_{13}}{(S_{11} + S_{12})S_{33} - 2S_{13}^2}$$

$$C_{33} = \frac{S_{11} + S_{12}}{(S_{11} + S_{12})S_{33} - 2S_{13}^2}$$

$$C_{44} = \frac{1}{S_{44}}$$

$$C_{66} = \frac{1}{S_{66}}$$

$$e_{31} = \frac{S_{33}d_{31} - S_{13}d_{33}}{(S_{11} + S_{12})S_{33} - 2S_{13}^2}$$

$$e_{33} = \frac{(S_{11} + S_{12})d_{33} - 2S_{13}d_{31}}{(S_{11} + S_{12})S_{33} - 2S_{13}^2}$$

$$e_{15} = \frac{d_{15}}{S_{44}}$$

$$k_{11}^{\varepsilon} = k_{11}^{\sigma} + \frac{d_{15}^2}{S_{44}}$$

$$k_{33}^{\varepsilon} = k_{33}^{\sigma} - \frac{[(S_{11} + S_{12})d_{33} - 2S_{13}d_{31}]d_{33} + 2(S_{33}d_{31} - S_{13}d_{33})d_{31}}{(S_{11} + S_{12})S_{33} - 2S_{13}^2}$$

References

1. J. E. Huber, N. A. Fleck, Multi-axial electrical switching of a ferroelectric: theory versus experiment, J. Mech. Phys. Solids 49, 785-811, (2001).

2. X, Chen, D. N. Fang and K. C. Hwang, Micromechanics simulation of ferroelectric polarization switching, Acta Mater, Vol. 45, No. 8, 3138-3189, (1997).

3. J. Fan, W. A. Stoll and C. S. Lynch, Nonlinear constitutive behavior of soft and hard PZT: experiments and modeling, Acta Mater, Vol. 47, No. 17, 4415-4425, (1999).

4. W. Seemann, A. Arockiarajan, B. Delibas, Modeling and simulation of piezoceramic materials using micromechanical approach, Proceedings of European Congress on Methods in Applied Sciences and Engineering (2004).

5. J. Li and G. J. Weng, A theory of domain switch for nonlinear behavior of ferroelectrics, Proc. R. Soc. London, A 455, 3493-3511 (1999).

6. J. Li and G. J. Weng, A Micromechanics-Based Hysteresis Model for Ferroelectric Ceramics, J. Intell. Mater. Syst. Struct. 12, 79-91 (2001).

7. J. Li, Electromechanical coupling behavior of ferroelectric ceramics under multiaxial electric switching, J. Appl. Phys., 94, No. 5, 3326-3332 (2003).

8. A.N. Morozovska, E.A. Eliseev, M.D. Glinchuk, Size effects and depolarization field influence on the phase diagrams of cylindrical ferroelectric nanoparticles, Physica B 387, 358-366 (2007).

9. http://en.wikipedia.org/wiki/Piezoelectric

10. J. F. Nye, Physical Properties of Crystals, Oxford University Press Inc., New York,

(1985).

11. C. M. Landis, Non-linear constitutive modeling of ferroelectrics, Current Opinion in solid state and materials science 8, 59-69 (2004).

12. J. Wang, S-Q. Shi and L-Q. Chen, Phase field simulations of ferroelectric/ferroelastic polarization switching, Acta Mater, 52, 749-764 (2004).

13. J. Wang, Y. Li, L-Q. Chen et, The effect of mechanical strains on the ferroelectric and dielectric properties of a model single crystal – Phase field simulation, Acta Mater, 53, 2495-2507 (2005).

14. S. C. Hwang, C. S. Lynch and R. M. Mcmeeking, Ferroelectric/Ferroelastic interactions and a polarization switching model, Acta Mater. 43, 2073 (1995)

15. S. C. Hwang and R. M. McMeeking, the prediction of switching in polycrystalline ferroelectric ceramics, Ferroelectrics, Vol. 207, pp. 465-495, 1998

16. A. Stanishevsky, S. Aggarwal, A. S. Prakash, J. Melngailis, and R.Ramesh, Focused ion-beam patterning of nanoscale ferroelectric capacitors, J. Vac. Sci. Technol. B 16, 3899 (1998).

17. M. Alexe, C. Harnagea, D. Hesse, and U. Gosele, Patterning and switching of nanosize ferroelectric memory cells, Appl. Phys. Lett. 75, 1793 (1999).

18. A. Gruverman, O. Auciello and H. Tokumoto, Scanning Force Microscopy: Application to Nanoscale Studies of Ferroelectric Domains, Integrated Ferroelectrics 19, 49-83 (1998).

19. A.F. Devonshire, Theory of barium titanate—part I, Philos. Mag. 40, 1040 (1949).

20. A.F. Devonshire, Theory of barium titanate—part II, Philos. Mag. 42, 1065 (1951).

21. P. Zhao and J. Li, Orientation dependence on electromechanical coupling behavior of ferroelectrics under compression , J. Appl. Phys., 103, 104104 (2008).

22. P. Zhao, Dissertation: Effects of Orientation on Electro-Mechanical Coupling Behavior of Ferroelectrics and Their Composites, The City University of New York (2009).

23. W.J. Merz, The Electric and Optical Behavior of $BaTiO_3$ Single-Domain Crystals, Phys. Rev. 76, 1221 (1949)

24. W.J. Merz, The Effect of Hydrostatic Pressure on the Curie Point of Barium Titanate Single Crystals, Phys. Rev. 78, 52 (1950)

25. W.J. Merz, Domain Properties in $BaTiO_3$, Phys. Rev. 88, 421 (1952)

26. W.J. Merz, Domain Formation and Domain Wall Motions in Ferroelectric $BaTiO_3$ Single Crystals, Phys. Rev. 95, 690 (1954)

27. M.E. Caspari and W.J. Merz, The Electromechanical Behavior of $BaTiO_3$ Single-Domain Crystals, Phys. Rev. 80, 1082 (1950).

28. K. Ishikawa, K. Yoshikawa, and N. Okada, Size effect on the ferroelectric phase transition in $PbTiO_3$ ultrafine particles, Phys. Rev. B 37, 5852 (1988).

29. K. Ishikawa, T. Nomura, N. Okada, and K. Takada, Jpn. Size Effect on the Phase Transition in $PbTiO_3$ Fine Particles, J. Appl. Phys. 35, 5196 (1996).

30. W. L. Zhong, B. Jiang, P. L. Zhang, J. M. Ma, H. M. Cheng, Z. H. Yang, and L. X. Li, Phase transition in $PbTiO_3$ ultrafine particles of different sizes, J. Phys.: Condens. Matter

5, 2619 (1993).

31. B. Jiang, J. L. Peng, L. A. Bursill, and W. L. Zhong, Size effects on ferroelectricity of ultrafine particles of $PbTiO_3$, J. Appl. Phys. 87, 3462 (2000).

32. W. S. Yun, J. J. Urban, Q. Gu, and H. Park, Ferroelectric properties of individual barium titanate nanowires investigated by scanned probe microscopy, Nano Lett. 2, 447 (2002).

33. G. Geneste, E. Bousquet, J. Junquera, and P. Ghosez, Finite-size effects in $BaTiO_3$ nanowires, Appl. Phys. Lett. 112906, 88 (2006).

34. J. Padilla and D. Vanderbilt, Ab initio study of $BaTiO_3$ surfaces, Phys. Rev. B 56, 1625 (1997).

35. R. E. Cohen, Origin of ferroelectricity in oxide ferroelectrics and the difference in ferroelectric behavior of $BaTiO_3$ and $PbTiO_3$, Nature (London) 358, 136 (1992).

36. Jonathan E. Spanier, Alexie M. Kolpak, Jeffrey J. Urban, Ilya Grinberg, Lian Ouyang, Wan Soo Yun, Andrew M. Rappe and Hongkun Park, Ferroelectric phase transitions in individual single-crystalline $BaTiO_3$ nanowrires, Nano Letters, 6, No.4, 735-739 (2006).

37.http://www.geology.um.maine.edu/geodynamics/microdynamics/ellemodules/TBH%20Site/html%20files/index.html

38. U.K. Kocks, C.N. Tome, H.R. Wenk, H. Mecking, Texture and Anisotropy, Cambridge University Press (2008)

39. Y. Su and G. J. Weng, The shift of Curie temperature and evolution of ferroelectric domain in ferroelectric crystals, J. Mech. Phys. Solids 53, 2071 (2005)

40. J.C. Slater, The Lorentz Correction in Barium Titanate, Phys. Rev. 78, 748 (1950).

41. A.F. Devonshire, Theory of ferroelectrics, Philos. Mag. Suppl. (Adv. Phys.) 3, 85 (1954).

42. H. Cao and A. G. Evans, Nonlinear deformation of ferroelectric ceramics, J. Am. Ceram. Soc. 76, 890 (1993).

43. Y.C. Shu and K. Bhattacharya, Domain patterns and macroscopic behaviour of ferroelectric materials, Philos. Mag. B 81, 2021 (2001).

44. E. Burcsu, G. Ravichandran, and K. Bhattacharya, Large electrostrictive actuation of barium titanate single crystals, J. Mech. Phys. Solids 52, 823 (2004).

45. J.Y. Li and D. Liu, On ferroelectric crystals with engineered domain configurations, J. Mech. Phys. Solids 52, 1719 (2004).

46. R.M. McMeeking and S.C. Hwang, On the Potential Energy of a Piezoelectric Inclusion and the Criterion for Ferroelectric Switching, Ferroelectrics 200, 151 (1997).

47. W. Chen and C.S. Lynch, A micro-electro-mechanical model for polarization switching of ferroelectric materials, Acta Mater. 46, 5303 (1998).

48. T. Chen, C.W. Nan and G.J. Weng, Unified approach for the estimate of effective magnetostriction of composites and polycrystals with particulate and columnar microstructures, Phys. Rev. B 68, 224406 (2003).

49. J. Li, Orientation-dependent piezoelectric Eshelby S -tensor for a lamellar structure in a transversely isotropic medium, Acta Mech. 162, 69 (2003).

50. W.F. Li and G.J. Weng, A micromechanics-based thermodynamic model for the

domain switch in ferroelectric crystals, Acta Mater. 52, 2489 (2004).

51. Y. Su and G.J. Weng, A polycrystal model for the anisotropic behavior of a fully poled ferroelectric ceramic, J. Appl. Phys., 100, 114110 (2006).

52. N. Srivastava and G.J. Weng, A theory of double hysteresis for ferroelectric crystals, J. Appl. Phys., 99, 054103 (2006).

53. L.P. Tang, S.H. Xie, X.J. Zheng, Y.C. Zhou and J.Y. Li, Domain switching in ferroelectric ceramics beyond Taylor bound, Mech. Mater., 40, 362 (2008).

54. Z.K. Lu and G.J. Weng, Martensitic Transformation and Stress-Strain Relations of Shape-Memory Alloys, J. Mech. Phys. Solids, 45, 1905 (1997).

55. Z.K. Lu and G.J. Weng, A self-consistent model for the stress–strain behavior of shape-memory alloy polycrystals, Acta Mater., 46, 5423-5433 (1998).

56. T. Mori and K. Tanaka, Average Stress in Matrix and Average Elastic Energy of Materials with Misfitting Inclusion, Acta Metall. 21, 571 (1973).

57. A. Norris, A differential scheme for the effective moduli of composites, Mech. Mat. 4, 1 (1985).

58. R. Hill, Continuum Micro-Mechanics of Elastoplastic Polycrystals, J. Mech. Phys. Solids, 13, 89 (1965).

59. M. Berveiller and A. Zaoui, An Extension of the Self-Consistent Scheme to Plastically-Flowing Polycrystals, J. Mech. Phys. Solids, 26, 325 (1979).

60. G.J. Weng, A Unified, Self-Consistent Theory for the Plastic-Creep Deformation of Metals, J. Appl. Mech., 49, 728 (1982).

61. J.D. Eshelby, The Determination of the Elastic Field of an Ellipsoidal Inclusion, and Related Problems, Proc. R. Soc. London A241, 376 (1957).

62. J.H. Huang and J.S. Yu, Electroelastic Eshelby tensors for an ellipsoidal piezoelectric inclusion, Compos. Eng. 4, 1169 (1994).

63. M.L. Duun, Electroelastic Green's functions for transversely isotropic piezoelectric media and their application to the solution of inclusion and inhomogeneity problems, Int. J. Eng. Sci. 32, 119 (1994).

64. M.L. Duun and H.A. Wienecke, Inclusions and Inhomogeneities in Transversely Isotropic Piezoelectric Solids, Int. Solids Struct. 34, 3571 (1997).

65. J.A. Hooton and W.J. Merz, Etch Patterns and Ferroelectric Domains in $BaTiO_3$ Single Crystals, Phys. Rev. 98, 409 (1955).

66. Y.Y. Liu, J.J. Liu, S.H. Xie and J.Y. Li, Energetics of charged domain walls in ferroelectric crystals, Appl. Phys. Lett. 91, 172910 (2007).

67. T. Ikeda, Fundamentals of piezoelectricity, Oxford Univ. Press, 1996).

68. J.F. Nye, Physical Properties of Crystals (Oxford University Press, Oxford, 1979).

69. J.R. Rice, Constitutive Equations in Plasticity, 23 (ed. A.S. Argon, MIT press, 1975).

70. Q.P. Sun, K.C. Hwang, and S.W. Yu, A micromechanics constitutive model of transformation plasticity with shear and dilatation effect, J. Mech. Phys. Solids 39, 507 (1991).

71. Q.P. Sun and K.C. Hwang, Micromechanics modelling for the constitutive behavior of polycristalline shape memory alloys - Part I: Derivation of general relations, J. Mech.

Phys. Solids 41, 1 (1993).

72. Q.P. Sun and K.C. Hwang, Micromechanics modelling for the constitutive behavior of polycristaline shape memory alloys - Part II: Study of individual phenomena, J. Mech. Phys. Solids 41, 19 (1993).

73. G.J. Weng, The theoretical connection between Mori–Tanaka's theory and the Hashin–Shtrikman–Walpole bounds, Int. J. Eng. Sci. 28, 1110 (1990).

74. P. Sharma, S. Ganti, Size-Dependent Eshelby's Tensor for Embedded Nano-Inclusions Incorporating Surface/Interface Energies, Journal of Applied Mechanics, 71, 663 (2004).

75. P. Tan, L. Tong, Micro-electromechanics models for piezoelectric fiber reinforced composite materials, Composites Science and Technology, 61, 759-769 (2001).

76. H. Huang, C.Q. Sun, Zh. Tianshu, P. Hing, Grain-size effect on ferroelectric $Pb(Zr_{1-x}Ti_x)O_3$ solid solutions induced by surface bond contraction, Phys. Rev. B 63, 184112 (2001).

77. A.N. Morozovska, M.D. Glinchuk, E.A. Eliseev, Ferroelectricity enhancement in ferroelectric nanotubes, Phase Transitions, 80, 71-77 (2007)

78. Z. Wang, J. Hu, A. P. Suryavanshi, K. Yum, and M-F. Yu, Voltage Generation from Individual $BaTiO_3$ Nanowires under Periodic Tensile Mechanical Load, Nano Letters, 7, 2966 (2007).

79. Z. Wang, J. Hu and M-F. Yu, Axial polarization switching in ferroelectric $BaTiO_3$ nanowire, Nanotechnology 18, 235203 (2007).

80. M. Alexe, C. Harnagea, D. Hesse and U. Gosele, Polarization Imprint and Size Effects in Mesoscopic Ferroelectric Structures, Appl. Phys. Lett. 79, 242 (2001).